GEORG-AUGUST-UNIVERSITÄT
GÖTTINGEN

Master's Thesis

Spektralanalyse ausgewählter Carmenes Daten

Spectroscopic analysis of Carmenes sample

prepared by

Andre Lamert

from Merkers

at the Institut für Astrophysik, Göttingen

Thesis period:	1st April 2014 until 10th September 2014
First referee:	Dr. Sandra Jeffers
Second referee:	Prof. Dr. Ansgar Reiners

Abstract

In the last years the number of detected exoplanets increased rapidly. Upcoming projects like CARMENES, which is planned to find terrestrial planets in the habitable zone of M-dwarfs, will close the gap of Earth-mass planets in the exoplanet distribution.
This thesis investigates the spectral type, radial velocity and magnetic activity of candidate M-dwarfs for the CARMENES project input catalog CARMENCITA.It focuses on the determination of spectral M-type stars. Based on calibration functions of the code *THE HAMMER*, different atomic and molecular lines and bands are used to calculate spectral indices. With the aim of increasing the determination accuracy, I have written an algorithm which uses only few, but very sensitive indices. These are particular dominant for M-type stars. Additionally, the H_α line is used to determine the magnetic activity. To determine the spectral type, the radial velocity and an activity indicator I use 900 high-resolution spectra taken from 364 different stars of the input catalog. 348 of these spectra were provided as raw data from the CAFE spectrograph. I use the IDL-Package *REDUCE* for reduction and add a new flux extraction procedure and a modified order definition procedure to increase the extracted wavelength range and the quality of the extracted flux values. The written fast working spectral typing algorithm calculates quite accurate spectral types for high-resolution spectra, since the results of this typing confirm former results collected in CARMENCITA using low-resolution spectroscopy. Spectral types from this thesis deviate from literature values only by a maximum of one subtype. Calculated errors are in the same order of magnitude. For early type M-dwarfs the algorithm calculates spectral types of approximately 0.5 subtypes earlier than the literature types. For late type stars this shifts to a calculation of approximately 0.5 subtypes later than the literature types. From an analysis of the H_α line 73% of all investigated stars show a low level of activity. However, the sample provides minor indication that the fraction of active stars increases towards later spectral types.
The results of this thesis are will provide the best selection of the target stars for CARMENES based on the spectral types and help to exclude high-active stars from the radial velocity analysis of CARMENES.

Zusammenfassung

In den letzten Jahren ist der Anzahl der entdeckten Exoplaneten stark angestiegen. Projekte, die derzeit in der Entwicklungsphase sind, wie CARMENES, welches entwickelt wird, um terrestrische Planeten in der habitablen Zone von M-Zwergen zu finden, werden die Lücke von erdschweren Planeten in der Verteilung der bekannten Exoplaneten schließen.
In dieser Arbeit werden Spektraltypen, Radialgeschwindigkeit und magnetische Aktivität von Kandidatensternen der Klasse M für den CARMENES Input-Katalog CARMENCITA untersucht. Dabei wird ein Schwerpunkt auf die Bestimmung des Spektraltyps gelegt. Basierend auf Kalibrationsdaten des Codes *THE HAMMER* werden verschiedene atomare und molekulare Linien und Bänder genutzt, um anhand dieser spektrale Indizes zu bestimmen. Um die Genauigkeit der Ergebnisse zu erhöhen wurde ein Programm entwickelt, dass eine kleine Anzahl an Indizes nutzt, die allerdings hochsensitiv im Bereich der untersuchten Klasse M sind. Dieses schnell ausführbare Programm bestimmt Spektraltypen mit einer hohen Genauigkeit. Zusätzlich wird die H_α Linie genutzt, um die magnetische Aktivität der Sterne zu untersuchen. Um die Spektralklasse, die Radialgeschwindigkeit und einen Aktivitätsindikator zu bestimmen werden 900 Spektren verwendet, welche von 364 verschiedenen Sternen des Input-Katalogs aufgenommen wurden. 348 dieser Spektren standen als Rohdaten des CAFE Spektrographen zur Verfügung. Das IDL-Package *REDUCE* wird zur Datenreduktion genutzt, eine neue Fluss-Extraktions Prozedur hinzugefügt und die order-definition Prozedur modifiziert, um den extrahierten Wellenlängenbereich zu vergrößern und die Qualität des extrahierten Flusses zu verbessern. Der entwickelte, schnell ausführbare Algorithmus zur Bestimmung der Spektraltypen von hoch aufgelösten Spektren bestimmt die Spektraltypen mit hoher Genauigkeit. Die Ergebnisse dieser Bestimmung stimmen mit vorherigen Untersuchungen aus Spektren mit geringer Auflösung überein. Sie weichen von Literaturwerten nur um etwa 1 Subtyp ab, während die berechneten Fehler in der gleichen Größenordnung liegen. Für frühe M-Zwerge werden durch das Programm Spektraltypen bestimmt, die ungefähr 0,5 Subtypen früher einzuordnen sind als die Literaturwerte. Für späte Spektraltypen verschiebt sich dies zu Ergebnissen, die 0,5 Subtypen später sind als die Literaturwerte. Anhand einer Analyse der H_α Linie zeigen 73% der untersuchten Sterne ein schwaches Aktivitätsniveau, die Ergebnisse deuten allerdings auch darauf hin, dass der Anteil der aktiven Sterne zu späteren Spektraltypen hin ansteigt.
Die Ergebnisse dieser Arbeit erlauben eine bestmögliche Auswahl der zu beobachtenden Sterne für CARMENES basierend auf deren Spektraltyp und können helfen, aktive Sterne von der Radialgeschwindigkeitsanalyse von CARMENES auszuschließen. Dies soll eine bestmögliche Auswahl der zu beobachtenden Sterne gewährleisten.

Contents

List of Figures

1. Introduction

Since the first planet orbiting a solar-like star outside of our solar system was found by Mayor & Queloz (1995) the number of detected extra-solar planets ('exoplanets') is steadily rising. The discovery of extra-solar planets showed that our solar system is just one of many others. Even if not for every star in our galaxy a planet is already discovered it can be assumed that most of them are orbited by one or more exoplanets. For M-dwarfs this was recently shown by Tuomi et al. (2014). Today, the exoplanet cataloge *exoplanet.eu* (Schneider et al., 2011) lists 1815 planets in 1130 different systems. Figure 1.1 shows the distribution of detected exoplanets. Most of them have high masses, thus they are supposed to be gas giants. With an increasing accuracy of the instruments more and more planets with smaller masses were detected. Planets of low masses are thought to be terrestrial ones, since the gravitational potential of these bodies is not enough to hold together larger amounts of gas. New instruments with a rising precision will make it possible to decrease the mass limit of detection to the order of earth masses. With the detection of exoplanets a new field of astronomical research about planetary systems rose with two different activities: The search and detection of exoplanets and the research of physical processes of planets and their corresponding planetary systems. The distribution of exoplanets in our galaxy can show how common planets are and it will help to answer the question if we are living in a unique system. It can also be used to verify our understanding of the formation and evolution of planetary systems, especially of the origin of the two major types of planets: Terrestrial planets consisting of silicates and iron and gaseous planets made of gas without a solid surface.

Several techniques were developed to detect exoplanets (Perryman, 2011). The most successful techniques, the radial velocity method and the transit method, can be used to determine physical properties of the planet like distance to its host star, its mass or its size. The rising level of accuracy of transit measurements even allows to study the transmission and absorption properties of the planet's atmospheres (Agol et al., 2010, Knutson et al., 2007).

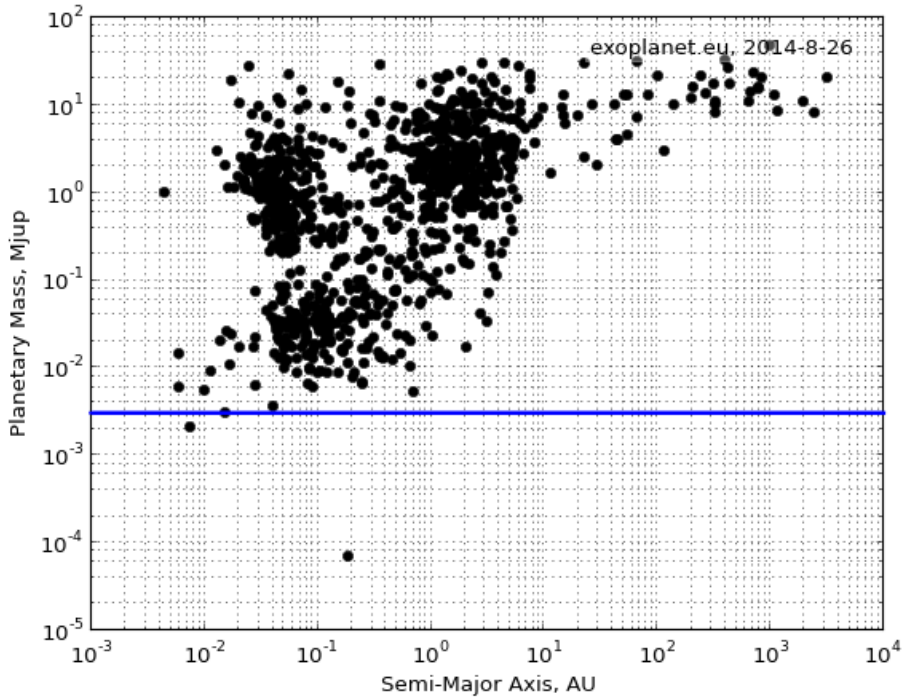

Figure 1.1.: Distribution of today known exoplanets. The mass of Earth is marked by a blue line. Almost all today known exoplanets have a mass higher than Earth. The lower edge of the mass of detected exoplanets is caused by the accuracy of current instruments.

The enhancement of detection accuracy of exoplanet research is leading the field to the range of Earth-like planets. Especially the search for Earth-twins is of major interest. These are terrestrial planets with a mass similar to the mass of the Earth orbiting their host star in the their habitable zone. This zone describes a range around a star where the surface temperature of a planet could allow the presence of liquid water. This is thought to be the major requirement to provide life. If a planet is orbiting its host star too close the radiation of the star would heat the planet, which evaporates all water. If the planet is too far away from its star the radiation would be insufficient to form liquid water so that all potential water would become ice. As of this writing 51 of 1457 detected planets listed in the Habitable Zone Gallery (Kane & Gelino, 2012) are entirely in the habitable zone of their host stars, but most of them are gas giants. However, terrestrial planets in the habitable zone are of much more interest for current exoplanet research. These rocky planets are expected to have masses lower than 10 $M_{\oplus}$ (Quirrenbach et al., 2012) what makes

them difficult to detect.

Figure 1.1 and the Habitable Zone Gallery show that current detection instruments are at the limit of the accuracy level to detect Earth-like planets in the habitable zone. For example, Kepler-186f (Quintana et al., 2014) is a confirmed planet with a mass of $1.11 \pm 0.14\ M_{\oplus}$. It seems plausible to assume this planet as terrestrial. Most other planets detected in the Habitable Zone of their host star are Kepler candidates or it is not clear whether they are of rocky or gaseous composition. Some planets, e.g. Kepler-62f, are thought to be ocean planets covered completely by water (Borucki et al., 2013). To find more potential habitable planets it is necessary to develop and build new instruments with a higher accuracy.

To search for Earth-like planets in the habitable zone the German-Spanish collaboration CARMENES (**C**alar **A**lto high-**R**esolution search for **M** dwarfs with **E**xo-earths with **N**ear-infrared and visible **E**chelle **S**pectrographs) (Quirrenbach et al., 2012) was started. It is planned to observe 300 M-dwarfs divided in three groups for late type M-dwarfs (M4 or later), mid type M-dwarfs (M3-M4) and early type M-dwarfs (M0-M2) with 100 stars in each sample to find their planets with the radial velocity technique, the most successful method for exoplanet search in the past (Schneider et al., 2011). CARMENES is developed to investigate the distribution of planets of late type stars, so the late type group is of most interest and can only be studied by CARMENES (Quirrenbach et al., 2012).

M-dwarfs are excellent targets to search for planets in their habitable zone. They are the most frequent type of stars in our galaxy (LeDrew, 2001). The main advantage of using M-dwarfs is a comparably large radial velocity signal caused by the low mass of this star type. M-dwarfs emit only a small amount of energy compared to earlier star types. Thus, the habitable zone of them lies very close to the star. Potential habitable planets need to orbit very close to their host star what amplifies the effect of a high radial velocity signal and leads to a high frequency of transit events because of a high orbital speed.

CARMENES will operate at the 3.5-m telescope at Calar-Alto observatory. It is a two-channel Echelle spectrograph that covers two wavelength ranges: An optical spectrograph with a CCD is planned to analyze the range from 530 nm to 1050 nm with $R = 80000$. A second one will observe in the infrared regime from 950 nm to 1800 nm with $R = 85000$. For the second wavelength range a HgCdTe detector to observe the near-infrared regime is necessary because of the Si cutoff at 1100 nm. CCDs do not provide sufficient efficiency around 1000 nm, what is a second reason

to use the near-IR detector. The wavelength range around 1000 nm is expected to be the best region for analyzing the radial velocity of M-dwarfs. Thus, CARMENES is optimized in this wavelength range. With both spectrographs an accuracy of radial velocity measurements of 1 ms^{-1} shall be reached (Quirrenbach et al., 2012). Both channels need a extremly high temperature stability to keep the radial velocity accuracy. A thermal stability of ± 0.07 K in 24h is required, while a stability of just ± 0.01 K is planned. With an exposure time of 900 s a SNR of 150 at $J = 9$ mag is expected (Quirrenbach et al., 2012). With this properties CARMENES should be able to detect planets with a mass of two earth masses in the habitable zone of a M5 star.
The investigation of activity is important to distinguish between a wavelength shift caused by activity and a shift based on radial velocity. Activity-induced radial velocity shifts are wavelength dependent, whereas orbital variations are not. Thus, both wavelength ranges are required to measure the activity level in the optical range and to use the high photon number in the infrared range. The wavelength dependence can also be used to get information on the temperature and the distribution of star spots.

The aim of this thesis is the spectral analysis of target stars from the CARMENES input catalog CARMENCITA. It is important to filter out the most promising targets to use the rare observation nights as best as possible. 900 spectra taken from 364 different stars are analyzed to determine their spectral type, radial velocity and an activity indicator of the H_α line with a self-written automatic analysis procedure. With this and further investigations, e.g. on rotational velocities, the stellar properties listed in the input catalog can be defined more precisely and thus, the selection of target stars can be simplified. The spectra were taken using three different spectrographs: FEROS (Fiber-fed Extended Range Optical Spectrograph) at the European Southern Observatory in La Silla, Chile, CAFE (Calar Alto Fiber-fed Echelle spectrograph) at Calar Alto Observatory, Spain, and HRS (High-Resolution Fiber-Coupled Spectrograph of the Hobby-Eberly Telescope) at McDonald Observatory, Austin, USA. Only for FEROS and HRS data was available as reduced spectra.

Chapter 2 of this thesis introduces to the theoretical background of spectroscopy. The way a spectrum depends on temperature and the determination of spectral types are presented. Additionally, the reduction of an Echelle spectrum is described in this chapter. After this, part 3 characterizes the used methods and problems.

The reduction process and the analysis procedure are displayed in detail. Chapter 4 gives an overview of the results which will be discussed in chapter 5. The thesis closes with a conclusion of the results.

2. Theoretical Background

2.1. Basics of Spectroscopy

2.1.1. Black body radiation

Every body with a temperature $T > 0\ K$ emits electromagnetic radiation. In an ideal case the spectrum of a black body is produced by a perfect absorber (hence the name black body) in a thermal equilibrium. According to the *Law of Planck* the spectrum of a black body depends only on temperature T (Weigert et al., 2009):

$$B(\lambda, T) = \frac{2hc^2}{\lambda^5} \cdot \frac{1}{\mathrm{e}^{\frac{hc}{\lambda k_B T}} - 1}, \tag{2.1}$$

where λ describes the emitted wavelength, h Planck's constant, c the speed of light in vacuum and k_B Boltzmann's constant.
Thus, a black body spectrum shows only a continuum without emission and absorption lines. The spectrum of stars can only be seen as an approximation of a black body spectrum and the higher the temperature, the better the approximation holds. Figure 2.1 shows a flux distribution of black body spectra for different temperatures. It is clear to see that the maximum of the spectral energy distribution moves to shorter wavelengths for higher temperatures (blue or ultraviolet ranges) and to longer wavelengths for low temperatures (red and infrared). In addition, the black body irradiation of the whole spectrum drops down strongly with lower temperatures. An integration over all wavelengths gives the area brightness F of a black body as follows:

$$F \ = \ \sigma T^4. \tag{2.2}$$

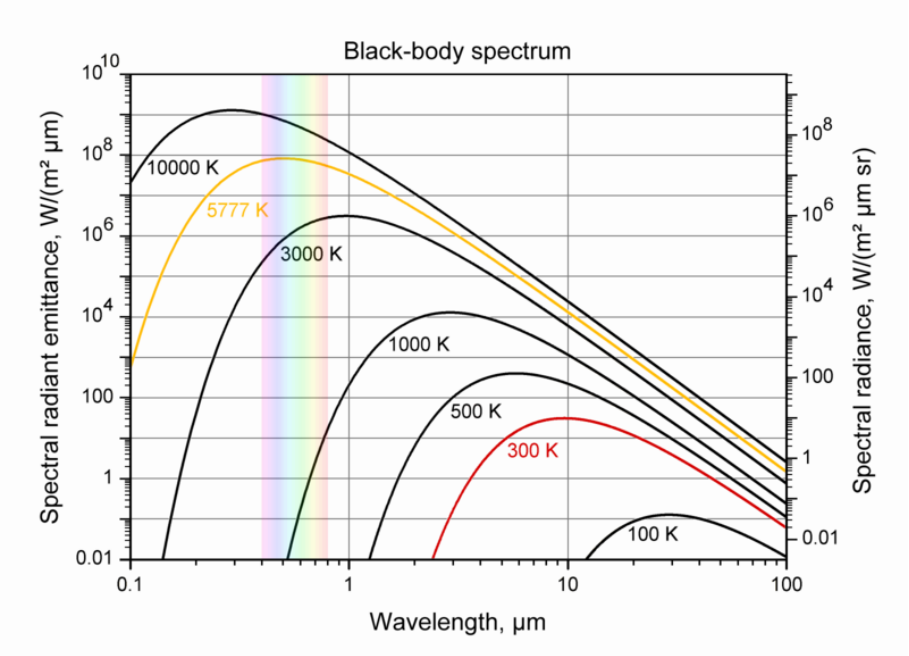

Figure 2.1.: Black body spectra for different temperatures. The spectra with effective temperature of Sun (yellow) and Earth (red) are highlighted.

The proportional constant $\sigma \approx 5.67 \cdot 10^{-8} W m^{-2} K^{-4}$ is the constant of Stefan Boltzmann. Here the strong decrease of the black body irradiation with temperature is easy to see because of its temperature dependence to the power of 4. Additional information on a black body spectrum is given by the position of the maximum of the energy distribution. For every temperature T there is a peak wavelength λ_{max}. λ_{max} and T are connected by Wien's displacement law (Weigert et al., 2009):

$$\lambda_{max} \cdot T \;=\; const. \;\approx\; 0.002879\ Km \tag{2.3}$$

With this relation a star's spectrum can be fitted to the best matching black body spectrum using its temperature as the effective temperature of the star.

2.1.2. Absorption and emission

If the spectrum of a star were equal to a black body spectrum, it would not give much information about the structure and properties of the star. In real spectra there are additional effects that deviate from an ideal black body such as the effects of absorption and emission. To understand the processes that result in emission and

absorption lines it is important to look at the energy levels of electrons in an atom or molecule. These energy levels can only have definite and discrete energy values and thus transitions between two different energy levels need to absorb or emit a specific amount of energy which is equal to the difference of both energy levels. If a photon with this specific energy interacts with an electron it will be excited to a higher energy level. Due to thermodynamical laws a system always wants to minimize its energy, thus the electron can spontaneously return to the lower level. In this case it emits a photon with the specific energy that is equal to the energy difference between the both levels. This emission happens in a random direction which is not connected to the direction of the previously absorbed photon.
In quantum mechanics, the energy levels of atoms and molecules are described by four quantum numbers characterizing a state vector which is an eigenvector of the quantum mechanical Hamiltonian. The appropriate eigenvalue is the energy of this level. From these four quantum numbers the most important one is the principal quantum number $n = 1, 2, 3, ...$ increasing to higher numbers for higher energies. Every state with principal quantum number n can be divided in $l = 0, 1, 2, ... < n$ sub-states by the azimuthal quantum number l. Furthermore these sub-states can be subdivided by the two remaining quantum numbers: the magnetic quantum number and the spin quantum number.
As described above, electrons are able to jump between two energy levels by absorbing or emitting photons. The energy of a photon can be described by its wavelength λ or its frequency ν as:

$$E = h\nu = \frac{hc}{\lambda}. \tag{2.4}$$

If photons are removed from a spectrum by absorption, these photons and their energy are missing at their specific wavelength in the spectrum. This leads to downwards pointing lines called absorption lines. The contrary effect for which photons with specific wavelengths occur produces upwards pointing lines called emission lines. As an example, Figure 2.2 shows the energy levels of a hydrogen atom. Some possible transition series are drawn which are named by their discoverers. Especially the Balmer-Series plays an important role in spectroscopy.
Figure 2.3 shows examples of spectra with absorption and emission features, while 2.4 gives an overview on the distinctions of the origins of absorption an emission lines. Energy levels of a specific atom have always the same energy value. Thus,

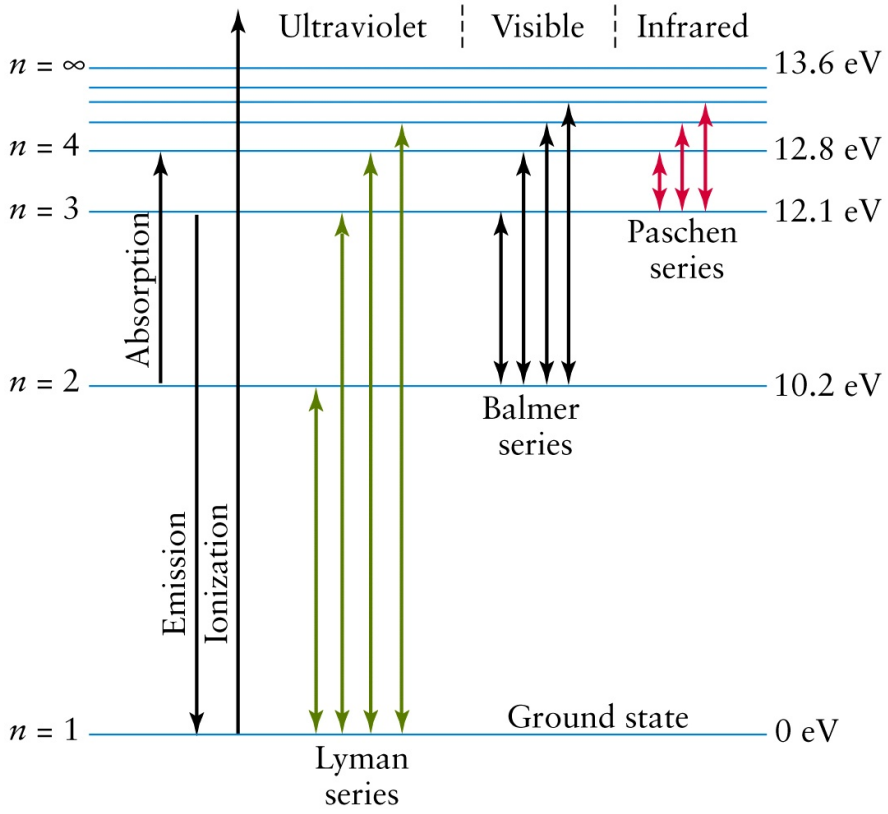

Figure 2.2.: Atomic transitions of a hydrogen atom. The transitions between two principal quantum numbers lead to several line series. Only the Balmer series, containing the H_α line, emits light at optical wavelengths and plays an important role for the observation of stars.

.

emission and absorption lines of a specific transition can always be found at the same wavelengths. This, in turn, gives the possibility to gain information about the composition of objects. Furthermore, the profile or shape of lines gives information about additional properties, e.g., temperature, surface gravity and rotational velocity.

Occupation of energy levels and transitions between them are affected by some rules which prohibit a few of these transitions. The most important of these rules is the Pauli Principle. It excludes the possibility that more than one electron of an atom or molecule can have the same quantum number configuration. Two electrons must be distinguishable in at least one quantum number (Tipler et al., 2004). This leads to the effect that an atom with k electrons is at its lowest energy state if the k lowest energy levels are occupied. In this case a spontaneous emission is not possible. In addition there are more rules for transitions between two levels. While the tran-

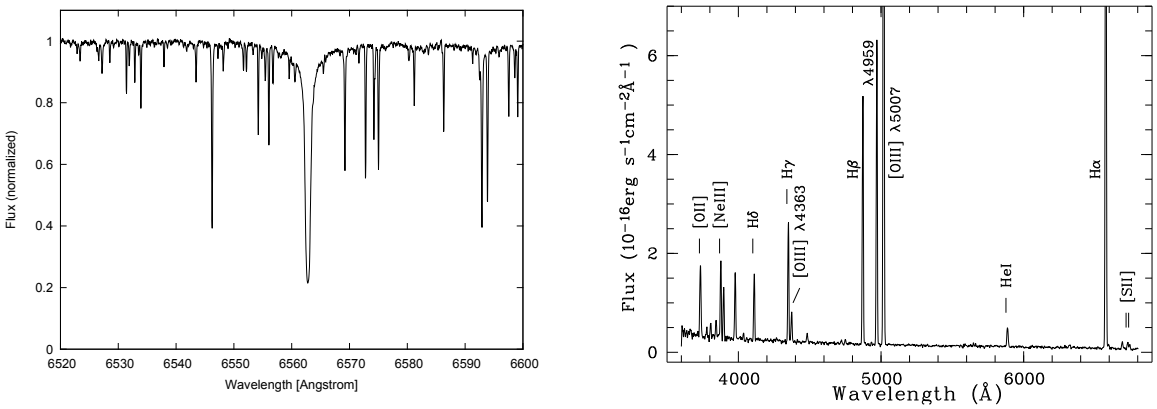

Figure 2.3.: Example spectra of absorption and emission lines. The left hand image shows a spectrum with absorption lines of HD4628 taken with FEROS in the range around H_α, the deepest line at the center. The right hand spectrum is adopted from Kniazev et al. (2000) and displays a galaxy emission spectrum of HS 0822+3542.

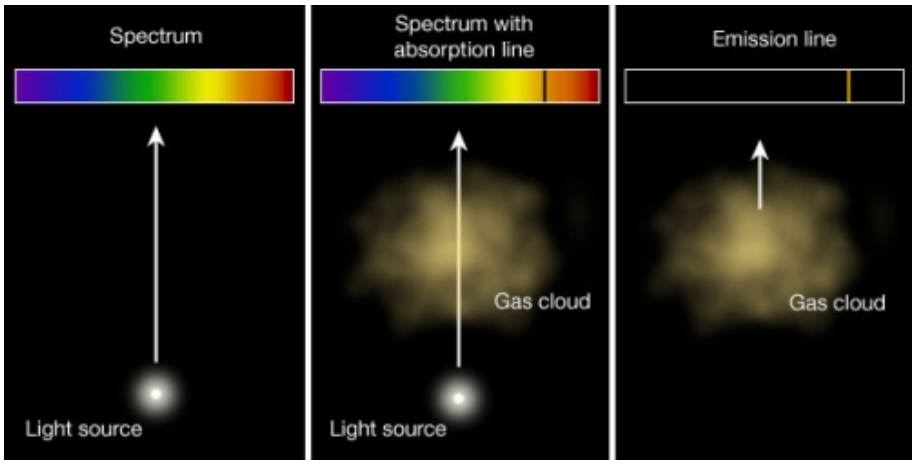

Figure 2.4.: Origin of absorption and emission lines. A single light source radiates a continuous spectrum. If the light travels through a gas cloud the gas atoms can be excited and the photons disappear. These missing photons can be seen as absorption lines. After a specific amount of time the electrons fall back to a lower energy level and emit new photons with the same wavelength than before. An observer of the gas cloud sees only emission lines in the spectrum of the cloud.

sition between two principal quantum numbers is free, the difference between two azimuthal quantum numbers must be $\Delta l = \pm 1$. The same counts for the magnetic quantum number, but this one must not be changing. So it applies $\Delta m = 0, \pm 1$.

All of these rules limit the possible number of spectral lines.

2.1.3. Line profile

A line profile, i.e. the shape, width and depth of a line, is affected by many physical processes. It can be strongly influenced by a stars temperature, pressure and chemical composition. In context of stellar atmospheres the pressure is expressed by the stars surface gravity g.
Here the focus will be mostly on the temperature influence because it determines mainly the stars spectral type. Very important in this aspect is the so-called Doppler broadening. Based on the temperature of a medium, its particles show a statistical Maxwell energy distribution. This implies a similar distribution of velocity and therewith higher velocities at higher temperatures in average. The directions of the particle motions are not aligned and uniformly distributed. Due to this effect some particles on a star's surface will travel in the direction of the observer and some will travel away. As described in the section above this motion leads to a red, respectively blue shift and thus a broadening of every spectral line will be produced. This temperature effect broadens a line profile to a Gaussian function whose width increases with $\sqrt{T}$ (Weigert et al., 2009). In Figure 2.6 the line broadening effect by particle motion is shown.
In addition to the line broadening by temperature the width of a line is also affected by the rotation of a star. During the rotation a part of the star moves towards Earth and generates a blue shift in the light radiated by this part. On the other side a red shift is affected by the part of the star moving away from Earth. Both, blue and red shift produces a broadening of spectroscopic lines.

As described in Section 2.1.2 a spectroscopic line is only visible if electron transitions are feasible. To make this possible for emission lines the high energy level must be occupied by many atoms while the lower energy level must be almost empty. The level of occupation of an energy level depends on temperature. Thus, the strength of a line is influenced by temperature, too. Statistically, the number of electrons n_s in a atomic state s with energy E_s relative to the number of electrons in the ground state n_1 is given by the Boltzmann equation (Weigert et al., 2009):

$$\frac{n_s}{n_1} = \frac{g_s}{g_1} \mathrm{e}^{-E_s/k_B T}, \tag{2.5}$$

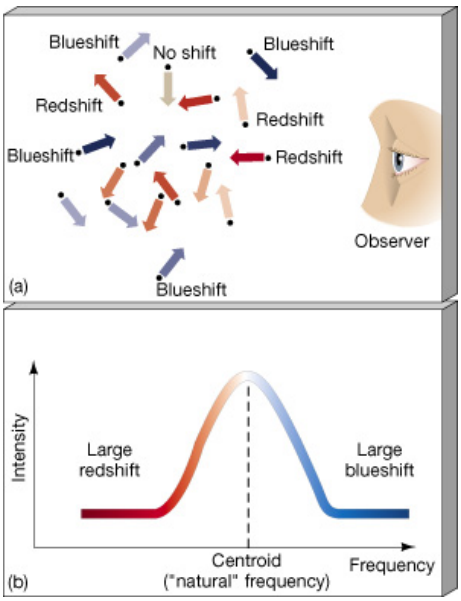

Figure 2.5.: Line broadening affected by particle motion in the photosphere of a star. A higher temperature leads to a higher particle velocity and thus to a higher broadening.

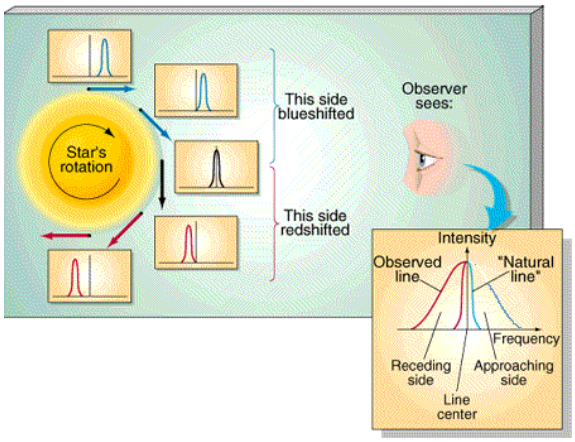

Figure 2.6.: Rotation of a star broadens a specral line. The light coming from the part of the star moving towards Earth appears blue shifted. The other side of the star moving away from Earth is red shifted.

with g_s and g_1 the statistical weights of the states, determined by their degeneration. This equation shows that the higher the temperature the more electrons occupy higher states.

In addition a higher temperature raises the degree of ionization and thus more electrons are free. With this, the electron pressure increases and hence the opacity. This temperature dependence of a line's profile and strength gives the opportunity to use

very temperature sensitive lines to determine the spectral type of a star.

Not the shape, but the position of a line in a spectrum is influenced by the relative motion between Earth and an observed star. This effect can be used to investigate the radial velocity between this two bodies and to detect small velocity shifts indicating a planet orbiting the star. The velocity of the motion between Earth and star is mainly determined by the different rotational velocities of star and sun around the galactic center of the Milky Way and the rotation of earth around the barycenter of our solar system. For far distant stars the expansion of the universe will be noticeable and prevail for very high distances. But for such high distances single stars can not be resolved (Weigert et al., 2009).
Caused by the Doppler effect the frequencies and with this the wavelengths of the emitted light change. This wavelength shift depends only on the radial component of the relative velocity between star and Earth and can be calculated by (Weigert et al., 2009):

$$\frac{\Delta\lambda}{\lambda} = \frac{\lambda - \lambda_0}{\lambda_0} = \frac{v_r}{c}. \tag{2.6}$$

λ describes in this equation the observed wavelength and λ_0 the wavelength in a system in rest. For radial velocities $v_r < 0$, i.e., star and observer are coming closer the spectrum is shifted to shorter wavelengths and appears blue shifted. In the contrary, if star and observer are moving away from each other the spectrum appears red shifted at longer wavelengths.
Therewith an opportunity to measure the radial velocity of a star is given by measuring the wavelength of spectral lines in a star's spectrum and in a non-moving system on earth. It is even possible to convert all wavelengths of a observed spectrum to a system in rest by using Equation 2.6 if v_r is determined.

2.1.4. Detection of exoplanets - the radial velocity method

For around 20 years the gravitational influence of extrasolar planets on the light curve of their host stars can be detected. It is important to note that not only the planet is traveling around the star but both star and planet orbit their center of mass and thus, the motion of the star leads to an alternating radial velocity shift. The velocity of a star is much smaller than its planet's orbital speed due to the much higher mass of the star. With frequent observations it is possible to find periodic

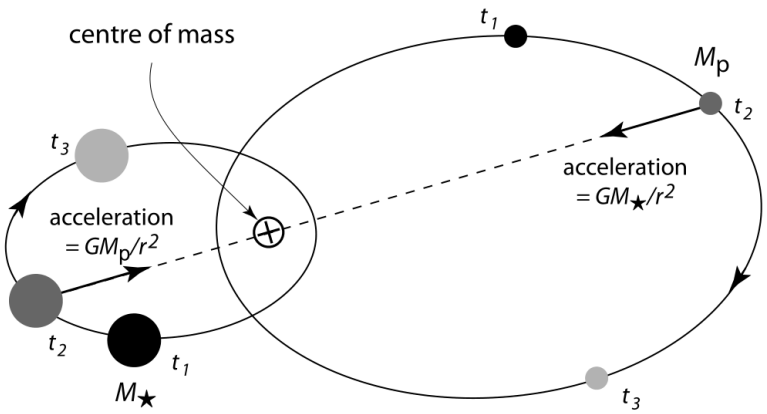

Figure 2.7.: Two bodies, a star and its planet, orbiting their center of mass. The motion of the planet induces a motion of the star which can be seen as a periodic shift of the radial velocity function. Adopted from Perryman (2011).

oscillations in a stars radial velocity which can provide evidence for exoplanets. The first detection of an exoplanet orbiting a solar-like star, 51 Pegasi b, was performed by this radial velocity method. The measured radial velocity oscillation of the host star is shown in Figure 2.8.

It is important to correct the measured radial velocity by the barycentric motion of Earth. This can easily be done by computer algorithms, e.g. the IDL routine *baryvel*. If a periodic shift in the observed light curve remains after the removal of this effect it is fair to assume the shift to be caused by an extrasolar planet. Properties of the planetary body can be calculated with the period P and amplitude K of the radial velocity function.
With the third Kepler law the mass of a planet and K are connected by (Clubb, 2013):

$$K = \left(\frac{2\pi G}{P}\right)^{\frac{1}{3}} m_P m_{star}^{-\frac{2}{3}} \frac{1}{\sqrt{1-e^2}} \sin i. \tag{2.7}$$

Equation 2.7 shows how the observed velocity amplitude depends on the planetary mass m_P, the inclination i, the mass of the star m_{star} and the eccentricity e of a planets orbit. G is Newton's gravitational constant.
With further observations, e.g. from transit measurements (see Perryman (2011)) the inclination can be approximated by $i \approx 90°$. If additionally a nearly circular

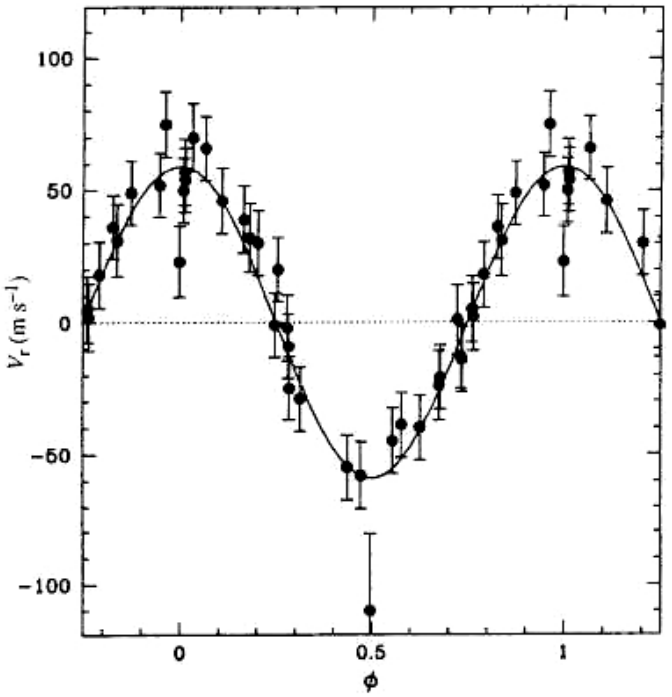

Figure 2.8.: The first detection of an exoplanet orbiting a solar-like star. The planet 51 Pegasi b induce a periodic radial velocity shift to its host star. Adopted from (Mayor & Queloz, 1995).

planetary orbit is supposed the eccentricity gets to $e \approx 0$ and Equation 2.7 simplifies to

$$K = \left(\frac{2\pi G}{P}\right)^{\frac{1}{3}} m_P m_{star}^{-\frac{2}{3}}. \tag{2.8}$$

The distance between planet and star (more accurate: the semi major axis) is a further outcome of the third Kepler law (Perryman, 2011):

$$a^3 = \frac{G(m_{star} + m_P)}{4\pi^2} P^2. \tag{2.9}$$

m_P can be neglected here, since the star is much heavier than the planet.
The last important property of the planet is its radius. It can be determined by a transit measurement. While transiting, the planet covers a part of the star's surface and due to this the star's light curve drops down a little bit. This decrease is connected to the squares of the radii of the star (R_{star}) and the planet (R_{planet}) as follows:

$$\frac{F - F_{transit}}{F} = \frac{R^2_{planet}}{R^2_{star}}. \tag{2.10}$$

Here, $F_{transit}$ is the measured flux from the star during transit time and F the flux while no planet covers the stars.

2.1.5. Stellar activity

The motion of conductive plasma inside stars generates a stellar magnetic field according to solar dynamo theory (Voigt, 2012). This effect destroys the primordial magnetic field and generates a dipolar magnetic field. Due to the differential rotation (different angular velocities at different latitudes) the magnetic field lines are wounded into flux ropes. So the field can become highly concentrated.
At a stars surface magnetic field loops can form starspots (called 'sunspots' on the Sun) when the magnetic field lines break through the surface. Since the strong magnetic field constrains convection, the starspot areas cool down and appear darker than ambient areas on the surface. When magnetic field loops come close together a magnetic reconnection can lead to acceleration of charged particles out of the star (Voigt, 2012). This particles form a sudden flash of brightness called flare which is often connected to a coronal mass ejection. Spectra taken while a flare event happens show different properties compared to normal spectra. Lines like, e.g., CaII λ8662, H_α and other Balmer lines (Montes et al., 2004) get emission lines and can be used as indicators for activity.
In this thesis the H_α line will be used to identify active stars and to calculate the brightness ratio of H_α and the bolometric brightness $A := \log(L_{H\alpha}/L_{bol})$. This brightness ratio can be determined by the equivalent width of H_α, EqW(H_α), and a χ-factor depending only on temperature (Reiners & Basri, 2008):

$$A = \log(L_{H\alpha}/L_{bol}) = \log(\chi \cdot \mathrm{EqW}(H_\alpha)). \tag{2.11}$$

Reiners & Basri (2008) calculated χ by a fifth-order polynomial fitted at a function showing logarithmic H_α luminosity versus temperatures for PHOENIX spectra (Hauschildt, 1992).

The equivalent width is defined by the width of a rectangle with the same height as the continuum level and the same area as the line profile. With this definition an emission line gets a negative equivalent width. In contrast to the common definition, here emission lines are used with a positive value to be able to calculate the logarithm of $L_{H\alpha}/L_{bol}$.
Active stars with large star spots can pretend the existence of an exoplanet, although there is no. Like described before the rotation of a star broadens its spectral lines. If now a star spot is located on one side of a star the amount of light coming from this side is lower than the amount of light emitted from the other side because the star spot is cooler than the normal surface. This effect is leading to unsymmetrical line profiles and to a shift of the line grounds pretending a radial velocity shift. Since the star is rotating the star spot is alternating located at the one and the other side. Thus, an alternating red and blue shift of the spectrum is produced. The generated radial velocity can be similar to the signal produced by an exoplanet. Thus, it is important to filter out very active stars from a target list for exoplanet search. Investigations on the effect of magnetic activity on the radial velocity accuracy can be found in, e.g. Saar & Donahue (1997) or Lovis et al. (2011).

2.2. Data Reduction

2.2.1. Spectrographs

For analyzing the light of a star a spectrograph is used. This instrument separates light into a wavelength spectrum and records the result using a camera. In general, an optical component of the spectrograph diffracts light with different wavelengths to different positions on a screen or camera to make them visible. This component can be a prism or a diffraction grating. In modern astronomy only gratings are used. For this thesis data taken with Echelle spectrographs, a special type of diffraction gratings is used. It consists of two gratings rotated 90° with respect to each other and placed close to one another. In a single grating a specific wavelength is diffracted to the central zero order or successive higher orders at specific angles. The angular separation between higher orders decreases, so they can get very close to each other. For multiple wavelengths it can be possible that longer wavelengths of a higher order might overlap with the order of a shorter wavelength. In an echelle spectrograph this unwanted effect is eliminated by using the second grating as cross disperser

separating the spectrum in multiple orders overlapping at their edges. With the use of this, the spectrum is displayed in two dimensions on the CCD camera (*charge-coupled device*) to record broadband, high-resolution devices.
In this thesis data taken from three different spectrographs are used:

CAFE

CAFE (Calar Alto Fiber-fed Echelle spectrograph) is an Echelle spectrograph installed at the $2,2\ m$ telescope at Calar Alto Observatory, Spain. It was developed to replace the FOCES spectrograph (Pfeiffer et al., 1997) that was being operated until 2010. With a resolution of $R = 62000 \pm 5000$ a wavelength range of 3650 Å to 9800 Å in 84 orders is covered. CAFE was developed to measure radial velocities with an accuracy of some 10 ms^{-1} for stars with $J \approx 13..14\ mag$ (Sánchez et al., 2009) and to achieve a SNR of 30 for a star with a brightness of 14.5 mag and an exposure time of 2700 seconds. It was constructed as a simple and unexpensive, fast track instrument for a maximum radial velocity accuracy to search for exoplanets. CAFE operates only in a single mode with no possibility to increase the resolution or the efficiency. A CCD camera of 2048x2048 pixels of 13.5 μm is used the record the spectra. For CAFE just the raw data were given, hence a reduction had to be done separately. More details to CAFE can be found in, e.g., Sánchez et al. (2009).

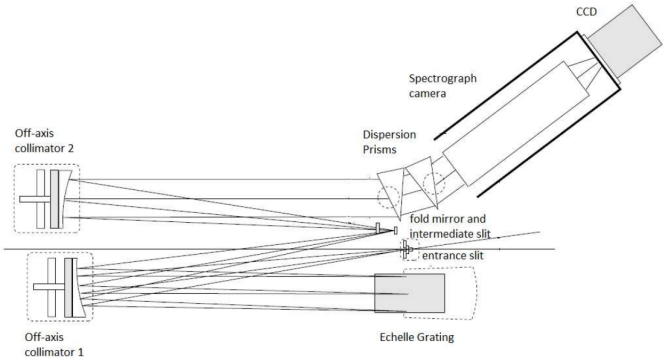

Figure 2.9.: Sketch of the optical system of the CAFE spectrograph. Adopted from Sánchez et al. (2009).

FEROS

Additional data was taken with FEROS (Fiber-fed Extended Range Optical Spectrograph) at the ESO 1.52-m telescope located at the European Southern Observatory in La Silla, Chile. FEROS is able to observe a spectral range from 3700 Å to 8600 Å

with $R \approx 48000$. The accuracy of radial velocity determinations is given as 10 ms^{-1} (Kaufer et al., 1999). FEROS uses in contrast to other spectrographs a 55° prism with a base length of 235 mm as crossdisperser what provides access to the full wavelenght range together with a high efficiency. The CCD chip consists of 2048x4096 pixels with a size of 15 μm. For an exposure time of 2 h a magnitude limit of 16 mag for a SNR of 10 and a limit of 12 mag for a SNR of 100 in the V-Band is expected. Like CAFE, FEROS can operate only in a single mode. Data sets for FEROS were reduced by the FEROS pipeline *DRS* (Kaufer et al., 1999). Hence, they could be analyzed immediately without further reduction steps and were available as *fits*-files with data for every order and as complete merged spectrum.

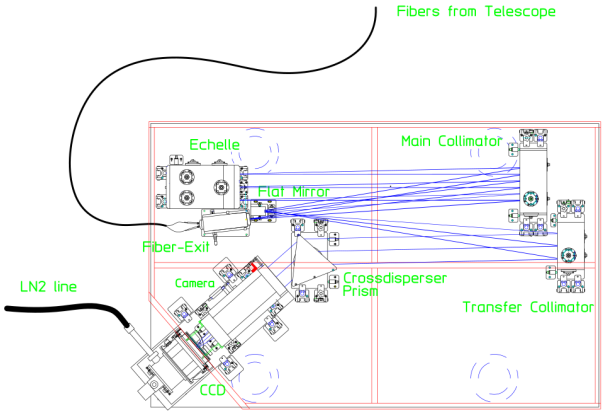

Figure 2.10.: Optical system of the FEROS spectrograph on the optical bench. Adopted form Kaufer et al. (1999).

HRS

A third sample of spectra was taken with HRS (High-Resolution fiber-coupled Spectrograph). This fiber spectrograph is installed at the Hobby-Eberly Telescope, McDonald Observatory, Austin. With the detection of exoplanets the telescope was extended by the HRS spectrograph to use high-resolution spectra to search for Extra-Solar Systems and to investigate the formation and early stages of them. A mosaic of two chips can be used to observe stars in a wavelength range from 4200 Å to 11000 Å and a resolution from $R = 30000$ to 120000. The resolution can be changed to adjust the spectral resolution. For $R = 60000$ the spectral resolution element is four pixels. Each chip contents 2048 x 4096 pixels with a size of 15 μm (Tull, 1998). For a resolution of $R = 60000$ and an exposure time of 1h

stars with a V-band brightness of 14.4 *mag* can be observed with a SNR of 100 and for a brightness of 19.4 *mag* with a SNR of 10. The spectrograph was developed to find exoplanets with a wavelength stability better than 10 ms^{-1}. HRS spectra were available in a final reduced format produced by Mathias Zechmeister at the Institute of Astrophysics, Göttingen. The reduced spectra and all interim steps were provided.

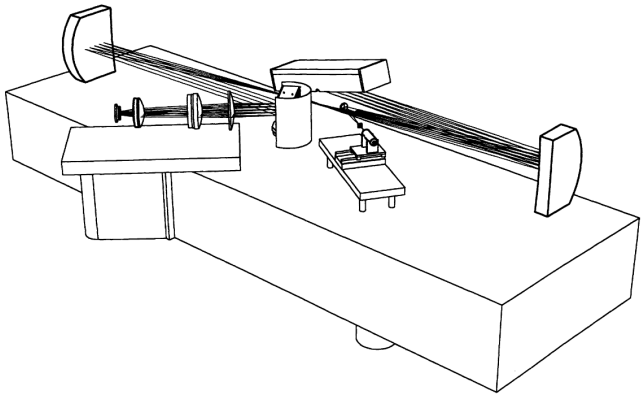

Figure 2.11.: Perspective view of the optical bench of the HRS. Adopted from Tull (1998).

To analyze a spectrum the frames of the CCD camera must be converted into a function flux versus wavelength. In the following sections the reduction of CCD frames to a spectrum will be described.
A CCD frame displays just the brightness of every pixel meaning the flux $F(x, y)$ depending on the pixel position (x, y). Aim of the data reduction is to convert this two-dimensional flux frame into a one-dimensional wavelength depending flux function $F(\lambda)$.
To enable this, among the science spectrum frame some other frames are required to remove contaminating effects, e.g. artifacts on the CCD camera or the Blaze function, or the additional frames are needed to calibrate the wavelength positions on the frames.

2.2.2. Data types

Science Frame

The science spectrum is the frame of a star observed with a spectrograph. This frame contents the important information of the star. It will be reduced by the

additional frames to the spectrum.
The star's spectrum forms several lines (orders) on the science frame. For wide wavelength ranges it is important to divide the spectrum into these orders because the chip is not broad enough to scan the spectrum in one dimension. Thus, the spectrum must be divided in parts which overlap at the end and begin of each order, in best case. These orders lie next to each other on the two dimensional chip. Figure 2.12 shows an example of a Science Frame in the top left picture. In Figure 2.13 a zoomed-in image of a few orders is displayed.

Dark Frame

During the exposure of a frame, thermal noise contaminates the signal of a spectrum. This noise is not equally distributed over the frame and changes from pixel to pixel. To remove this effect, dark frames can be taken for non- or low-cooled cameras. With a closed prime lens, when no light can enter the spectrograph, a frame is taken. This must have the same exposure time and the same temperature compared to the science spectrum in order to get a frame containing Dark and Bias (see next section). To eliminate statistical outliers a master dark can be calculated by averaging a series of dark frames. This master dark must be subtracted from the science spectrum. The dark current depends exponentially on the temperature. Therefor, the CCD cameras must be cooled and kept by a constant temperature over the complete exposure time. For the used CAFE data no Dark Frames were provided, so they are not shown in Figure 2.12.

Bias Frame

In addition to thermal noise, errors occur during the read-out of the CCD chip. For a perfect CCD a frame with exposure time 0 s and a closed prime lens should theoretically have the same read-out value in every pixel. However, in reality the readout values are all different. A frame taken with the properties described before (i.e. minimal exposure time) can be used to eliminate the read-out noise from the Science Spectrum and Dark. Like the master dark a master bias can be averaged to decrease statistical outliers. Figure 2.12 shows a Bias Frame in the bottom left picture.

Flatfield response frame

The illumination of a CCD chip is not equally distributed over the whole chip. Therefore, it is important to take a flatfield frame. To do this, the spectrograph is illuminated by a bright lamp with a wavelength independent flux. In general, the center of the chip is more illuminated than the edges (vignetting) and specific areas get more light due to reflexions. Like the Bias and the Dark the Flatfield frames can be averaged to a masterflat. With a normalization to 1 the masterflat is used to correct the science frame for influences of unequal illumination by dividing the science frame by the masterflat. The top right image of Figure 2.12 shows a Flatfield of CAFE.

Wavelength Calibration

To find the wavelength of each pixel position on the CCD chip a calibration frame with a Thorium-Argon-Lamp (ThAr) is used. The known wavelengths of the emission spectrum are dedicated to specific positions on the CCD which are the same for the ThAr frame and the science frame. An example of a ThAr spectrum can be seen at the bottom left corner of Figure 2.12.

2.2.3. Disturbing Influences

In addition to the effects previous mentioned there are more effects complicating the data reduction. Below, these are shortly characterized:

Cosmics

For long exposure times of the science frame (necessary for the observation of low mass star because of the small amount of emitted light) the probability rises that cosmic particles hit the CCD chip. Due to their high energy a strong, bright signal is produced in one or more pixels (see 'Blooming'). This signal is stronger than the signal from star light leading to small, high peaks in the spectrum if they hit one of the orders and not be removed from the spectrum. Depending on its direction the cosmic particle can hit a single pixel or a row of them. In Figure 2.13 Cosmics can be seen as small dots between the orders.
Cosmics can be removed from the spectrum by a program searching for high peaks and smoothing them. Because one cosmic appears only on one single frame they

must be removed from every frame separately.

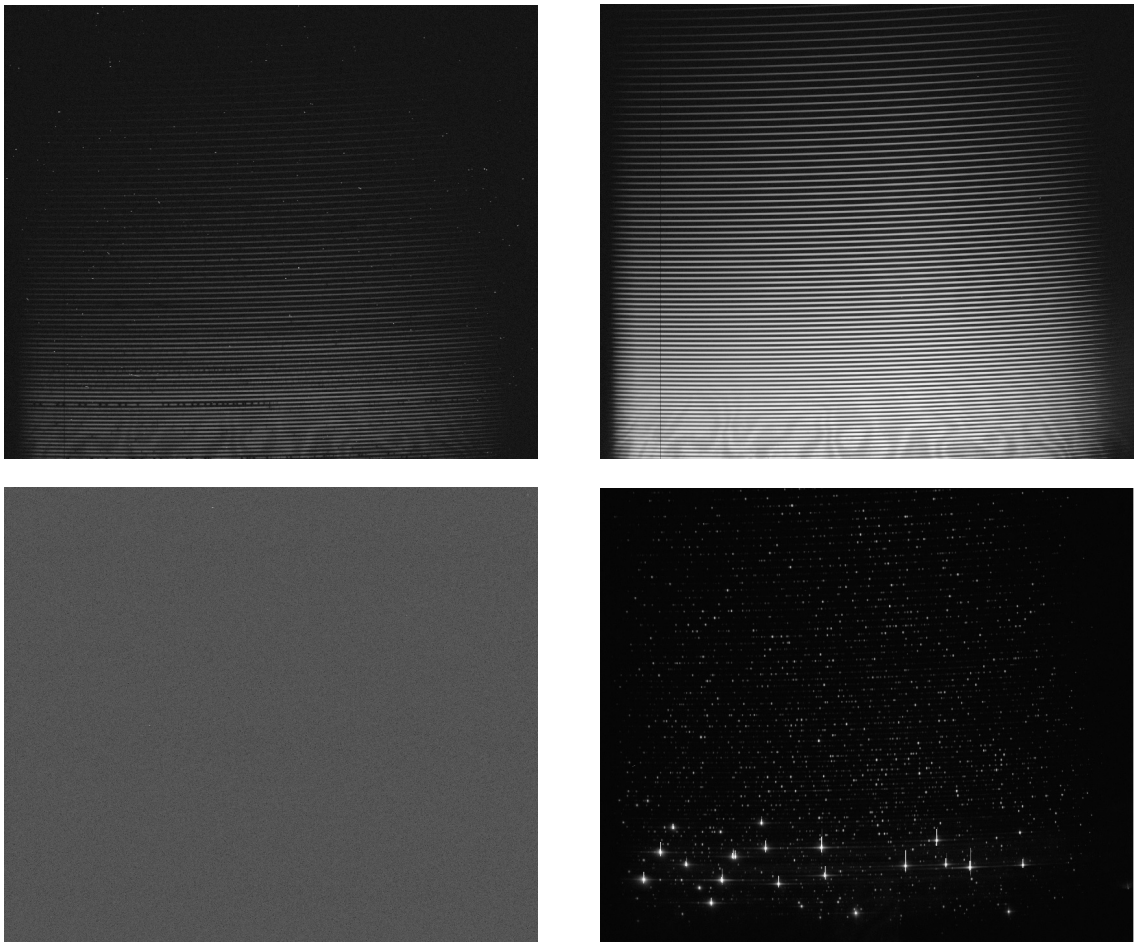

Figure 2.12.: Examples for a Science spectrum (top left), a Bias (top right), a Flat (bottom left) and a ThAr emission spectrum (bottom left) taken by the spectrograph CAFE. All frames are plotted with a logarithmic brightness scale to get a higher contrast.

Fringing

Due to reflections in the picture frame glass, interferences on the CCD can be produced leading to blurred patterns on all frames. This effect occurs especially for infrared light when the thickness of the CCD chip gets the same dimension than the wavelength and produces local reflections (Reiners & Jeffers, 2013). In most cases effects of Fringing can be eliminated by flatfielding but for fiber spectrographs problems may occur when the frame is differently illuminated by the star and the

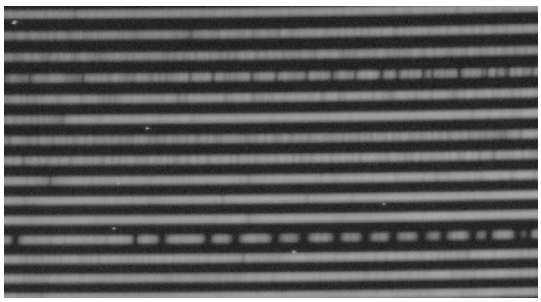

Figure 2.13.: Zoomed-in image of the Science Frame showing absorption lines as gaps in the orders and cosmics as small dots between orders. If a cosmic hits an order the signal of these pixels will be intensified leading to small peaks in the spectrum.

flat field lamp (Reiners & Jeffers, 2013). In Figure 2.12 Fringes can be seen at the bottom of the flatfield.

Stray light

Reflections in the optical system itself scatter light onto the chip. This light is called stray light. In most cases stray light appears on large scales so it can be removed by a 2D Fourier transformation. By an extraction of low frequencies the important information be retained and the stray light parts removed.

Airglow

On Science Spectrum frames the star's spectrum forms several orders on the frame like described above. In a perfect case in which nothing is between the telescope and a star all orders would have the same width than the image of the star. This is caused by the effect that the star is displayed in every wavelength on the chip and thus produces the order lines.
However, if the star can not be fixed at the same slit position the star's image can travel up and down in the slit and this broadens the width of the order lines. Especially for faint objects it is complicated to fix the position in the slit.
A second effect broadening order lines is caused by telluric lines (emission lines from Earth's atmosphere). Air in front of the slit emits radiation through the hole slit and this radiation is imaged in the size of the whole slit on the chip.

Blooming

On a CCD Chip incoming photons are converted into electron charges and they are saved in a potential well. When the potential well of a pixel is exposed too much, the potential well can get 'filled' that means saturated and 'overflow'. Then charges flow in neighbor pixels and fill them, too. Thus, a neighbor pixel can also be filled and overflow into its neighbor pixel. Because of the structure of a CCD this flow goes more easily in one direction leading to a vertical streaking. In Figure 2.12 the ThAr spectrum shows examples of blooming.

Sky Background

Not only light from the observed star enters the spectrograph. The background of the sky also emits radiation. The influence of this effect depends strongly on the spectrograph type. If a slit is used the background light enters the spectrograph with the star light. Thus, an order line broadening appears because the whole slit is imaged at the chip. This produces a sort of Airglow.

Charge Transfer Efficency

To read out a CCD Chip pixel charges must be transferred from one pixel to the next column by column and line by line. This transfer does not have an Charge Transfer Efficency (CTE) of exactly 100%. Typical values are greater than $0,9999$ (Christen et al., 2006). As a huge number of pixel transfers is required this efficiency can lead to a noticeable loss of charge. For a CTE of $0,9999$ and 1000 pixels per column the last pixel of a row would only get $0,9999^{1000} = 0,9048 \approx 90\%$ of its real charge value. With a known CTE value all pixel values can be corrected afterwards.

2.3. Spectral types

2.3.1. Morgan-Keenan system (MK)

Because of their different temperatures stars radiate with different intensity at different wavelengths. To categorize stars on this effect Pickering and Cannon introduced their *Draper Catalogue* with a spectral class sequence in 1888 (Weigert et al., 2009). After some modifications at the end of the 19th century and the beginning of the 20th William Wilson Morgan, Philip C. Keenan, and Edith Kellman from Yerkes

Observatory extended the system to the Yerkes spectral classification, also called MK System. The MK system is a two dimensional system based on temperature and luminosity of stars. Here more attention is payed to the temperature scale.
The MK System divides stars in different spectral types named with letters

O, B, A, F, G, K, M, L and T

where the brightest and hottest stars are of type O and faint, cool stars in type K and M. Brown dwarfs start in class M and fill the at the begin of the 21st century added classes L and T (Weigert et al., 2009).
The pure qualitative classification and the non alphabetical order is caused by historical reasons. Because the MK sequence shows a temperature sequence the historical sequence with letters A to O was simplified and changed in their order. In the past, astronomers thought the sequence shows the development steps of stars while burning their hydrogen and becoming cooler and fainter with the decreasing available amount of burnable hydrogen. With this idea stars would start in a class on the left side and wander through the sequence from left to right. With the current state of knowledge we know that this concept is wrong. But the old nomenclature calling O, B and A early types, F and G medium types and the remaining ones as late types are still common designations today.
For a more detailed classification all classes can be divided in 10 subclasses labeled with a digit 0-9 after the spectral class from early to late subtypes. But not every possible subclass is used in every spectral class. Some of them are skipped. For example class K ends with K7 while K4 and K6 are skipped (Gray et al., 2009).
From early to late spectral types the maximum of the energy distribution (see section 2.1.1) changes from shorter to longer wavelengths. Thus, the color of the stars goes from blue-white to yellow and red and end in the infrared range for M stars and brown dwarfs. Figure 2.15 shows spectra taken from stars of different spectral types. It is clear to see that class M radiates most light in the infrared regime around 1000 Å. That's why CARMENES is optimized to observe in this wavelength range.

2.3.2. Spectral class M

Stars with spectral class M play an important role in exoplanet research. Because of their low temperature, their habitable zone is very close to the star and therefore

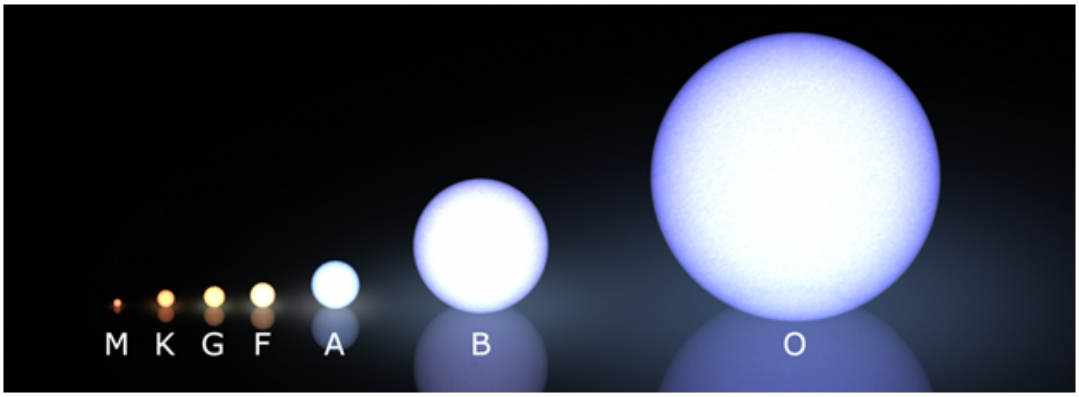

Figure 2.14.: Size and color distribution of spectral classes.

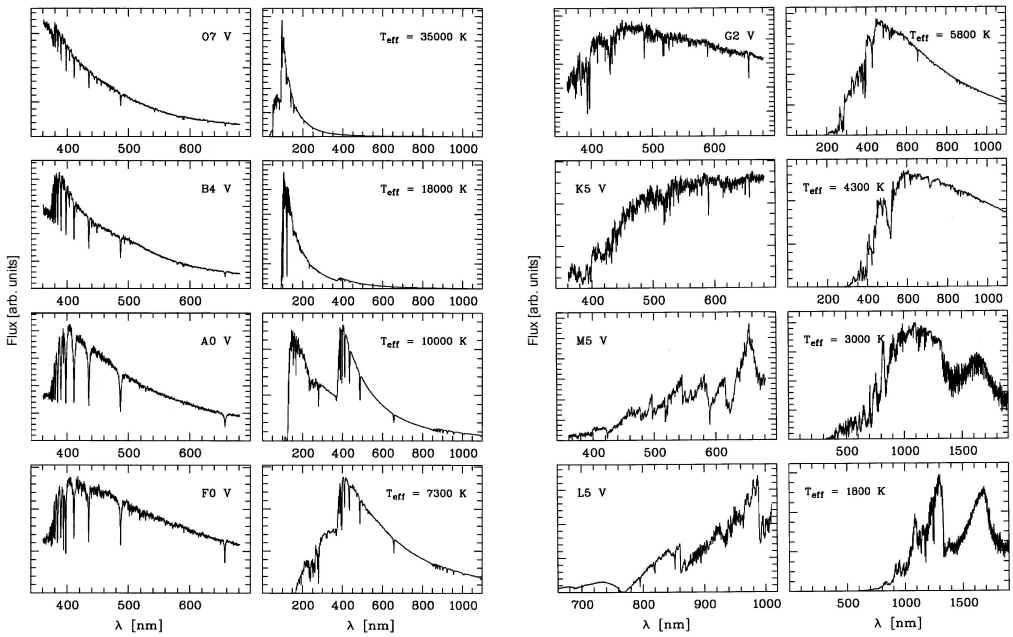

Figure 2.15.: Comparison of spectra from different spectral types. The left hand frames of each doublet show the observed spectra of each spectral type. On the right hand side the spectral energy distribution calculated from models based on the specific temperature can be seen. Note that the shown wavelength range of the M and L star is changed to higher wavelengths. Adopted from Weigert et al. (2009).

it is easier to find planets in there. The CARMENES project will observe M-dwarfs to find Earth-like planets in the habitable zone of these stars.

M-dwarfs are at the end of the main sequence in the Hertzsprung-Russel-Diagram at low temperatures and radiate mostly at high wavelengths in the infrared range (see Figure 2.16). A differentiation of class M and neighbor classes based only on

physical properties is difficult. There are different used methods. Stars fainter than an absolute luminosity of $M_V = 7,5$ can be classified as M (Reid et al., 2000) or with an effective temperature between 2500 K and 4000 K (Giampapa, 2000). A third method is to use standard stars defining all spectral types.
With their low effective temperature M-dwarfs radiate only with a small luminosity, $L \approx 0,0001..0,05\ L_\odot$ (Reid et al., 2000). Due to this the detection and investigation is more complicated than for earlier types. A longer exposure time or multiple observations are needed.

Characteristic features of M-dwarf spectra are not only atomic absorption lines like CaIλ6162, CaIIλ8662 and Hα but also molecular absorption bands, e.g., from TiO, VO und CaH_3. The strength of these lines and bands depend strongly on the effective temperature (see 2.1.3) so they can be used to determine the spectral type of a star.
Based on the mass-luminosity relation (Voigt, 2012) M-dwarfs are low mass stars with a mass around one magnitude smaller than the mass of the Sun. Around 76% of all stars in the sun's neighborhood are M-dwarfs (LeDrew, 2001) so M-dwarfs are thought to be the most common stars in our galaxy. Nevertheless, no M-dwarf can be seen by eye from Earth because of their small luminosity.
M-dwarfs are not only important for investigations in exoplanet research. They can also be used to determine the age of star clusters. With their small mass M-dwarfs burn their Hydrogen very slow and stay in the main sequence for a very long time. Estimations of the life time of M-dwarfs gives values from 10 Gyr to some trillion years (Weigert et al., 2009). The lower end of this estimation and the age of the Universe of $13,7\ Gyr$ lead to the assumption that no or only a few stars have left the main sequence yet (Weigert et al., 2009). With this information and the maximum mass of stars in a cluster which have not left the main sequence it is possible to determine a star clusters minimum age.

In exoplanet research M dwarfs are important objects for the search of rocky planets in the habitable zone. Because of their small luminosity a planet has to orbit very close to the star to stay in the habitable zone. According to the third law of Kepler this leads to a short period time (see Section 2.1.4) what makes it easier to detect the planet. To be sure that the radial velocity shift is caused by a planet it is necessary to observe multiple orbits. Thus, planets with a longer period must be observed for a longer time. A second advantage of observing close orbiting

planets is that they induce a higher radial velocity amplitude to the host star what decreases the required precision to detect them.

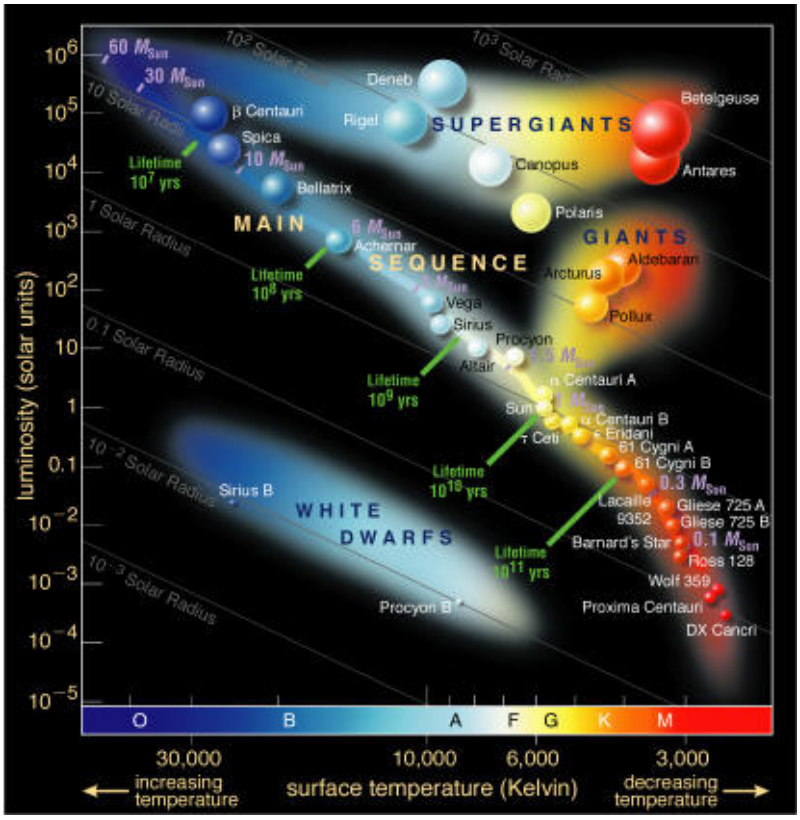

Figure 2.16.: Hertzsprung-Russel diagram showing the effective temperature and the spectral type versus the luminosity of stars. M dwarfs are at the end of the main sequence located in the bottom right corner with a low temperature and a small luminosity. Adopted from Reiners & Jeffers (2013)

2.3.3. Determination of spectral types

The classification of stars into their spectral types can be performed by analyzing the strength of their absorption lines and bands. A classification based only on the effective temperature, i.e. black body fitting, would lead to some problems, e.g. the spectra of several spectral types show big deviations from a perfect model of a black body because of their absorption features. Especially late-type stars show a large amount of absorption lines and large deviations in strength which is caused by the decreasing temperature for later types. For type G or later there are ranges in the spectrum where no continuum can be found (Weigert et al., 2009).

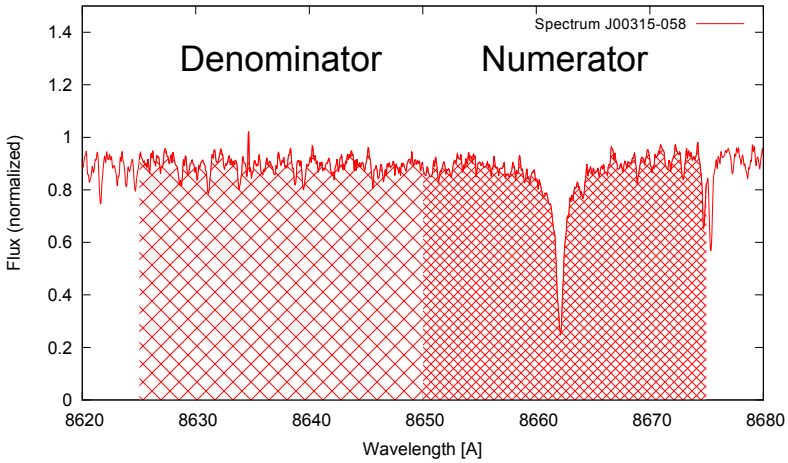

Figure 2.17.: Two different ranges where used to calculate the index value of CaIIλ8662 to determine the spectral type of the star. The integral on the right hand side (Numerator) is divided by the integral at the left hand side (Denominator) to define the index of the spectral line.

Early-type stars show mostly absorption lines of a higher degree of ionization and absorption bands can only be found in spectra of late type stars. This gives an idea which lines can be used to classify stars of different types. It is important to use lines and bands that are strongly effected by temperature but are only weak influenced by surface gravity and metallicity. In this thesis the lines from the project THE HAMMER (Covey et al., 2001) will be used to investigate the spectral types by the calibration functions of this project. Table 2.1 lists the important lines for the spectral typing of M-dwarfs. To determine the spectral type of a star, the spectrum must be corrected by its radial velocity shift first and then be normalized. Using this normalized spectrum the spectrum around an absorption feature is integrated over a specific wavelength range (symbolized by N for nominator, see Table 2.1) and divided by the width of the wavelength range. For discrete data, the average of the flux in this wavelength range becomes equal to this integral for a high number of data points. The same integral is calculated for a wavelength range of the continuum (i.e. with no or only small absorption features), symbolized by D for denominator, and with these two integrals the index value I_{line} of a line can be defined by (Covey et al., 2001):

$$I_{\text{line}} := \text{Index}_{\text{line}} = \frac{\bar{F}(N)}{\bar{F}(D)}, \tag{2.12}$$

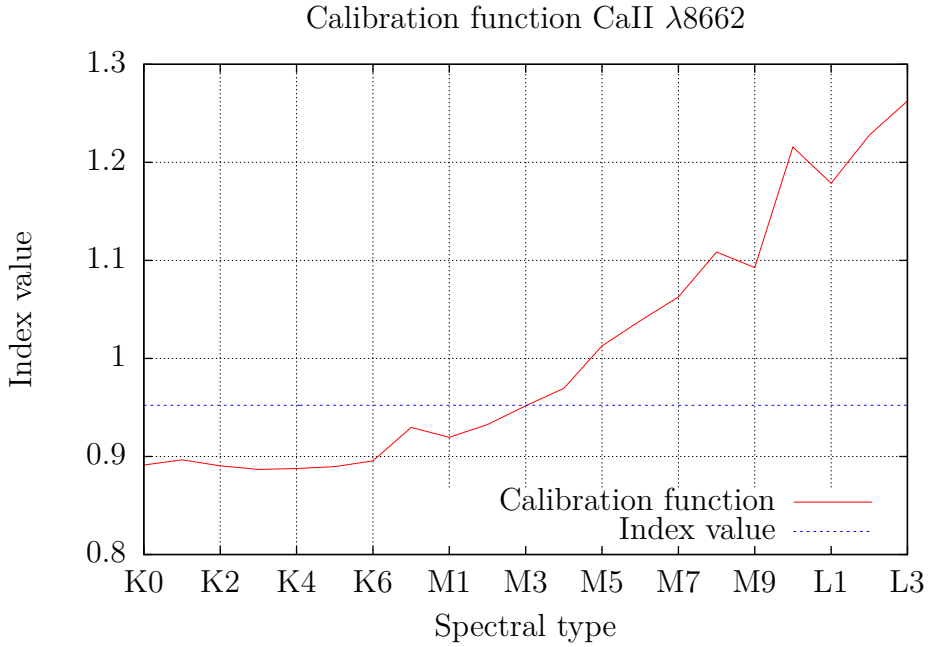

Figure 2.18.: Calibration function for CaII λ8662 with a dummy index value. The intersection of index value and calibration function gives the spectral type.

where $\bar{F}(N)$ is the average flux including the absorption line and $\bar{F}(D)$ is the average flux in the continuum range. A sketch of the integrated ranges is shown in Figure 2.17. For some indices, $\bar{F}(N)$ is composed by two parts. In this case the ranges are marked by $N1$, respectively $N2$. $\bar{F}(N)$ is given by the weighted sum of both averaged fluxes with the weights σ_{N1} and σ_{N2}:

$$\bar{F}(N) = \sigma_{N1} \cdot \bar{F}(N1) + \sigma_{N2} \cdot \bar{F}(N2). \tag{2.13}$$

The error of the index value is mainly influenced by the error of D und is given by (Covey et al., 2001):

$$\sigma_{I_{\text{line}}} = \sqrt{\left(I_{\text{line}} - \frac{\bar{F}(N)}{\bar{F}(D) + \sigma_D} \right)^2} \tag{2.14}$$

while σ_D can be calculated by the the standard deviation $s(D)$ of D and the number of datapoints n_{pix}:

Indexname	$N1_S$	$N1_E$	$N2_S$	$N2_E$	D_S	D_E
CaI λ6162	6150	6175	-	-	6120	6145
CaH 3	6960	6990	-	-	7042	7046
TiO 5	7126	7135	-	-	7042	7046
VO λ7434	7430	7470	-	-	7550	7570
VO λ7912	7900	7980	-	-	8100	8150
TiO B	8400	8415	-	-	8455	8470
TiO λ8440	8440	8470	-	-	8400	8420
CaII λ8662	8650	8675	-	-	8625	8650
VO-a	7350	7400	7510	7560	7420	7470
VO-b	7860	7880	8080	8100	7960	8000
Cs-a	8496.1	8506.1	8536.1	8546.1	8516.1	8526.1

Table 2.1.: Overview of used indices and wavelength ranges. All wavelengths are given in Å. Values with a subscript S shows the left edge of the wavelength range, values with a subscript E the right edge. For molecular bands of VO-a, VO-b and Cs-a two N-areas are used to determine the index value. For VO-b and Cs-a both ranges are weighted with 0.5. For VO-a the first range has a weight of 0.5625, thus the second gets 0.4375 (Covey et al., 2001).

$$\sigma_D = \frac{\mathrm{s(D)}}{n_{\mathrm{pix}}}. \tag{2.15}$$

The broader and the deeper a line the smaller is the average flux $\bar{F}(N)$ around the line. Thus, a smaller index value is the result. THE HAMMER measured for all lines in Table 2.1 (and more for earlier spectral types) a calibration function of index values and spectral types. An example is plotted in Figure 2.18.
Based on the calculated index value a matching spectral type can be found. It is important to use more than one index value because some calibration functions can show different spectral types for the same index value in the crucial ranges. Thus, the best spectral type matching to all calibration functions must be found.

2.4. CARMENCITA Database

CARMENES uses the CARMENCITA (**CARMEN**es **C**ool star **I**nformation and da**T**a **A**rchive) database containing all information about candidate stars (Quirrenbach et al., 2012). Main source of the catalogue is the Palomar/Michigan State

University Survey, PMSU (Hawley et al., 1996, Reid et al., 1995). This catalog contains coordinates, visual magnitudes, distances, proper motions and such indices which were also determined in this thesis, e.g. TiO5, for 1966 stars. The PMSU catalog was cross-matched with the 2MASS point source catalog (Cutri et al., 2003) to include JHK magnitudes. Because of the instrument limits of CARMENES and its site, stars with $J > 11.5\ mag$ and declination $\delta < -23°$ are discarded. The CARMENCITA database is completed by RECONS (http://www.recons.org) for late-type stars, the SLOAN Digital Sky Survey (West et al., 2011), the catalog by Lépine & Gaidos (2011) and additional publications from Bochanski et al. (2005), Irwin et al. (2011) and the Dwarf Archive maintained by Gelino, Kirkpatrick and Burgasser at http://dwarfarchives.org.

3. Methods

The following chapter will give an overview over the analyzing process of all 900 spectra. The reduction process of the CAFE data is also be described and its problems. Table 3.1 shows how many spectra were taken with each spectrograph and how many nights were used for observations in the given period.

Spectrograph	# Spectra	# Obs. nights	Period
CAFE	348	51	2013/01/21 - 2014/04/19
FEROS	401	38	2012/12/31 - 2013/12/31
HRS	151	38	2011/09/29 - 2013/06/18

Table 3.1.: Overview of the period, number of observation nights and number of spectra taken with each spectrograph.

3.1. Used programs

To reduce the CAFE data the IDL freeware package *REDUCE* (Piskunov & Valenti, 2002) was used, which was developed to reduce Echelle spectra. *REDUCE* executes all steps of reduction automatically but is not free from bugs. These will be described in detail in Section 3.3.
In the first step *REDUCE* averages all available Bias Frames to a Master Bias and all Flatfield Frames to a Master Flat. After this, the program is searching for bright lines in one of the Flatfields to define the orders where the spectrum will be extracted. To correct the Science Frames for different illumination the Masterflat is normalized and the Blaze function, describing the illumination profile depending on the pixel position, is calculated. Before the extraction of the Science Frame starts *REDUCE* gets the flux of the ThAr spectra to calibrate the wavelengths later. The flux extraction process of the Science Frame in *REDUCE* works by fitting a profile function to the flux values across an order. This function will be normalized to 1. Subsequently the profile function is fitted for every column to the data. The mul-

tiplication factor between the normalized function and the function in each column is used as the flux value of the pixel column.
This method is time-intensive and worked for CAFE not faultlessly. So, *REDUCE* was extended by the program *Fox* (Zechmeister et al., 2013). *Fox* fits model spectra to the pixel values and eliminates outliers to get the best spectrum.
REDUCE does not have its own wavelength calibration procedure. However, *WAVECAL*, a procedure to compare the wavelengths of a ThAr specrum with the pixel positions on the CCD in each order, can be added very easily. All emission lines were fitted by a Gaussian function. Thus, the pixel position can be determined by the maximum of the Gaussian. A comparison between this position and the known wavelengths of the emission lines makes it possible to fit a polynomial of 5th degree to convert pixel positions into wavelengths. After indicating the first lines by hand the program is able to find more lines automatically. However, it is important to check its results. To improve the calibration accuracy it is crucial to use as many good lines as possible. Good lines distinguish themselves by clear identifiably and thin peaks with a small full width at half maximum (FWHM).

3.2. General reduction process of spectra

As described in the chapter before Bias Frames, Flats and (if available) Darks must be averaged to eliminate statistical outliers at the beginning of the reduction process. After this, the Masterbias is to be subtracted from Science Spectrum, Masterdark and Masterflat. In the next step the Science Spectrum must be corrected for thermal noise by subtraction of the Masterdark from the science spectrum and Masterflat. With the Masterflat normalized to 1 the unequal illumination of the chip can be corrected.
The method of flatfield correction depends on the spectrograph type. For a slit spectrograph the science spectrum frame can be just divided by the Masterflat. In case of a fiber spectrograph the blaze function for every order must be calculated by the envelope of the flatfield orders. Thus, the final corrected frame is calculated by (Weigert et al., 2009):

$$\text{Final frame} = \frac{(\text{Science} - \text{Masterbias}) - (\text{Masterdark} - \text{Masterbias})}{(\text{Masterflat} - \text{Masterbias}) - (\text{Masterdark} - \text{Masterbias})}. \quad (3.1)$$

For observations without darks, this equation simplifies to

$$\text{Final Frame} = \frac{\text{Science} - \text{Masterbias}}{\text{Masterflat} - \text{Masterbias}}. \tag{3.2}$$

To extract the spectrum out of the frames it is essential to know the positions of the orders on the frame. A bright Flat is used to fit polynomial functions to the bright orders. Since the orders are at the same positions on the Flatfield , the Science Spectrum and the ThAr spectrum the same polynomial functions can be used for all three frames.

The next step reads out the pixel values of the science spectrum along the polynomial function for every pixel and creates the flux function $F_n(x)$ depending on the pixel position x and the order number n.The ThAr spectra can be extracted in the same way. With the known wavelengths of the ThAr spectrum it is possible to create a function $\lambda = f(x)$ by comparing the wavelengths of as many emission line as possible with their pixel positions and fitting the function $f(x) = \lambda$ to them. With this function f the flux function $F_n(x)$ can be transferred into a wavelength depending flux function $F_n(\lambda)$ which is the final spectrum. For all n orders, $F_n(\lambda)$ can be merged to one function by merging the overlapping parts of the orders.

3.3. Reduction of CAFE spectra

3.3.1. Reduction process

The analysis of all given data started with the reduction of CAFE spectra. Like described before, CAFE spectra were reduced with *REDUCE*. For CAFE no Dark frames were provided.
After Master Dark and Master Bias were averaged *REDUCE* found orders in a range from around 400 nm to 1000 nm in 82 to 89 orders depending on night and data quality to extract the flux there. For wavelength ranges larger than 700 nm the wavelengths of neighbor orders did not overlap any longer. Thus, gaps in the spectrum for high wavelengths occurred. The results of the ongoing extraction process showed some quality issues. Order edges, especially in the red parts and bluest parts (which got almost no light), had high noise levels due to the fact that the edges of the chip were not well illuminated. The noise was often so high that no lines could

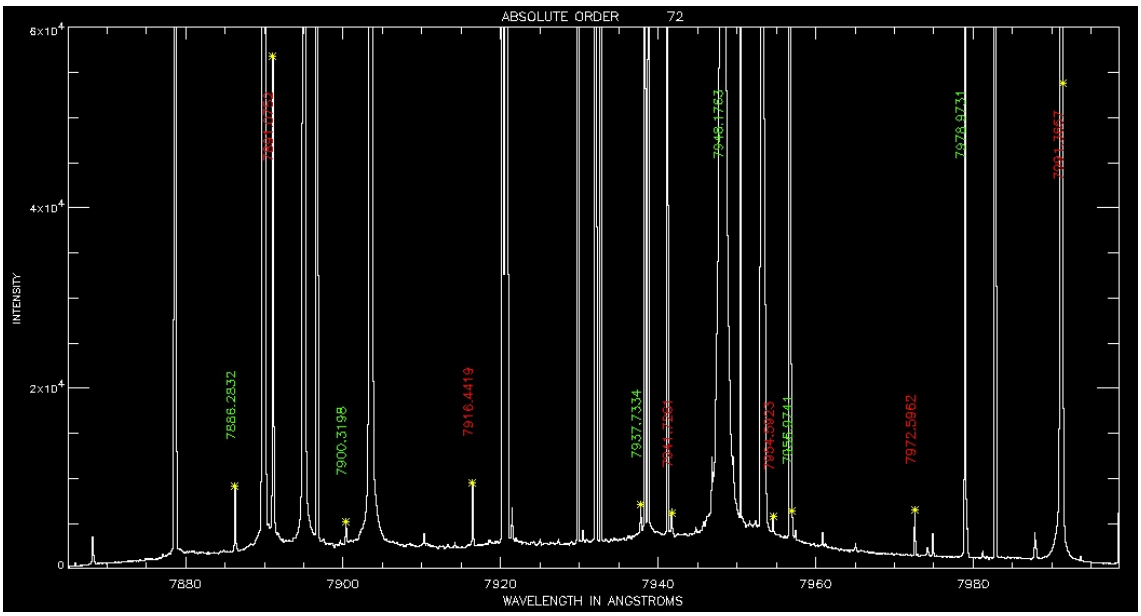

Figure 3.1.: Part of a ThAr emission spectrum around 7900 Å. The emission lines with their known wavelengths can be used to calibrate the wavelengths of a recorded star spectrum because light with the same wavelength is displayed at the same position for the ThAr spectrum and the star spectrum. The very sharp emission lines are necessary to ensure a high radial velocity precision.

be identified. With the errors calculated by *REDUCE*, a filter was installed for every single data point to eliminate data points with a relative error larger than 1. They were removed before the ongoing analysis.

The performing and the results of the extraction procedure of *REDUCE* were not satisfying. It worked very slow and it could not be understood how the error calculation works to estimate the quality of the results. With the new program *Fox* (see section 3.1), the extraction process was repeated. One advantage of *Fox* is its much faster extraction procedure. The time to get the flux from a science frame decreases from two minutes to around 5 seconds without the time needed for eliminating the stray light. In addition, *Fox* give smaller errors for every data point than the old *REDUCE* procedure (see Figure 3.2). Whether this is caused by a better determination routine in *Fox* or an imprecise calculation of *REDUCE* is still unclear because of the incomprehensibility of the error calculation in *REDUCE*.

After the spectrum was extracted a comparison between the right end of one order and the left end of the next showed discrepancies in their flux values. It was expected to find the same values for both orders because the same wavelength range was ob-

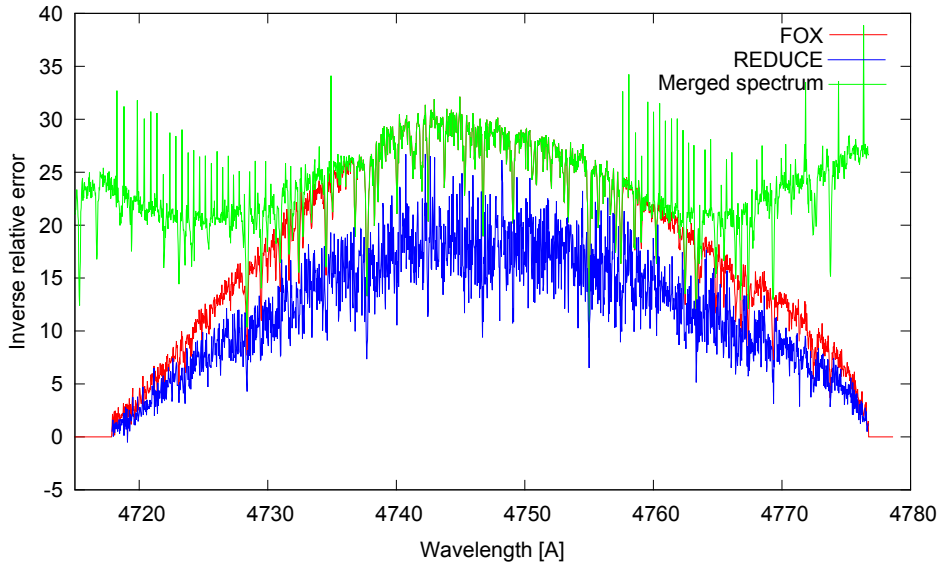

Figure 3.2.: Comparison of the inverse relative error (definded as value/error) calculated with *REDUCE* and *FOX* for one order. Additionally the curve of the merged spectrum is plotted in the same wavelength range. The function for *FOX* is entirely above the *REDUCE* function. Thus, the error bars of *FOX* are smaller. The thin peaks in the merged function are caused by a higher number of data points in the bin.

served. The fact that always the order with the lower wavelengths showed smaller values and the ratio between both order edges were equal over the whole wavelength range led to the assumption that this differences were effected by Charge Transfer Efficiency (see Section 2.2.3). With a CCD size of 2048 Pixels per row a decrease of the flux values seems plausible. A correction with an efficiency of $0,99995$ removed almost all of the discrepancies.
After the extraction process the wavelength calibration was performed with a ThAr spectrum by the procedure *WAVECAL* (see section 3.1).

3.3.2. Problems occured while the reduction

After Masterbias and Masterflat were created *REDUCE* had problems to find orders in the flatfield frames. The flatfield part for long wavelengths got an insufficient amount of light, thus the contrast between order and background was too small. Due to the fact that M dwarfs emit radiation in red and infrared wavelengths the results of this order definition process were unfeasible. *REDUCE* extracts flux values only from parts where it have found orders. It was necessary to manipulate a flatfield to

create a new order definition file with a higher contrast.
The smallest pixel value between two infrared orders which was necessary for the analysis was searched and all pixel values with a flux lower than this were set to 10 to decrease the background. If pixels were set to a value lower than 10, errors occurred were the program set these pixels to the highest possible number. In the next step rectangular areas with similar brightness were defined and their background was decreased, depending on the lowest pixel value in the orders of the specific areas.
During the calibration of the first observation night a missing order came apparent, which was not measured in the order definition process. This missing order generated a gap of around 100 *nm* in the infrared regime and therewith a large loss of information.
During the order definition manipulation two small squares between two orders appeared because of unknown reasons. Both orders seemed to be connected and *REDUCE* interpreted them as one. Thus, the second order was skipped. Figure 3.3 shows a part of an order definition file with both squares. Additionally, rectangular areas from the manipulation process can be seen. A changed threshold for decreasing the background solved the problem and eliminated the squares.

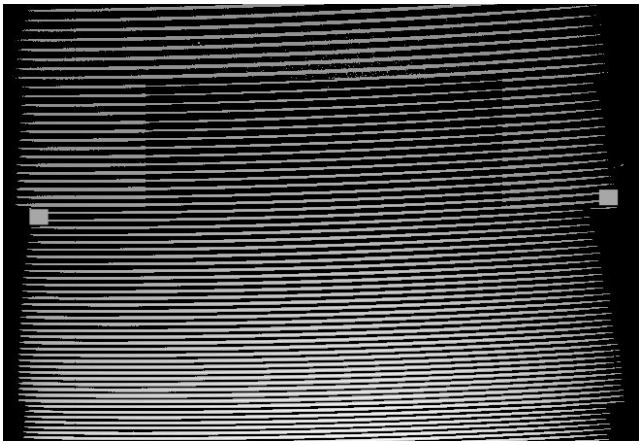

Figure 3.3.: Incorrect order definition file. Both squares connect two orders and lead to a skip of one order in the order definition process.

A big, bright spot appeared for some nights from March to May 2013 in the ongoing analysis process on all frames: Science Spectrum, Flatfield and ThAr. The illumination in the lower half of the chip was very high and washed-out and could not be caused by normal star light. For bright reference stars and flat field frames the spot was much stronger than for observations of M dwarfs. A request at the

observatory gave the information that a leak in the vacuum affected condensations on the camera head. It was not possible to fix this problems before May 2013. Thus, condensed water could form and contaminated the observations for some nights, but not for all. The spectra from the following nights in 2013 were unusable: 30th March, 31st March, 26th April, 27 th April, 7th May, 9th May, 10th May, 11th May and 12th May.

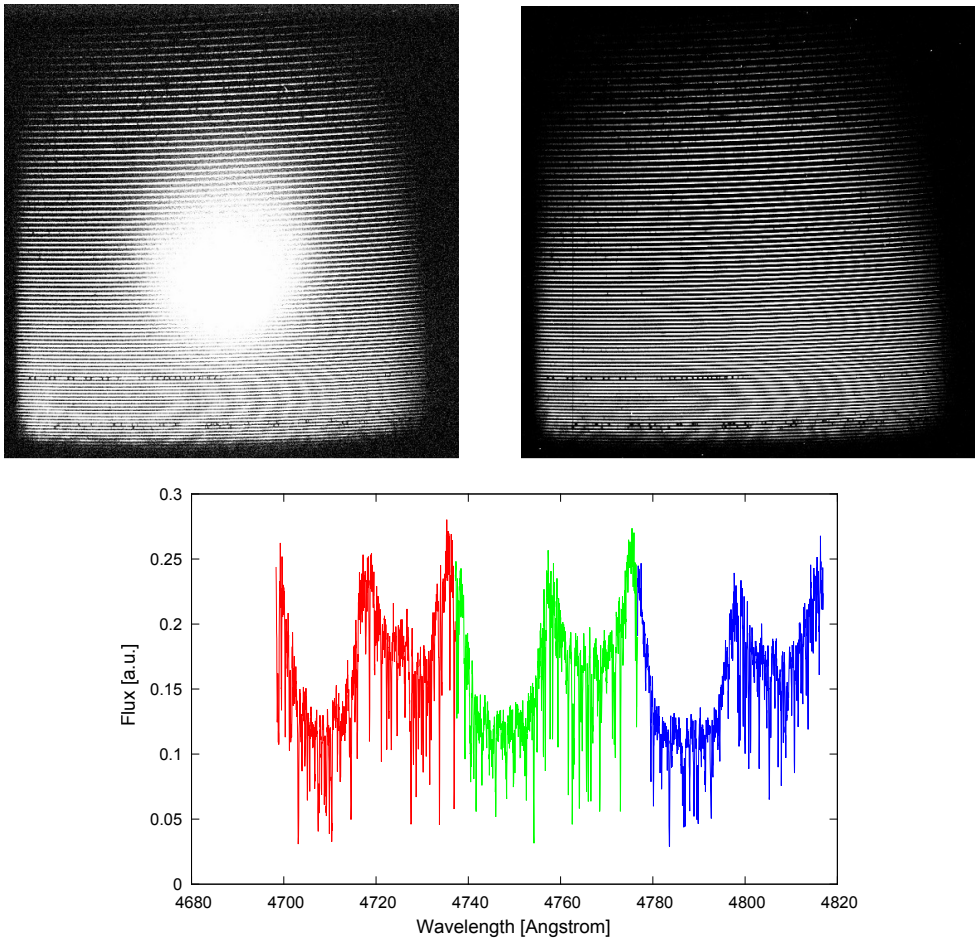

Figure 3.4.: Flatfield with a brigth spot at the center (top left). The spot contaminated the reduced spectrum and produced peaks in every order where the spot lied. The spectrum in the lower image shows these peaks for three orders. Because the spot appeared also at the Science Frame, but was not so distinct there, the flatfield correction produced the dips and the peaks. For comparison a normal flatfield is shown in the upper right image.

Some attempts were made to recover the data. The first one was to remove the spot in the Science frame using the same feature in the Flatfield frame by a normal flatfielding process.
This method eliminated most of the spot but had large problems at the edges. The final spectra showed peaks in each order were the frame was affected. Unfortunately, the size of the spot depended on the brightness of the light source. Therefore, the spot on the Flatfields was larger than the one on the Science spectra. The Flatfield values at the edges of the spot were to high leading to too small flux values after the Science Spectrum was divided by the Flatfield. A later correction of the peaks was not possible. The spot and a contaminated spectrum is shown in Figure 3.4
A second attempt was to handle the spot like stray light. With a Fourier transformation for all columns and rows low frequency oscillations should be eliminated. Since spectroscopic lines appears as high frequent oscillations in Fourier space they would not be affected. This very promising method produced not the desired success and the spot remained hardly effected.
As no working method could be found to make the contaminated observations usable, they were not analyzed. An analysis with feasible spectral type results were neither expected nor possible.
The spectra taken from the HRS spectrograph were available in a reduced format. For the reduction process *REDUCE* with *FOX* was used. However, during the normalization process or the flatfielding process an error occurred which was noticed during the analysis of this thesis the first time. For the continuum fit a polynomial with a too high degree was used. In ranges of absorption bands which are important for the spectral typing the polynomial followed the spectrum in the band. Thus, the dip of the absorption band in the spectrum was eliminated by dividing the spectrum by the polynomial. With it the important information of the temperature were lost. Fortunately, the raw extracted spectrum and the calculated Blaze function were saved. Both were used to restore the spectra.

3.4. Automatic spectroscopic analysis

3.4.1. Normalization

The first step of the analysis is to normalize each spectrum. For every observation night additional spectra taken from brighter reference stars (e.g. G-types or early

K-types) were taken. These spectra show a much more clear continuum than the M-dwarf spectra and contain the same illumination effects. Normalizing the M-dwarf spectra by using a polynomial fit to their spectra was not possible because M-dwarfs show no real continuum. A very high polynomial order was necessary to follow the spectrum. However, a polynomial of such a high order followed also the absorption bands which are used to determine the spectral type and destroyed the information on the effective temperature like it was the case for the HRS spectra. It was possible to divide the M-dwarf spectra by the continuum of the reference spectra to eliminate all remaining effects of the spectrograph.

3.4.2. Determination of radial velocity, activity indicator and SNR

Radial velocity

Section 2.1.4 describes how a spectrum is red or blue shifted due to the radial velocity of a star towards Earth. For the further analysis steps the spectrum must be corrected. To do this, a part of the spectrum with clear absorption lines must be compared to the same part in a synthetic PHOENIX spectrum (Hauschildt, 1992) showing all lines at their laboratory wavelengths. One of these spectra is shifted by a radial velocity with Equation 2.6 in the range from $-200\ km/s$ to $200\ km/s$ in small steps. For every data point the cross correlation of both spectra was calculated producing a cross correlation function depending on the radial velocity shift. The maximum of this function gives the radial velocity of the star towards Earth. To improve the measurement a Gaussian function can be fitted around the maximum taking the peak of the Gaussian as the radial velocity. This measurement was done for the five different ranges given in Table 3.2 containing many different absorption lines in each spectrum. For some stars, especially fast rotators that are also

Wavelength ranges in Å
$6565 - 6620$
$8200 - 8320$
$8440 - 8470$
$8500 - 8550$
$8620 - 8670$

Table 3.2.: Used wavelength ranges to calculate the radial velocity for non active stars.

magnetically active, the lines from Table 3.2 often gave unusable results with peaks at different radial velocities. This was caused by broad absorption lines leading to broad Gaussian functions in the cross correlation function and the transformation of absorption lines into emission lines for activity affected lines. For these stars the ranges from Table 3.3 were used. They provided results with a lower precision for non active stars than the ranges in Table 3.2. Due to this, the used wavelength ranges were split for active and non-active stars. From all single results an average

Wavelength ranges in Å
$7300 - 7350$
$7676 - 7725$
$8350 - 8400$
$8400 - 8450$
$8500 - 8550$

Table 3.3.: Used wavelength ranges to calculate the radial velocity for fast rotators and active stars.

and its error σ_{RV} was calculated. If one of the single results had a difference to the average larger than $3\sigma_{RV}$ this value was taken out and a new average was calculated. After this all values were checked again whether they are in a 3 σ_{RV} range or not. This procedure was necessary to eliminate wrong measurements when there is another peak in the cross correlation function higher than the right one. After the calculation of the radial velocity all wavelengths were corrected.

Barycentric correction

Due to the rotation of Earth around Sun (or more precisely around the barycenter of the system Sun-Earth) the fraction of the radial velocity affected by this motion is measured automatically during the determination of the redshift and is included in the radial velocity result. With a barycentric correction, the radial velocity of a star relative to the barycenter of the Solar System can be calculated. To do this, the IDL routine *baryvel* was used and Earth's motion in direction to the observed star was determined and subtracted from the measured radial velocity. The accuracy of *baryvel* is given by 42 cm/s (Stumpff, 1980). Thus, the accuracy of the barycentric correction will be much smaller than the accuracy of the calculated radial velocities.

Activity indicator

To find active stars, H_α can be used to calculate an activity indicator. A small theoretical introduction in active stars was given in Section 2.1.5. With Equation 2.11 the luminosity ratio $L_{H\alpha}/L_{bol}$ can be calculated and used as an activity indicator. To get the equivalent width needed for this equation two ranges of the spectrum were used to normalize the spectrum near H_α: one redward and one blueward to H_α. For both the median flux was calculated in the ranges [6545 Å, 6559 Å] and [6567 Å, 6580 Å] based on the ranges given in Reiners & Basri (2008). Afterwards, the equivalent width in the range [6560 Å, 6565 Å] was determined.
Additionally, a χ factor connecting the equivalent width of H_α and the activity indicator (see Equation 2.11) which depends only on temperature is necessary. As the spectral type corresponds to a stars temperature the spectral type can be used to get a temperature sequence of $T = 2475\ K$ for M9 stars to $T = 3900\ K$ for M0 stars (Rajpurohit et al., 2013). With these temperatures and a polynomial of 5th degree adopted from Reiners & Basri (2008) χ can be calculated.

Signal-to-noise ratio

To determine the quality of all spectra, an analysis of the signal-to-noise ratio (SNR) is necessary. Parts of the spectrum without any spectral lines are used to calculate the variability of the signal. For M dwarfs such ranges are very rare, so three small parts were chosen to get around 100 data points. In the ranges [8842 Å, 8843 Å], [8732.75 Å, 8733.5 Å] and [7572 Å, 7573 Å] the average differences to the median and the ratio between both numbers were calculated. Weighted on the number of data points the SNR values of all three ranges were averaged.
The ranges specified above are the only ranges were no spectral lines could be found. Nevertheless, for the CAFE spectrograph one of the three ranges were located in an order gap, for HRS this happened for two of the three ranges. Fortunately, for this spectrographs errors were given for every data point. Around 7572 Å the average of the relative errors (defined as ratio of error and value) for around 100 data points were determined as SNR. The SNR is rounded down to the next decade, respectively the next integer if the SNR is smaller than 10.

3.4.3. Spectral typing

The determination of spectral types is based on calibration data from THE HAMMER (Covey et al., 2001). The developed program was written to analyze the spectral type automatically. It calculates index values for temperature sensitive lines and based on them, the spectral type of a star (see Section 2.3.3). THE HAMMER measured calibration functions for 29 lines over the whole spectral type series. Not every line is sensitive for every spectral type, so lines sensitive for spectral typing of M-dwarfs were selected. Lines with a high scatter of data points in the calibration function in the range of M dwarfs were sorted out. The 11 lines from Table 2.1 were chosen to classify the stars. However, not all of these lines are sensitive for all M-dwarf subtypes. The lines VO7434, VO7912 and TiO5, sensitive for early types, and VO-a, Cs-a and CaII, sensitive for late types, were used to calculate a reference type and with the help of it the spectrum was categorized in one of three groups: Early types (earlier than M4), Mid types (M4 to M6) and Late types (later than M6). These lines were chosen to calculate the reference type because they are bijective in the investigated ranges. Based on the reference group different lines were used to calculate the spectral type. In Table 3.4 the selected lines for all groups are listed.

Early types	Mid types	Late types
CaI 6162		
CaH3		
CaII 8662*	CaII 8662*	
TiO5	TiO5	
VO 7912	VO 7912	
VO 7434*	VO7434*	
	Cs-a	
	TiOB	TiOB
	TiO 8440	TiO 8840
	VO-b	VO-b
		VO-a

Table 3.4.: Used Lines to get the spectral type for each group. Most lines are used in more than one group. Lines with bad results and/or activity dependence were canceled later. They are marked by *.

After the calculation of the reference type, the program uses all lines of one group to get every possible spectral type from their calibration functions. Because not every calibration function is bijective in the investigated range more than one

spectral type with the same index value is possible for one line. In this case the closest result to the reference type was taken as the result of this line.
Data points of the calibration function were only available for every subtype, thus the result of every line was determined as a half subtype between the earlier and the later subtype (i.e., if the index value is between M3 and M4 the result is determined as M3.5).
It can happen that the program cannot find any spectral type matching to the calculated index value. In this case the line was not used. After a single result for every possible line of the group was calculated, all results were averaged to the final spectral type of the specific spectrum. The error is calculated as the error taken from the average calculation and an additional systematic error of 0.5 subclasses. This was chosen because the calibration functions resolution is of only 1 subtype. Figure 3.5 shows the process described before in a sketch.

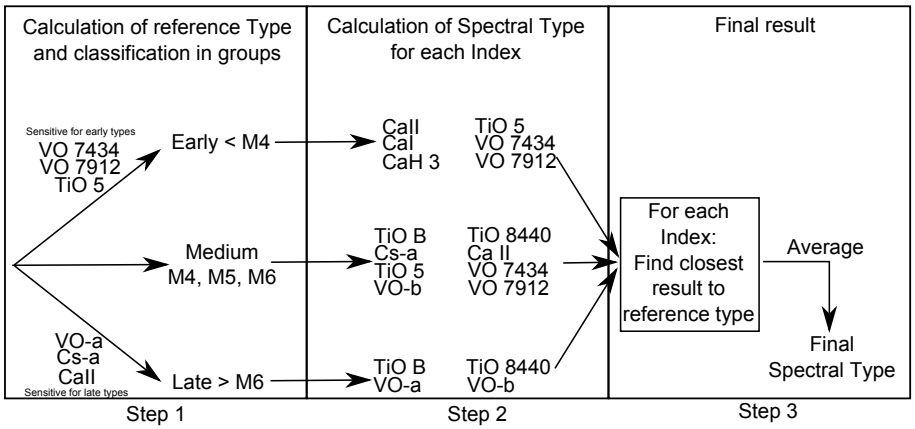

Figure 3.5.: Sketch of the used spectral typing process.

4. Results

4.1. Analysis of spectra

After the rejection of unusable spectra and probably false observations (see section 4.2), 842 spectra remained to investigate 364 stars. All spectra taken from the same star were averaged to remove outliers. Table A.2 in the appendix gives an overview of all these stars. If there was only one spectrum of a star available the values of the spectral type, radial velocity and activity indicator of this spectra were used with their calculated errors. For multiple measurements the weighted average of all spectra were calculated. The error of the activity indicator is the error of the average from all spectra. Thus, there is only an error for multiple measured stars. Some stars were observed with different spectrographs. They are marked with 'MULTI' in the spectrograph column.

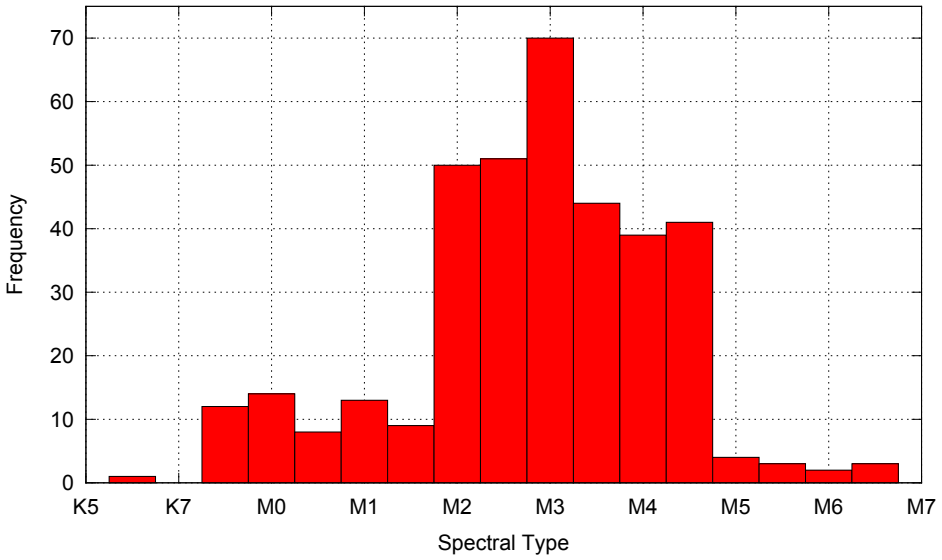

Figure 4.1.: Histogram of all calculated spectral types.

4.1.1. Spectral types

Figure 4.1 shows the statistical distribution of spectral types from the investigated sample. 81% of all stars have a spectral type between M2 and M4.5. Only 16% show a spectral type earlier than M2 and just 3% one later than M4.5. However, this distribution is caused by a selection bias from the input catalog.
It is planned to observe 100 M0 to M2 stars, 100 M3 to M4 stars and 100 stars later than M4 with CARMENES (Quirrenbach et al., 2012). The distribution of Figure 4.1 does not confirm this very well. Half of all stars from the group of early type stars would be of type M2 and in the here used sample are almost no stars with spectral types later than M4.5

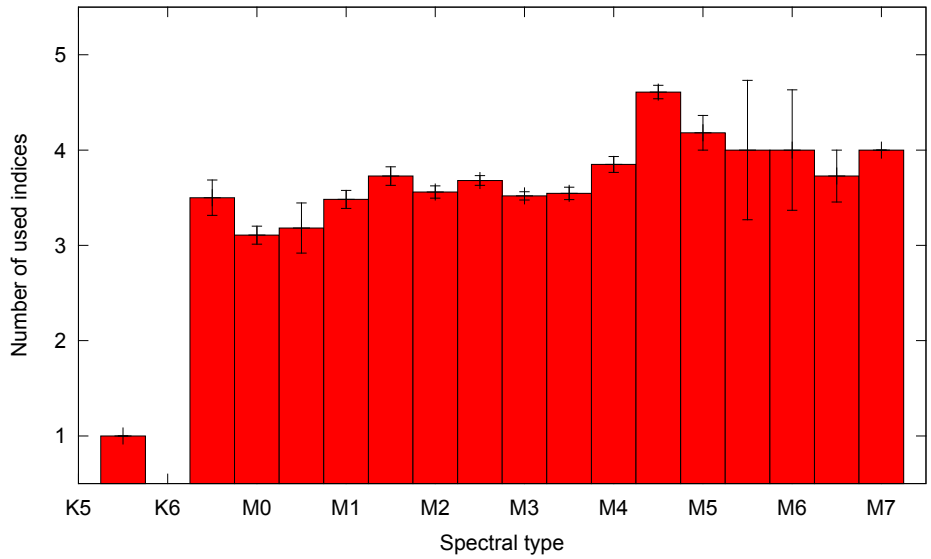

Figure 4.2.: Average number of used indices for each spectral type. Note: This plot is based on the results of each spectrum and not on the average of each star.

To get an idea of the quality of the spectral type determination Figure 4.2 shows a histogram of the average number of used index values for each spectral type. The error bars give an estimation of the variation.
The average number of used lines varies between 3 and 4.5 lines. A small increase from early types to late types can be seen. For types around M0 were only 3 to 3.5 lines usable. For types around M5 this number increases to 4 or higher. This may be caused by the use of different groups and therewith different lines in the analysis algorithm. For both groups, early and medium types (there are almost no spectra in the late type group), four lines gave very well results, but it seems that for the

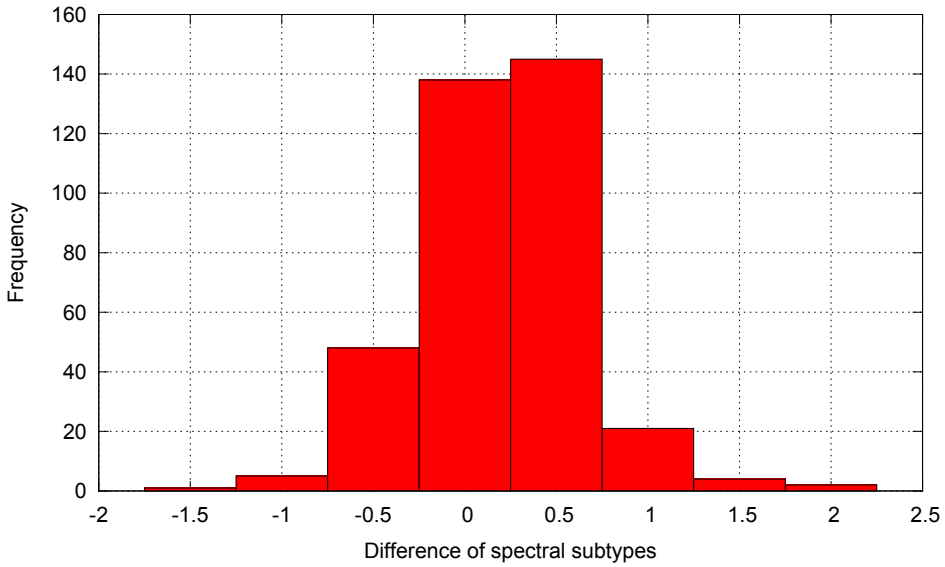

Figure 4.3.: Comparison of calculated spectral type with the literature values from CARMENCITA. The histogram shows the frequency of all differences. Positive values mean the literature value is a later type.

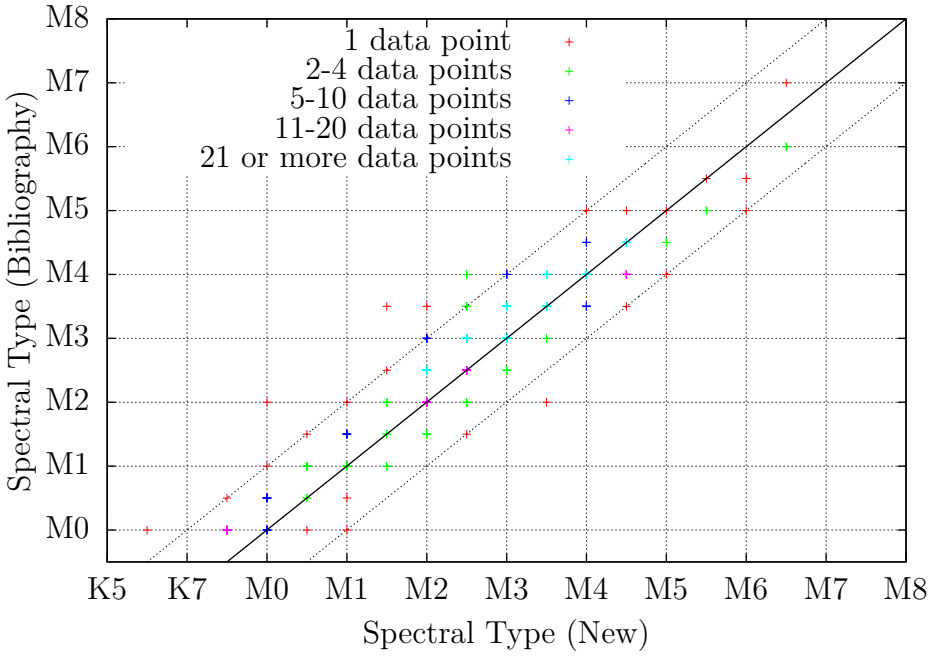

Figure 4.4.: Comparison of the calculated spectral type and the literature values from another point of view. Both types are plotted versus each other with a comparative straight line. The dashed lines symbolizes a range ±1 subtype. Most of all stars are in this range. The different colors symbolize how many stars lie at the same data point.

medium type group more lines in average were usable.
The error bars of the histogram increase a lot for type M5.5 or later. Here, the number of available spectra was very low and the variation was even high.
There is a single spectrum taken from J09231+223 with spectral type K5.5 where only one index value was usable. It was planned that the analysis program is able to determine spectral types especially in class M but also in class K to around K4-K5. Why the results of this spectrum are that bad is unknown. However, it is a single data point and maybe an outlier.

Figure 4.3 gives a comparison of all calculated spectral types and the literature values from CARMENCITA. It is easy to see that 91% of all stars are in a range of ±0.5 subtypes compared to CARMENCITA. However, a preference to positive differences can be seen. It is probable that this is also a selection bias. Figure 4.6 shows the same plot as Figure 4.3 for every single subtype (some subtypes with a very low number of measurements were summarized to increase the statistical significance).

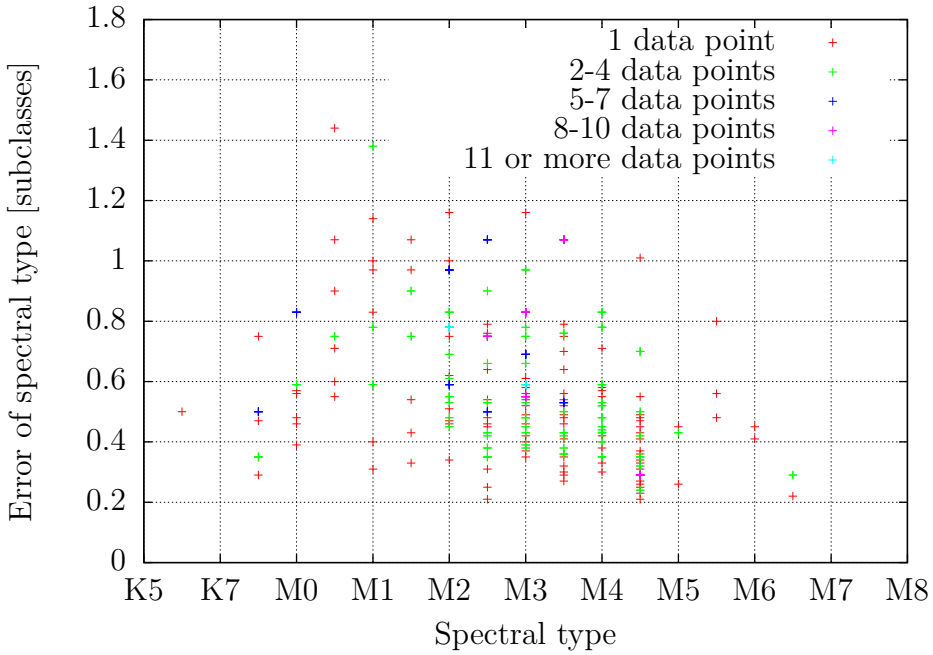

Figure 4.5.: Calculated errors for every star depending on the spectral type. Most spectral types are determined with an accuracy of 1.2 subtypes or less. These results correspond to the comparison of spectral types from this thesis and the ones from CARMENCITA in Figure 4.4.

The histograms for early types show a clear peak at +0.5 subtypes. The later the spectral type the more wanders the shift to a value of -0.5 subtypes. Only for M2.5 a small trend back to +0.5 can be detected. If this is caused by a too small number of used measurements can not be decided. Due to the effect that most stars are in range M2 to M4.5, the overview of Figure 4.3 gets an overweight at a difference of +0.5 subtypes. Only class M4.5 (and M4.0 a little bit) got more differences -0.5 than +0.5. This is overcompensated by the other spectral types in Figure 4.3. Figure 4.4 compares the calculated spectral types with the CARMENCITA literature values from another point of view. Both values are plotted versus each other. The spectral types follow the expected solid line, while the dashed line shows a range of ± 1 subtype containing almost all stars.

The calculated errors as a function of the spectral type are displayed in Figure 4.5. Despite of the two data points at an error of around 1.4 subclasses all determinations are more accurate than 1.2 subclasses. In average the error is 0.6 subclasses which is an excellent result because an systematic error of 0.5 subclasses was added to the statistical error for every spectrum. The error for a single star can be smaller than 0.5 subclasses if there was more than one spectrum measured for a star.
It seems that the average error decreases with later types but again, the number of data points of the latest and earliest types is too small to provide statistically significant results.

4.1.2. Radial Velocity

To analyze the radial velocity distribution of the sample, Figure 4.7 shows binned radial velocities of all stars. The distribution resembles a Gaussian function with a peak around 0 km/s. However, the data set is to small to verify a real Gaussian distribution. Some outliers, e.g. the bars at -25 km/s and 15 km/s, causes doubts which could be eliminated by a bigger sample.
Most observed stars show only small velocities relative to the sun. This indicates that most observed stars are close to the sun. The velocities of star and Sun are mainly determined by their rotation around the galactic center. Thus, the closer two stars the smaller are the velocity differences despite of some quasi-randomly peculiar motions (Weigert et al., 2009). The high number of close observed stars seems logical because faint stars like M-dwarfs are easier to observe if they are close to Earth. The radial velocity values agree with the ones given in Weigert et al.

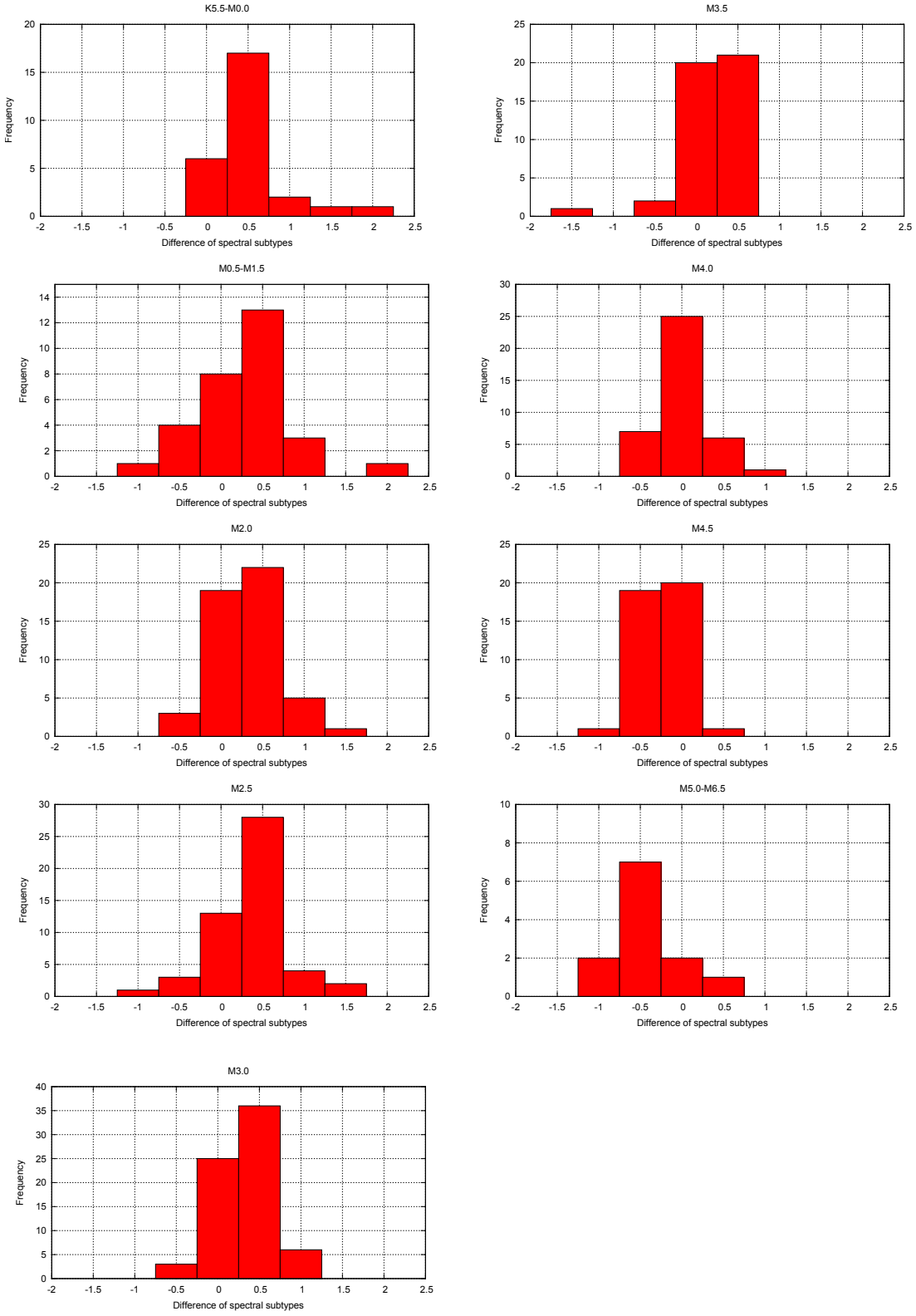

Figure 4.6.: Comparison of the calculated spectral types and the CARMENCITA literature values for every subtype. Some subtypes were summarized to increase the statistical significance. The images are plotted from top to bottom to highlight the shift of the peak to negative values.

(2009) for stars in the neighborhood of the sun. 81% of all observed stars have radial velocities in a range from $-35\ km/s$ to $35\ km/s$.

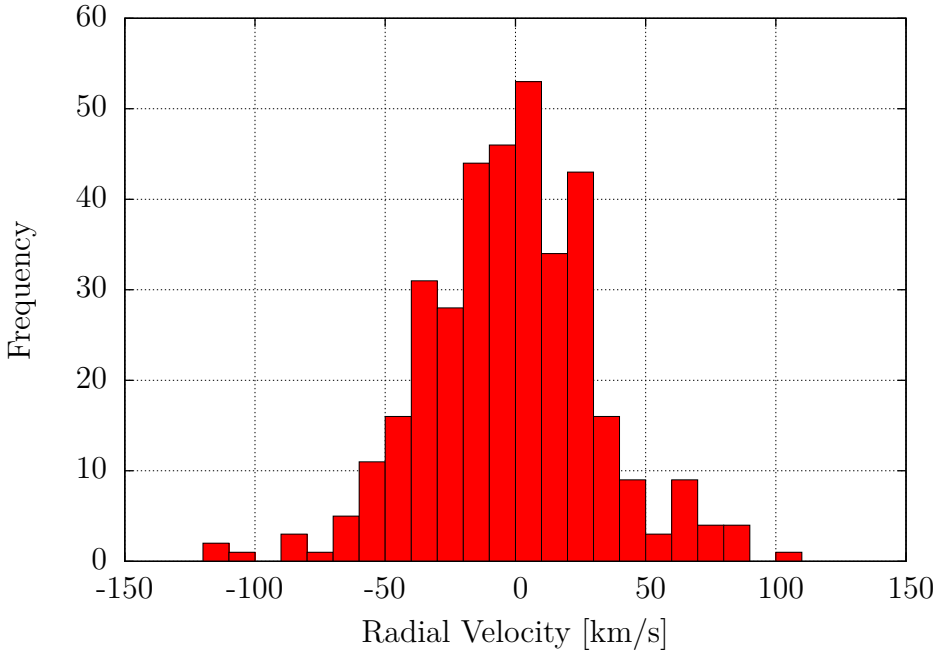

Figure 4.7.: Histogram of the radial velocity distribution.

Figure 4.8 shows the calculated radial velocity versus the given literature values from CARMENCITA to compare both. A straight one-to-one line is plotted, too. Most data points lie very close to this line. Outliers can be found equally distributed on both sides. Hence, there is no systematic error to be expected. Some data points show high deviations to the literature values. Most of these stars are very active stars. Due to the fact that active stars are often fast rotators showing very broad absorption lines and the spectrum contains emission lines, e.g. H_α or Ca-lines, the determination of the radial velocity of active stars is more complicated than the determination for non-active stars. It is hard to say if the high deviations are caused by problems with the determination of active stars in this thesis or in former investigations. It is also possible that a narrow companion with a similar spectral type instead of the target star was observed like described later. It is very reasonable that in such a case a different radial velocity is measured.

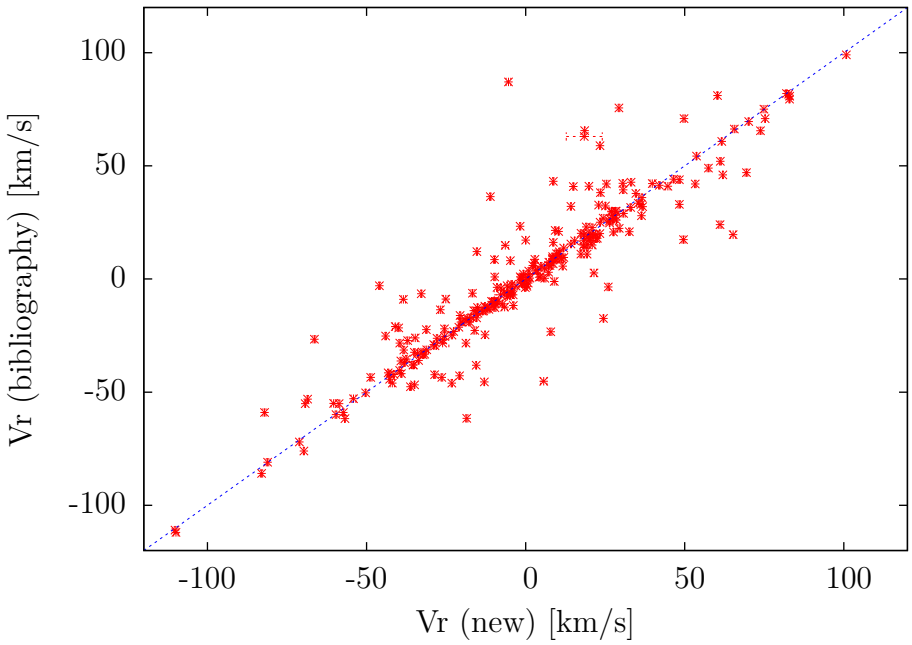

Figure 4.8.: Comparison of calculated radial velocities and literature values from CARMENCITA. Additionally a comparative straight line is drawn to show the expected distribution.

4.1.3. Activity

Most stars, i.e., 73% do not show an emission feature at H_α. Because only the emission of H_α was investigated no conclusions of the strength of H_α absorption can given. For CARMENES it is important to sort out all very active stars with a high H_α emission. Active stars can pretend an oscillating radial velocity shift which could be thought to be created by a planet, although there is no real planet like described in section 2.1.5. Figure 4.9 shows the frequency of the activity indicator A (see equation 2.11) with emission features and the much higher number without emission features (left bar). It is to see that the number of active stars increases with higher activity until $A \approx -2.75$. After this, the frequency decreases until the highest found activity indicator of $A = -1.57$.

4.1.4. Data quality and comparison of different measurements

To quantify the quality of each spectrum the signal-to-noise ratio (SNR) can be determined (see section 3.4.2). Figure 4.10 displays the connection between spectral type and SNR for each spectrum. The SNR values were rounded to their lower

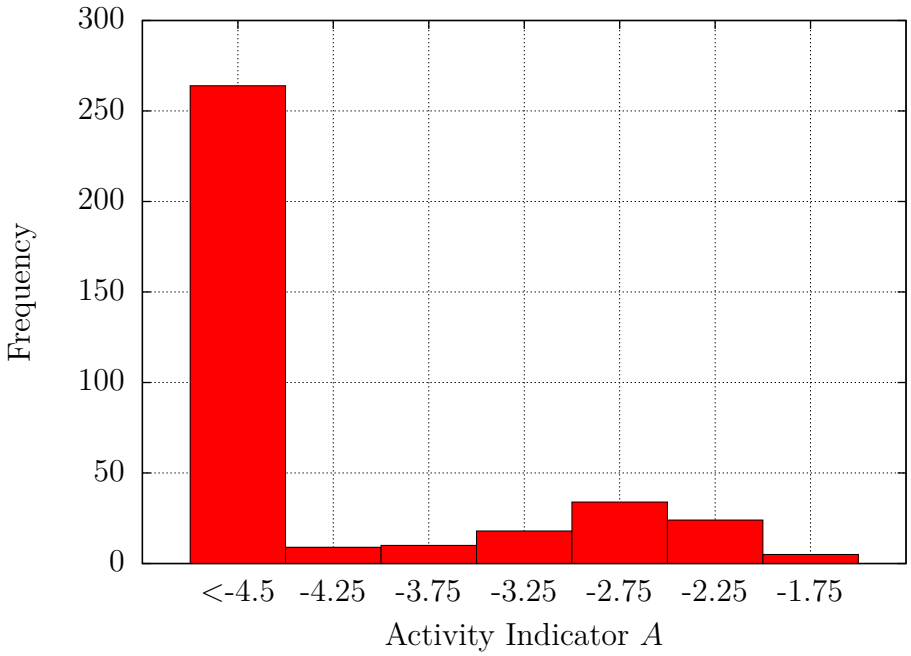

Figure 4.9.: Distribution of the activity indicator A of the H_α line. Most stars do not show a H_α emission.

decade, so only specific data points are possible. The color code in Figure 4.10 shows how many spectra are combined at every data point. A clear decrease of the SNR to later spectral types can be detected which is expected because M dwarfs become fainter for later spectral types. The spectrum of J09231+223 with type K5.5 shows a very low SNR for its spectral type. This matches with the single spectral type measurement and indicates that the results for this star are not sufficient. Other stars with a similar small SNR may be distant stars.

The error bars of the radial velocity measurements were determined by the average error of all single determinations. As mentioned before the accuracy of the radial velocity determinations decreases for fast rotating stars and therefor with activity. It is even expected that the radial velocity accuracy decreases with the SNR. The effect that the amount of active stars increases with later types of class M and the SNR of these stars is lower in average lead to the assumption that the error bars of the radial velocity calculations would increase with later spectral types. In Figure 4.11 both spectral type and error bars of radial velocity measurements are plotted. Despite of some single data points at early types a clear trend of an increasing upper limit of the radial velocity error can be found. Again, there are not enough data points with spectral types later than M4.5 to provide significant results in this range.

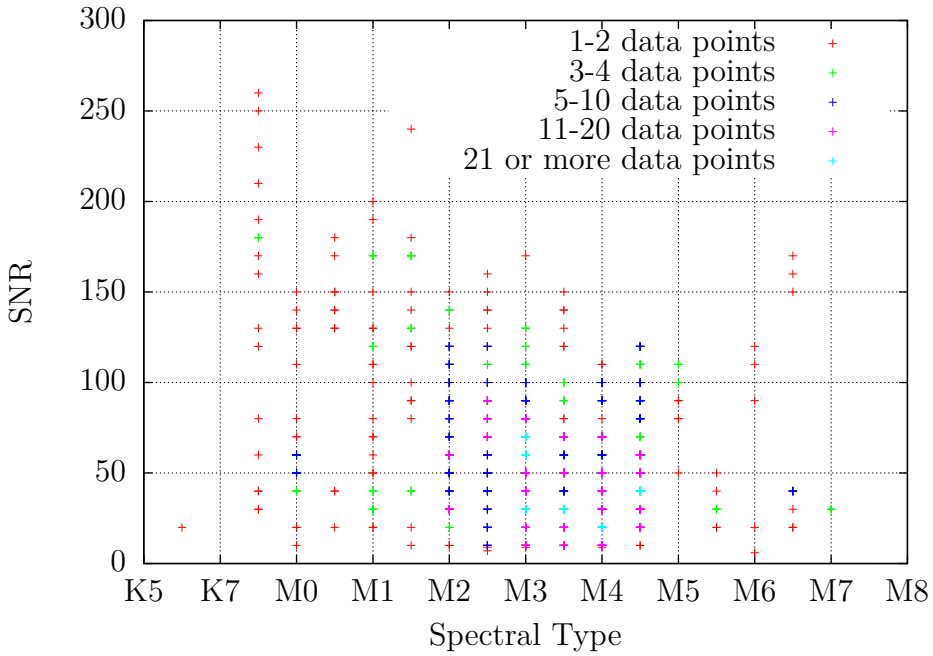

Figure 4.10.: The signal-to-noise ratio decreases for later spectral types. The upper limit of the SNR shows approximately a linear connection to the spectral type. Lower SNR values may be caused by the distant to the stars. Note: This plot is based on the results of each spectrum and not on the average of each star.

The lower limit seems not to be influenced what strengthens the assumption that the radial velocity error is influenced by the activity. The stars at the lower limit are the non-active stars.

The activity indicator A was filtered for all values lower than $A = -4.5$ because for this value the change from a absorption line to a emission line was found (see section 4.3). In Figure 4.12 all data points with a positive equivalent width are displayed also if they have values of A lower than -4.5. Spectra with a negative equivalent width can not be plotted because A is not defined. For the spectral types M2 to M4.5 a gap around $A = -4.5$ can be detected. However, this gap stays not at the same value for every spectral type. It fluctuates between $A = -4$ and $A = -5$. For other spectral types this gap cannot be found, probably because there are too few data points. Maybe the gap shows the change from emission to absorption line of H_α. This would confirm the former assumption that this change happens at $A \approx -4.5$. However, it is an open issue why the position of the gap changes with the

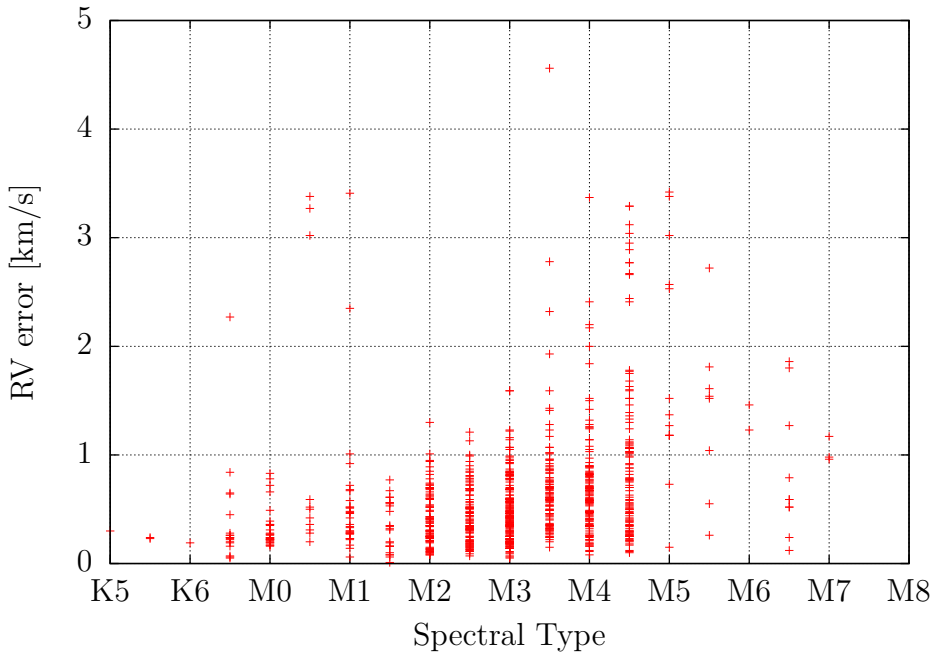

Figure 4.11.: The upper limit of the error of the radial velocity increases for later spectral types. For early subtypes some datapoints do not follow this relation. The lower limit seems no to be influenced by the spectral type. Note: This plot is based on the results of each spectrum and not on the average of each star.

spectral type. There are two possible explanations: First, there is an physical effect which forms the spectrum around H_α in a way producing this shift of the gap. Or, second, the assumptions of the temperature to calculate A (see equation 2.11) based on the spectral types from Rajpurohit et al. (2013) are not sufficiently precise.
West et al. (2004) showed that the fraction of active stars increases rapidly for spectral types from M4 to M8. Earlier types have only a low fraction of active stars and for stars later than M8 the number of active stars decreases again. Figure 4.12 give hints to this connection but it is not significant. One have to keep in mind that all stars with a clear H_α absorption line are not displayed.

4.2. Issues and rejected spectra

Not all spectra could be used for the analysis. Five spectra had a very low SNR around 1, and it was not possible to get any information from them. Additionally, two HRS spectra were provided with a wrong Blaze function which did not match

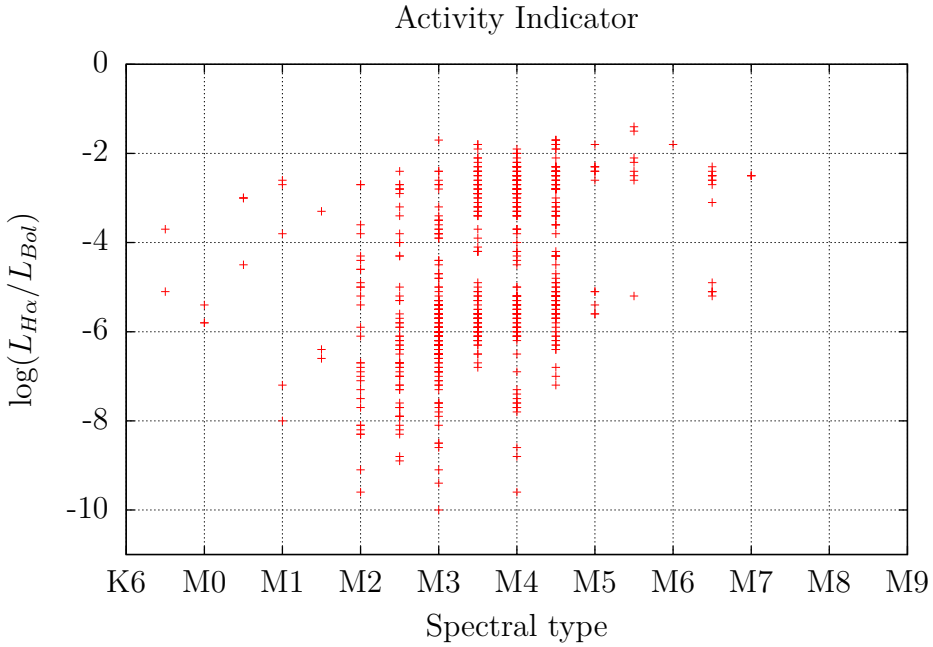

Figure 4.12.: The Activity indicator A depending on the spectral type. A clear gap around $A = -4.5$ can be noticed. Note: This plot is based on the results of each spectrum and not on the average of each star.

to the flux values, making the spectra unusable. However, the third spectrum taken in this night from the same star could be used. All in all, the seven spectra listed in Table 4.1 were rejected.

Date	Time	Star	Spectrograph
20140110	01:18:59	J06171+751	CAFE
20140111	01:27:52	J08005+258	CAFE
20140116	02:06:57	J07119+773	CAFE
20140221	02:17:02	J09561+627	CAFE
20140312	03:26:33	J13536+776	CAFE
20111122	11:04:31	J09218-023	HRS
20111122	11:15:00	J09218-023	HRS

Table 4.1.: List of rejected spectra because their data were not usable. The listed CAFE spectra showed a very low SNR and could not be analyzed. For the HRS spectra an unfeasible Blaze function was provided.

Furthermore 51 spectra could be analyzed but must be rejected because of different reasons. They are listed in the appendix in table A.1. The given error codes of this table are described in the following.

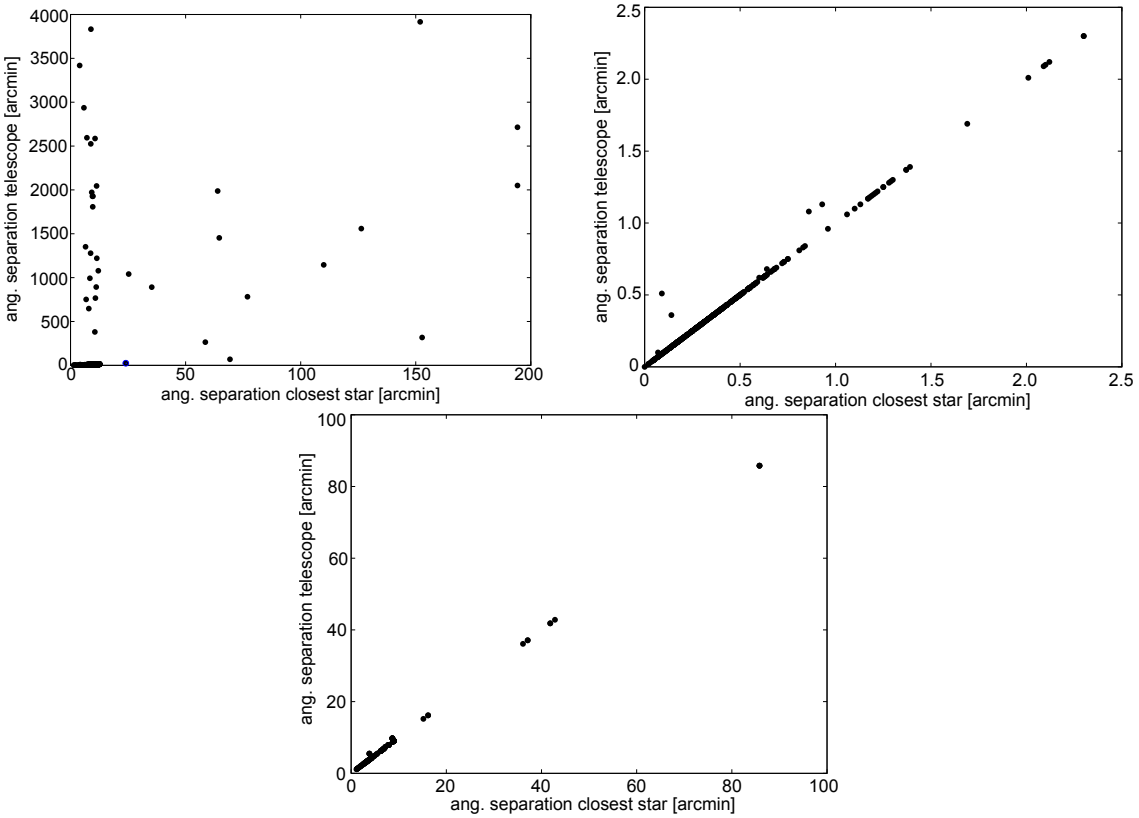

Figure 4.13.: Separation of telescope coordinates to closest star on the x-axis versus the separation to the header star on the y-axis. Rejected spectra are plotted here with the non-rejected ones. For CAFE (top left) extremely high discrepancies can be found. Matching stars are on the small line at the bottom left corner. FEROS (top right) and HRS (bottom) spectra lie almost on or close to the expected line where both values are the same.

First, for some stars a wrong star name was written into the header of their spectrum files. The name of all stars used for CARMENES is build by their coordinates. The right ascension in hours in format HH:MM.m and the declination in degree as ±DD.d gives the name as JHHMMm±DDd. If the name did not match to the coordinates a cross match with the CARMENCITA database was done to find the closest star to the coordinates where the telescope was pointed to. Figure 4.13 shows a comparison of the angular separation between the telescope coordinates and the expected coordinates from the header name on the one hand and the angular separation between the telescope coordinates and the closest star in CARMENCITA on the other hand. For CAFE extremely high discrepancies occurred while for FEROS

and HRS in most cases the header coordinates and the closest star matched. It is very probably that for CAFE wrong star names were written into the files and wrong stars observed. All of the wrong observation must be excluded from the analysis. It is possible that not all wrong observations were found.
However, to be sure that the right star was found the results for this star were compared to other spectra taken from the same star where it is clear that the right star was observed. If the radial velocity was not almost the same the spectra were rejected. In Table A.1 this spectra are marked by an error code '1'.
Additionally, there are stars where the difference between the expected spectral type and the calculated one is very high. In most cases a spectral type in class K was calculated and a short view on the spectrum showed that the spectrum cannot be taken from a class M star in any case. The calculated K type does not need to be right because the used program is not able to calculate spectral types earlier than K4. Earlier stars than this may give the same index values like in the K range for one or two lines. Hence, this spectral types are not confident and it is very probably that a wrong star was observed, e.g., a close companion. In table A.1 this spectra are marked by error code '2'. For some stars no spectral type could be calculated. For them it is very probably that a early type companion was observed, too. They are marked by error code '3'.
The fourth class of error codes contains all other measurements where the results do not match to results from other spectra from the same star.

4.3. Analysis of determination procedure

The first 250 spectra taken with CAFE and FEROS were used to test the analysis algorithm. For all of them a spectral type for all lines was calculated by Equation 2.12, respectively Equation 2.13, after the normalization process.
A comparison to the CARMENCITA spectral types gives the opportunity to investigate the quality of every line index. Figure 4.14 shows histograms of the difference between the measured spectral types and the literature values from CARMENCITA for seven lines. The remaining four lines delivered results only for a few spectra. Their calculated index value matched in most cases to no spectral type. The histograms of them would not be statistical significant, hence they are not shown here. Additionally a Gaussian function is fitted to the histograms. The peaks of the Gaus-

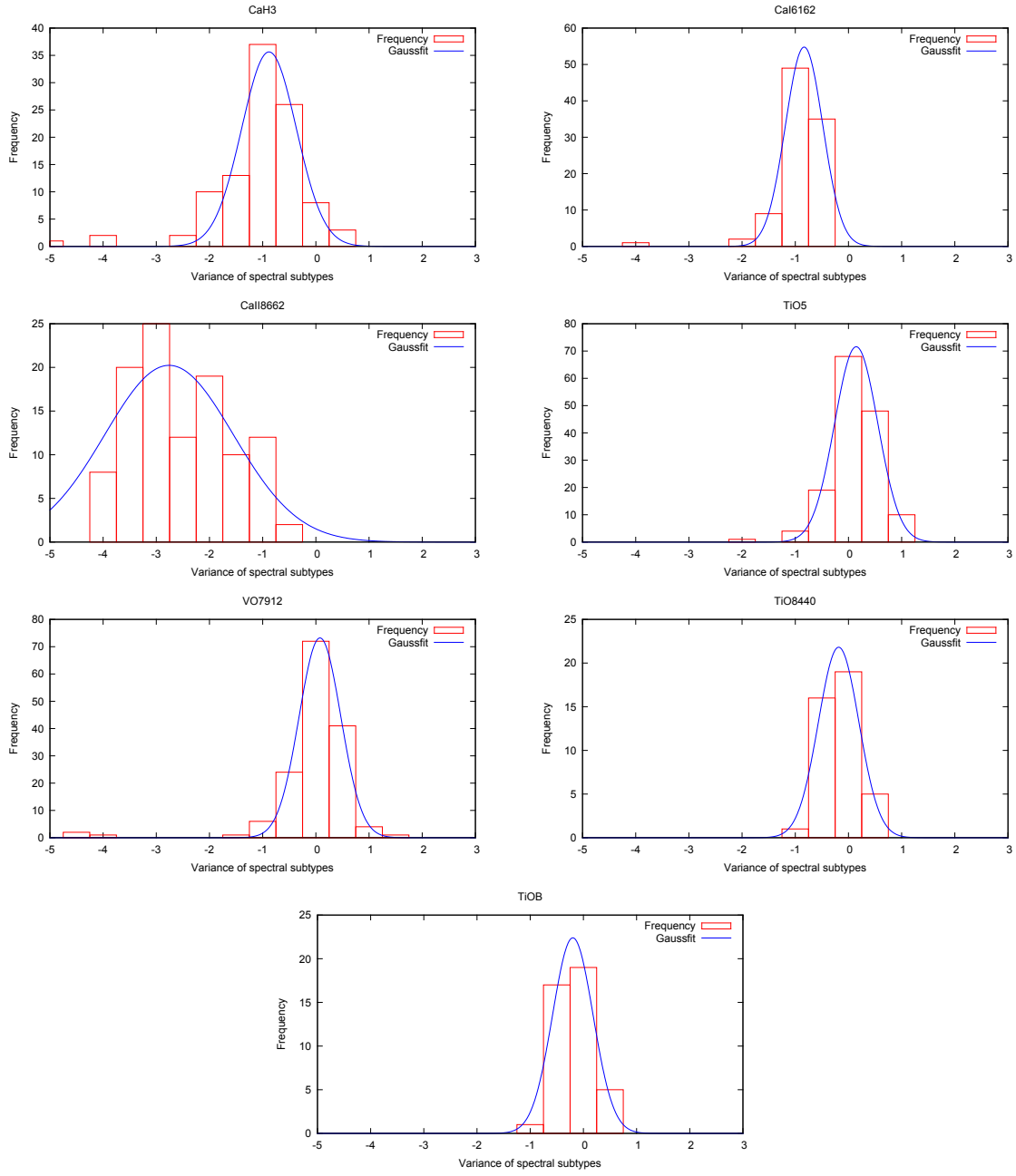

Figure 4.14.: Histograms to compare the calculated spectral types to the ones given in CARMENCITA. A Gaussian function is fitted to the histograms to get its width and shift as quality indicators.

sians give an approximation of the average shift for every index and their widths an approximation of the accuracy. It is easy to see that five of the seven lines delivers very good results with an accuracy of less than 0.5 subtypes. CaH3 shows larger variations but is still used for further analysis runs. CaII8662 displays a very high

shift and the histogram does not fit to the Gaussian very well. It shows a high variability of the spectral type deviations. It is assumed that this is caused by the influence of activity because the strength of the CaII8662 line depends on it. For active stars the CaII8662 line is not as deep as for non active stars. Thus, the index value decreases and lead to a earlier spectral type. Due to this, CaII8662 was not used for the ongoing analysis. All analysis runs were repeated without CaII8662.
Additionally, Figure 4.14 shows that most of the used lines lead to spectral types a little bit earlier than literature results from CARMENCITA. Only the Gaussians of CaH3 and VO7912 have their peaks at positive shifts, but at very small values.
In almost all histograms results with a spectral type in the early range of the K class can be found (small bars on the left hand side of the fitted range). These are expected to be observations of wrong stars. If the right star has a narrow companion, this one may be observed and could have an earlier spectral type. However, the used program is not able to find spectral types earlier than K4. Stars with an earlier spectral type will lead to a result of K4 or to no result.

In section 2.1.5 the analysis of the activity indicator A was described. It was expected to get a positive equivalent width only for H_α emission lines (note the not-common definition of the equivalent width). However, even for small absorption lines the equivalent width of the investigated range was positive. Figure 4.15 shows in the upper part a very weak H_α line, but a absorption line. Due to the normalization process and the absence of a continuum in M-dwarf spectra the spectrum fluctuates around 1 in the ambient range of H_α. The areas above $F = 1$ in the investigated range from 6560 Å to 6565 Å are larger than the ones below $F = 1$ including H_α. Thus, H_α gets a positive equivalent width although H_α is an absorption line.
The lower part of Figure 4.15 shows the H_α line of one of the most active stars in the sample. One can see that H_α becomes very broad for such stars, hence the range for calculating the equivalent width cannot be chosen smaller.
To distinguish between 'real' H_α emission lines and such lines were H_α is an absorption line with a positive equivalent width, spectra with weak H_α lines were investigated to find a threshold of A where H_α changes from a absorption to a emission line. The median value of spectra with weak H_α lines was $A \approx -4.5$. All spectra with a lower activity indicator were not taken as active stars.

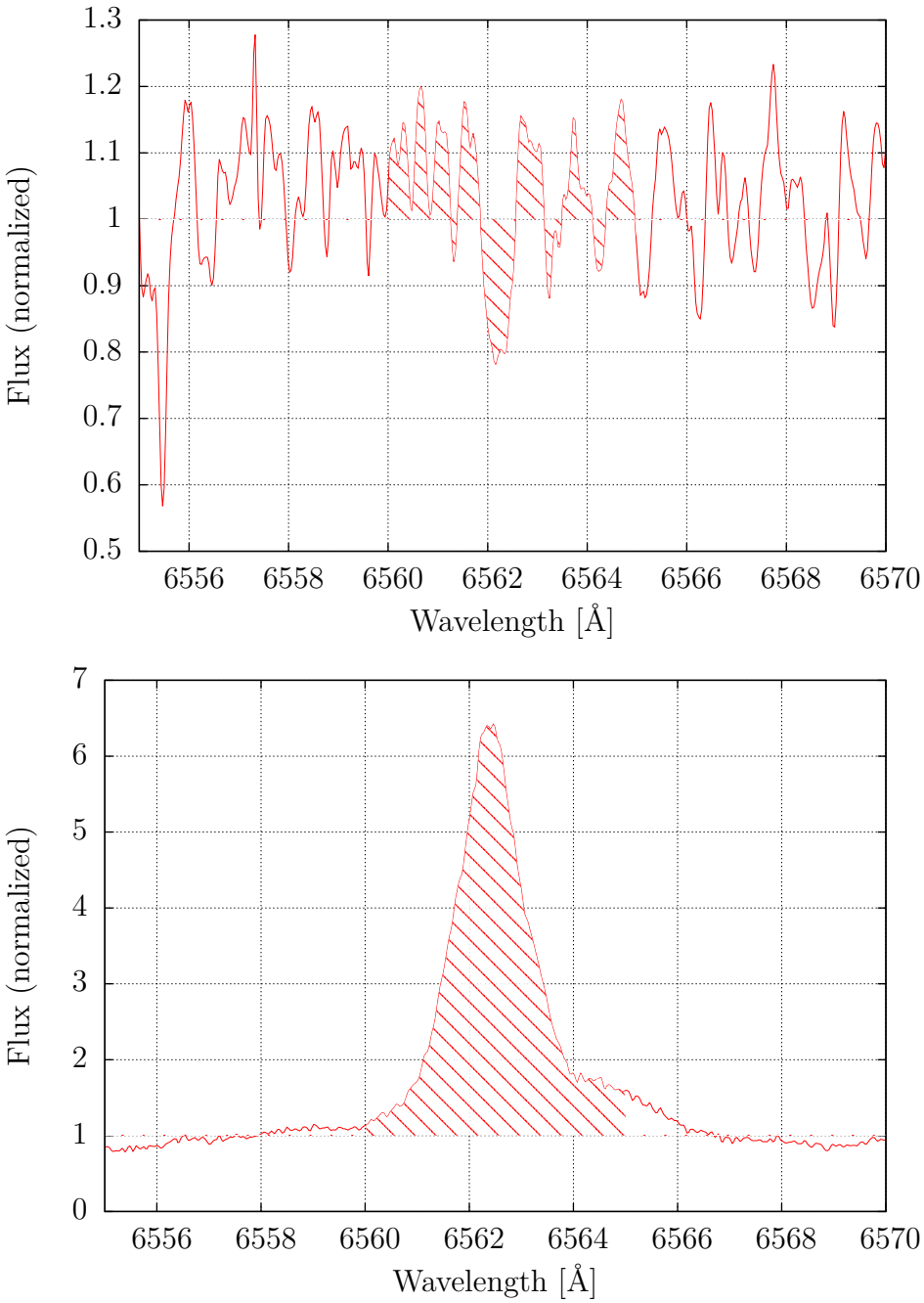

Figure 4.15.: H_α line of two stars with different activity. Both spectra are normalized and radial velocity corrected. The areas to calculate the equivalent width are marked in both figures. **Upper figure:** Spectra of J03217-066 with a weak H_α line. The parts of the spectra above 1 gives a area bigger than the areas bellow 1 (which were subtracted from the upper areas). Thus, the equivalent width is larger than zero, although H_α is a absorption line. **Lower figure:** Spectra of J04173+088, a very active star. H_α is very broad and the whole spectrum in the investigated spectrum range is larger than 1. Due to the high width of the line it was not possible to choose a smaller wavelength range.

5. Discussion

Most of all determined spectral types are in a range ±1 subtype compared to the CARMENCITA data base. The final quality of the results that close to the data base values is even better than expected. The original *THE HAMMER* program works with a accuracy of ±2 subtypes for K and M type stars (Covey et al., 2001). The calculated errors are even smaller than 2 subclasses. Despite of a few outliers the error of the spectral typing is 1.2 subclasses or smaller.
Thus, the used method calculating a reference type and dividing the spectra in groups seems to have worked successfully. For the different groups only a few but very sensitive calibration functions were used. Two former bachelor theses written in the same group worked on spectral typing based on *THE HAMMER*, too. Both used an approach using as many index lines as possible appearing in M-dwarf spectra. Schöfer (2013) who used only FEROS data got a similar accuracy compared to literature values and even similar errors like in this thesis. 93 of 100 stars which are observed in both theses do not differ more than 0.5 subclasses. Mrotzek (2013) worked on HRS spectra only. Here, only a few stars were used also in this thesis. All of them are determined with much later spectral types here. The literature shows later values, too. It can not be ruled out that in this bachelor thesis the same problems with HRS spectra occurred than the ones described in section 3.3.

Literature values of the CARMENCITA database were collected from several sources. Many spectral types are from, e.g., Reid et al. (1995) and Lepine et al. (2013). That no systematic differences to the different sources can be found give additional hints that the results of this thesis are reliable.
348 of the analyzed 900 spectra taken with CAFE were only available as raw data and had to be reduced for every single night before the analysis runs. The used Package *REDUCE* was not able to find spectral orders in the required infrared wavelength range. It was necessary to modify the order definition process to extract the flux in a sufficient wavelength range. The used modification did not change the flux

values of the orders, but these between the orders. Thus, it is guaranteed that the extracted spectrum was not affected. A new extraction process *FOX* (Zechmeister et al., 2013) was implemented in *REDUCE*. This fast working procedure provided more precise results. During the reduction or analysis occurred problems like bright spots on the images made it necessary to reject spectra taken in nine nights from the list of investigated spectra. It was tried to recover the data by flatfielding or by handle the spot like straylight. Both attempts were not successful. For each observation night of CAFE a wavelength calibration was performed by comparing the known wavelengths of a ThAr spectrum with an observed spectrum. Some of these calibrations had to be repeated because the order definition process missed an order. For every case where the order definition process missed an order this was noticed during the calibration at the latest. The radial velocity accuracy of the wavelength calibration was around 90 ms^{-1}. Thus, this effect can be neglected compared to the calculated radial velocities.

The biggest problem during the determination of spectral types was the choosing of the normalization procedure. Both the normalization by a polynomial and the way using a reference star are justifiable. However, the results of both ways differed from each other by 0.5 to 1 subtype. Eventually the normalization process using a reference star was used because its results were closer to the literature values and this way does not depend on the choice of any polynomial degree. That means that the fit to the continuum of the reference stars does not depend as strong to the polynomial degree as for the investigated stars.
This distinctions of the results underline the importance of defining a normalization process for the spectral typing, especially for M-dwarfs. Earlier types show a continuum which can be fitted much easier. It is not mentioned how the spectra of the *THE HAMMER* calibration functions were normalized. All spectra which were analyzed with calibration functions should be handled in the same way than the calibration spectra.
The analysis of deviations of every single spectral type (see Figure 4.6) showed a systematic change from a difference of +0.5 subtypes for early types to -0.5 for late spectral types. This could be caused by the use of different groups of indices. In this case a sudden jump between M3 and M4 would be expected. This jump can not be seen, but a continuous shift. It seems possible that this shift originates from the normalization process or that it is a systematic error of the literature values. However, the latter seems very unlikely because various sources were used. It is

also feasible that the shift is produced by the calibration functions. The number of usable stars decreased with later types, even for data of *THE HAMMER*. Maybe the low number of data points in the calibration functions induce this systematic shift. Eventually, the best explanation for this systematic change seems to be the normalization process or a systematic error in the calibration function.
The analysis of radial velocities did not work with the accuracy the spectrographs were developed for (see section 2.2.1) . For every spectrum five wavelength ranges were used to investigate the radial velocities and an average were calculated from them. The cross correlation functions did not show a perfect Gaussian function in case of many spectra, so it was hard to fit the Gaussian function. This deviations led to differences of the peak position between the single wavelength ranges of around 1 km/s. It could be possible that a more accurate investigation of the radial velocity would lead to accuracies of around 20 m/s like given in the publications. To achieve this the analysis of the whole wavelength range and an analysis of much more lines is necessary. Additionally, it is important to use appropriate synthetic spectra for fast rotating stars. The cross correlation functions of these stars were very broad. A determination of radial velocity and rotational velocity in one procedure seems to promise a better determination of radial velocities.
The biggest problem during the investigation of the activity indicator A was to find the threshold value at which H_α changes from absorption to emission line. Due to the variations of the spectra around H_α the determined equivalent width could be positive, although H_α was an absorption line. This is no problem for the search of very active stars, here is the H_α emission well marked. An investigation of stars with a small H_α emission and even for stars showing only small absorption lines would be auxiliary.

During the analysis runs problems regarding the name of the stars occurred. Especially for CAFE many star names in the file headers contained typos or were completely wrong. This issue was solved by a cross match of the telescope coordinates and the expected coordinates of CARMENCITA. All multiple observed stars were checked for their radial velocity to find out if the right star was observed. For the different spectrographs the separation of the expected coordinates and the coordinates the telescope was pointed to have high variations. For FEROS almost all stars gave separations of $0.1'$ to $2.0'$ what is pretty fine. However, for CAFE and HRS the separation were in the dimension of $3' - 12'$ after the rejection of probably

wrong observations. This very high separation can not be explained by the proper motion of the stars. It seems that the pointing method of the FEROS telescope is different to the telescopes of CAFE and HRS.
It is very likely that the right star names were found, especially because the spectral types are matching that well, since they deviate only by an order of half a subtype. Additionally, stars with obviously wrong radial velocity measurements were sorted out. Nevertheless, for stars with just one observed spectrum it could be possible that a wrong star was observed with a similar spectral type close to the right star. Much more investigations would be necessary to find these discrepancies.

6. Conclusion

For this thesis 900 spectra taken from 364 M-dwarfs were used to determine the spectral type, radial velocity and the activity indicator of the H_α line. 842 of these spectra were usable. Based on the calibration functions from the project *THE HAMMER* a self-written fast processing IDL routine was used to analyze all high-resolution spectra automatically. For this spectral typing process only very sensitive lines categorized in different groups based on a reference spectral type were used.
The determined spectral types show deviations to literature values from low-resolution spectroscopy of around 1 spectral subtype and error bars in the same range. Thus, the used method to determine spectral types from high-resolution spectra can be categorized as fast, effective and reliable.
Nevertheless, the spectral type of a star is more a quantitative category than a real physical variable. Influences of activity have been discussed in this thesis but they are not included in the MK system. Furthermore the spectral type depends on the luminosity class, the second dimension of the MK system. This was not discussed here because all stars were M-dwarfs on the main sequence with luminosity class V. Small differences between the spectral types for one star measured by different methods are reasonable.
The analysis of the activity indicator A showed that most of the investigated stars do not show strong magnetic activity. The amount of active stars seems to increase for later spectral types like even found in former publications. Thus, the determination of the spectral type becomes more complicate for late type M-dwarfs because they are fainter (and thus, have a lower SNR) and show more activity features in average.
The radial velocity measurements were accurate in the order of 0.1 to 4 km/s. This is precise enough to correct the spectrum for the radial velocity shift to analyze the spectral type. However, to find earth-like exoplanets around these M-dwarfs the accuracy is much to low. To achieve this precision the CARMENES project will observe 300 M-dwarfs with a radial velocity accuracy of 1 m/s. The results of this

thesis will help to choose the most promising target stars for searching exoplanets with CARMENES. The calculated spectral types allow a better categorization of the target stars into the different target groups to select the best possible targets for the CARMENES survey. Additionally, it was shown that the spectral types determined by low-resolution spectroscopy listed in CARMENCITA are very close to the here calculated types with high-resolution spectroscopy. Thus, the used algorithm provides a fast and accurate determination of spectral types for high-resolution spectra with an accuracy of around 1 subtype.
However, a small shift wandering from 0.5 subtypes for early type M-dwarfs to -0.5 subtypes for late type M-dwarfs was detected. Whether this is caused by the used calibration functions or by the use of different spectral indices in this work is to be investigated in further analyses. Additional determinations on the properties of the target stars will help to improve and complete the CARMENES input catalog. For example, the effective temperature and the rotational velocity of the target stars will be calculated which can be used to define the habitable zone of these stars and to investigate their rotation as an additional activity indicator since activity and rapid rotation is often associated.
All in all, CARMENES will push the research of extra-solar planets to smaller masses and will be the first instrument which is able to find rocky planets orbiting late-type M-dwarfs in their habitable zone. Besides the detection of the single planets, the CARMENES survey will provide sufficient statistics to get an overall distribution of planets around M-dwarfs. It will be the first survey leading to robust statements about planet formation in the regime of low-mass stars. Thus, further investigations, e.g. numerical simulations, will enlarge our understanding of the formation and evolution of stars and planets, especially in the low-mass regime.

A. Appendix

On the following pages all rejected spectra are listed in table A.1 and an overview of the results for every single investigated stars is given in table A.2.

Karm	Closest star	SpT	SpT	V_r	V_r	Date	Time	SNR	A	Spectro-	Err
				$[km/s]$	$[km/s]$					graph	
			Carm		Carm						
J00077+603	J03102+059	M4.0±0.9	M2.0	-6.4±0.2	87.1	20130203	19:55:49	10	-2.6	CAFE	1
J01026+623	J02019+735	M2.0±1.2	M4.5	-0.2±0.3	40.8	20130121	18:50:37	50	-8.2	CAFE	1
J02026+105	J02026+105	K5.5±1.5	M4.5	-8.1±0.3	-	20131114	02:18:27	50	-	FEROS	2
J02026+105	J02026+105	K6.0±1.0	M4.5	-7.7±0.2	-	20131114	02:49:19	40	-	FEROS	2
J02026+105	J02026+105	Na.0±0.5	M4.5	22.0±0.9	-	20131112	05:12:35	2	-66.	FEROS	3
J02190+353	J04311+589	M3.0±0.9	M4.0	-16.2±0.6	29.0	20130121	20:14:03	10	-5.7	CAFE	1
J02190+353	J04311+589	M3.0±0.9	M4.0	-15.9±0.6	29.0	20130121	20:52:25	10	-5.3	CAFE	1
J02336+249	J05019+011	M4.0±0.9	M4.0	-1.1±0.9	-3	20130203	21:03:25	10	-3.0	CAFE	1
J02362+068	J02362+068	K6.5±0.5	M4.0	26.4±0.4	24.8	20130105	00:23:00	150	-	FEROS	2
J02362+068	J02362+068	K3.5±0.5	M4.0	26.4±0.4	24.8	20130105	00:26:03	200	-	FEROS	2
J02441+492	J02441+492	Na.0±0.5	M1.5	25.2±0.6	27.7	20131031	03:14:23	350	-	CAFE	3
J03574-011	J03574-011	K5.0±2.0	M2.5	3.6±0.3	13.2	20130917	06:18:46	130	-	FEROS	2
J03574-011	J03574-011	K3.5±0.5	M2.5	4.8±0.5	13.2	20131122	06:25:37	270	-	FEROS	2
J05019+011	J05195+649	M4.0±0.9	M3.5	27.5±0.9	-	20130203	22:48:39	20	-2.3	CAFE	1
J05195+649	J07033+346	M4.0±0.9	M4.0	-42.3±0.5	8.7	20130204	00:06:50	20	-3.4	CAFE	1
J06171+751	J06171+751	M2.0±0.9	M2.0	-25.7±1.0	-28.3	20140110	00:47:21	10	-2.7	CAFE	1
J06307+397	J06307+397	M6.5±0.5	M2.0	33±25	-	20120926	10:38:18	10	-5.2	HRS	4
J06594+193	J06594+193	K3.5±0.5	M5.0	-1.8±0.3	-30.6	20130228	00:49:50	50	-	FEROS	2
J06594+193	J06594+193	K3.5±0.5	M5.0	-1.8±0.3	-30.6	20130228	00:49:50	50	-	FEROS	2

J07033+346	J11509+483	M3.5±1.1	M4.5	13.6±0.6	-26	20130204	04:05:57	20	-5.5	CAFE	1
J07582+413	J07582+413	M4.0±0.9	M4.0	8.6±0.5	8.7	20130204	01:18:05	20	-3.1	CAFE	1
J07583+496	J08066+558	M4.0±0.8	M2.0	-25.5±0.5	-47.6	20140112	01:41:47	30	-5.3	CAFE	1
J08005+258	J07319+392	M1.0±0.9	M3.0	12.2±0.2	16.1	20140111	01:01:15	20	-	CAFE	1
J08066+558	J09177+462	M2.0±0.9	M2.5	-29.0±0.2	-	20140112	02:59:42	40	-	CAFE	1
J09008+052W	J09008+052W	M0.0±0.9	M3.0	2.7±0.2	-35.4	20130103	06:27:40	120	-	FEROS	1
J09008+052W	J09008+052W	M0.5±1.1	M3.0	2.6±0.2	-35.4	20130105	05:51:58	100	-	FEROS	2
J09008+052W	J09008+052W	M0.5±1.1	M3.0	2.7±0.2	-35.4	20130106	05:27:25	110	-	FEROS	2
J09133+688	J08068+367	M2.0±0.9	M3.0	9.2±0.4	6.4	20140215	22:28:53	30	-4.8	CAFE	1
J09218-023	J09218-023	M2.0±2.0	M2.5	-94.4±0.6	-59	20111122	11:04:31	190	-	HRS	4
J09218-023	J09218-023	M5.0±1.0	M2.5	-75±3	-59	20111122	11:15:00	330	-5.1	HRS	4
J09218-023	J09218-023	M2.5±1.5	M2.5	-94.6±0.5	-59	20111122	11:25:56	180	-7.9	HRS	4
J09231+223	J09231+223	Na.0±0.5	M0.0	1.8±0.1	-	20131227	05:40:41	40	-	CAFE	3
J09319+363	J10143+210	M1.0±1.4	M0.5	20.6±0.3	2.7	20140108	06:33:14	50	-3.8	CAFE	1
J09423+559	J13195+351E	M3.5±1.1	M3.0	35.7±0.3	-11	20130122	03:18:22	20	-6.0	CAFE	1
J10143+210	J11355+389	M0.0±0.9	M3.5	18.6±0.4	-10.6	20140112	04:37:23	50	-4.0	CAFE	1
J10185-117	J10185-117	Na.0±0.5	M4.0	47±13	-	20140214	01:32:01	20	-	CAFE	3
J12373-208	J12471-035	M3.5±1.1	M3.0	6.7±0.4	-61.6	20140417	00:14:11	20	-6.2	CAFE	1
J12485+495	J13054+371	M3.0±0.9	M2.5	-1.6±2.0	-2.1	20140112	05:55:33	30	-2.6	CAFE	1
J12576+352E	J12576+352E	M5.0±1.2	M1.5	-13.1±0.6	-7.8	20130127	04:45:10	20	-2.6	CAFE	2
J12576+352E	J13254+377	M5.0±1.0	M0.0	-10.7±0.1	-	20130127	05:28:29	20	-2.5	CAFE	1.2
J13168+170	J13168+170	Na.0±0.5	M0.5	7.3±0.6	4.8	20130724	23:30:40	190	-	FEROS	3

J13229+244	J13215+037	M3.5±1.1	M1.0	-13.3±0.6	-	20130204	06:07:22	20	-5.4	CAFE	1
J13401+437	J13197+477	M3.0±0.9	M0.5	-31.4±0.8	1.9	20130127	06:01:32	30	-5.7	CAFE	1
J14257+236W	J16048+391	M0.5±0.5	M4.0	4.6±0.3	-56	20140220	06:18:57	50	-	CAFE	1
J16092+093	J16509+224	M3.0±0.9	M4.5	-41.4±0.5	-46	20130525	22:05:47	40	-5.4	CAFE	1
J16120+033	J18319+406	M1.5±0.5	M3.5	-2.5±0.1	-18.2	20140319	04:01:05	40	-	CAFE	1
J17395+277N	J21044+455	M2.0±0.9	M3.0	32.6±0.5	-	20130603	02:09:18	30	-6.1	CAFE	1
J19146+193N	J21044+455	M2.0±0.9	M3.5	-88.4±0.9	-	20130604	02:10:03	60	-2.4	CAFE	1
J20198+229	J20301+798	M3.0±0.9	M3.0	-29.2±1.3	-	20131028	21:47:27	40	-2.7	CAFE	1
J22231-176	J22231-176	M6.5±0.5	M4.5	-0.8±0.3	-2.1	20131115	02:26:18	40	-2.7	FEROS	4
J22231-176	J22231-176	M6.5±0.5	M4.5	0.1±1.7	-2.1	20131125	02:18:11	30	-3.1	FEROS	4

Table A.1.: List of reject spectra. The first column gives the star name written in the header. Column 2 shows the closest star in CARMENCITA where the telescope was pointed to. The reason to reject this spectra is given in the last column by a error code described in this section. The literature value in column 4 and 6 are taken from the CARMENCITA database.

Karmn	SpT	SpT	v_r $[km/s]$	v_r $[km/s]$	A	N	Spectro	Name
		Carm		Carm				
J00051+457	M1.5±1.07	M1.0	-1.00±0.19	0.4	-	1	CAFE	GJ 2
J00056+458	M1.0±1.38	M0.0	-0.80±0.23	0.0	-	1	CAFE	HD 38B
J00077+603	M4.5±0.70	M4.0	4.90±0.85	0.0	-2.80	1	CAFE	G 217-032
J00088+208	M4.0±0.52	M4.5	11.24±0.60	9.0	-2.55±0.04	2	CAFE	LP 404-033
J00162+198E	M4.5±0.32	M4.0	-0.70±0.18	2.2	-	4	FEROS	LP 404-062
J00162+198W	M4.5±0.29	M4.0	24.46±0.13	-17.4	-2.75±0.02	4	FEROS	EZ Psc
J00286-066	M4.0±0.52	M4.0	-11.56±0.36	-13.4	-	2	FEROS	GJ 1012
J00315-058	M3.0±0.40	M3.5	-9.70±0.32	0.9	-	4	FEROS	GJ 1013
J00395+149S	M3.5±0.29	M4.0	17.03±0.41	0.0	-4.17±0.02	3	HRS	LP 465-061
J00443+126	M3.0±0.55	M3.5	33.15±0.21	42.8	-	2	FEROS	G 032-044
J00502+086	M4.5±0.36	M4.5	-31.06±1.69	0.0	-2.40	3	HRS	RX J0050.2+0837
J00566+174	M3.5±0.49	M4.0	-26.33±0.28	-43.5	-	3	FEROS	GJ 1024
J00570+450	M3.0±0.83	M3.0	7.90±0.37	-23.3	-	1	CAFE	G 172-030
J00580+393	M4.5±0.29	M4.5	-30.14±0.76	0.0	-3.37±0.03	3	HRS	1RXS J005802.4+39191
J01009-044	M3.5±0.36	M4.0	30.56±0.19	42.3	-	3	FEROS	GJ 1025
J01256+097	M4.0±0.44	M4.0	-15.42±0.14	-17.2	-	3	FEROS	Wolf 66
J01384+006	M1.5±0.75	M2.0	0.40±0.08	-3.2	-	1	FEROS	G 071-024
J01466-086	M3.0±0.52	M4.0	53.71±0.14	54.3	-	3	FEROS	LP 708-416
J02026+105	M4.0±0.40	M4.5	22.42±0.21	0.0	-2.80	4	FEROS	RX J0202.4+1034
J02033-212	M2.0±0.97	M2.5	6.00±0.41	0.3	-	1	FEROS	G 272-145

J02050-176	M2.5±0.21	M2.5	23.41±0.12	25.1	-	13	FEROS	BD-18 359 AB
J02070+496	M3.0±0.59	M3.5	18.78±0.27	0.0	-	2	CAFE	G 173-037
J02096-143	M2.0±0.97	M2.5	17.40±0.25	20.2	-	1	FEROS	LP 709-040
J02116+185	M3.0±0.69	M3.0	-54.72±0.27	0.0	-	2	FEROS	G 035-032
J02123+035	M1.0±1.00	M1.5	-3.00±0.52	-3.1	-	1	FEROS	BD+02 348
J02129+000	M4.5±0.24	M4.0	28.26±0.10	30.0	-3.50±0.04	6	FEROS	G 159-046
J02190+353	M3.5±1.07	M3.5	-26.80±0.56	-13.6	-	1	CAFE	Ross 19
J02222+478	M0.0±0.83	M0.5	-38.30±0.28	-31.4	-	1	CAFE	BD+47 612
J02289+120	M2.0±0.78	M2.0	-54.10±0.74	-52.9	-	1	FEROS	[R78b] 140
J02336+249	M4.5±0.37	M4.0	-5.80±0.09	-3.0	-3.17±0.04	4	MULTI	GJ 102
J02358+202	M2.0±0.45	M2.0	0.83±0.09	-1.8	-	3	MULTI	BD+19 381
J02362+068	M4.0±0.78	M4.0	26.40±0.08	24.8	-	1	FEROS	BX Cet
J02530+168	M6.5±0.29	M7.0	18.43±5.67	63.0	-	3	HRS	Teegarden's St
J02534+174	M2.0±0.55	M3.5	-31.71±0.08	0.0	-	2	FEROS	NLTT 9223
J02581-128	M2.5±0.53	M2.5	100.78±0.11	99.1	-	2	FEROS	LP 711-032
J03026-181	M2.0±0.78	M2.5	19.90±0.14	41.0	-	1	FEROS	GJ 121.1
J03040-203	M4.0±0.71	M3.5	29.40±0.48	22.4	-	1	FEROS	LP 771-077
J03102+059	M2.0±0.78	M2.0	-5.40±0.73	87.1	-	1	FEROS	EK Cet
J03133+047	M6.0±0.41	M5.0	28.52±0.09	26.0	-	2	FEROS	CD Cet
J03194+619	M4.0±0.43	M4.0	-1.18±0.69	0.0	-2.40	3	HRS	G 246-033
J03217-066	M2.0±0.78	M2.0	27.00±0.48	29.7	-	1	FEROS	G 077-046
J03233+116	M2.5±0.50	M2.5	5.70±0.99	-45.2	-3.20	1	FEROS	G 005-032

J03242+237	M2.5±1.07	M2.0	20.20±0.21	19.1	-	1	CAFE	GJ 140C
J03263+171	M4.0±0.30	M4.0	-3.85±0.31	0.0	-	6	HRS	TYC 1237-889.
J03303+346	M3.5±0.36	M4.0	-18.36±1.28	0.0	-2.23±0.02	3	HRS	2M J03302331+344032
J03317+143	M2.0±0.45	M2.0	-32.20±0.17	-33.5	-	3	FEROS	GJ 143.3
J03346-048	M3.0±0.55	M3.5	12.02±0.40	9.5	-	2	FEROS	LP 653-008
J03366+034	M4.5±0.47	M4.5	20.96±0.82	15.0	-2.20±0.07	2	FEROS	[R78b] 233
J03430+459	M4.0±0.48	M4.0	-46.63±0.33	0.0	-4.30±0.06	3	HRS	NLTT 11633
J03438+166	K7.5±0.35	M0.0	34.66±0.19	37.8	-	2	FEROS	BD+16 502A
J03463+262	M0.0±0.56	M0.0	36.56±0.23	36.0	-	2	MULTI	HD 23453
J03473-019	M2.5±0.53	M3.0	17.36±0.26	0.0	-2.80	2	FEROS	G 080-021
J03507-060	M3.5±0.53	M3.5	-9.06±0.22	-10.1	-	2	FEROS	GJ 1065
J03526+170	M4.5±0.25	M4.5	36.41±0.21	28.0	-4.18±0.12	4	FEROS	Wolf 227
J03531+625	M2.5±0.50	M3.0	-119.20±0.16	0.0	-	1	CAFE	Ross 567
J03588+125	M4.5±0.32	M4.0	22.46±0.29	0.0	-	3	HRS	G 007-014
J03598+260	M3.0±0.59	M3.0	53.31±0.27	42.0	-	2	CAFE	Ross 873
J04148+277	M3.0±0.59	M3.5	37.76±0.39	0.0	-3.50	2	CAFE	HG 8-1
J04153-076	M4.5±0.70	M4.5	-43.20±0.21	-41.5	-2.80	1	FEROS	omi02 Eri C
J04173+088	M4.5±0.50	M4.5	18.40±1.22	14.0	-1.85±0.04	2	FEROS	LTT 11392
J04224+036	M4.0±0.45	M3.5	-1.31±0.38	0.0	-2.53±0.03	3	HRS	RX J0422.4+033
J04225+105	M3.0±0.45	M3.5	37.05±0.10	0.0	-	4	FEROS	LSPM J0422+103
J04252+080S	M2.0±0.78	M2.5	48.30±0.41	33.0	-3.60	1	FEROS	HG 7-206
J04311+589	M3.5±1.07	M4.0	30.80±0.49	29.0	-	1	CAFE	Stein 2051A

J04376-110	M2.0±0.53	M1.5	-6.78±0.11	-5.7	-	2	FEROS	BD-11 916
J04429+189	M2.0±0.97	M2.0	26.60±0.70	26.5	-	1	FEROS	HD 285968
J04429+214	M3.0±0.38	M3.5	3.22±0.05	0.0	-	5	MULTI	2M J04425586+212823
J04488+100	M3.0±0.38	M3.0	7.57±0.18	0.0	-3.80±0.05	4	FEROS	1RXS J044847.6+10030
J04499+236	M0.5±1.44	M1.0	-34.12±1.86	0.0	-3.00	3	HRS	EM* LkCa 18
J04524-168	M3.0±0.66	M3.0	27.66±0.25	26.7	-2.70	2	CAFE	LP 776-025
J04544+650	M4.5±0.24	M4.0	-25.86±0.40	0.0	-2.80±0.03	6	HRS	1RXS J045430.9+65045
J04588+498	M0.5±0.71	M0.0	-33.64±0.16	-36.0	-	2	CAFE	BD+49 1280
J04595+017	K7.5±0.50	M0.0	19.40±0.65	18.7	-3.70	1	FEROS	V1005 Ori
J05012+248	M2.0±0.59	M2.0	30.65±0.25	39.4	-	2	CAFE	Ross 794
J05019-069	M4.0±0.55	M4.0	42.03±0.24	41.4	-3.80±0.28	2	FEROS	LP 656-038
J05019+011	M4.5±0.33	M4.0	19.38±0.31	0.0	-2.30±0.03	4	MULTI	1RXS J050156.7+01084
J05032+213	M2.5±0.43	M1.5	69.40±0.42	47.0	-	2	CAFE	HD 285190 A
J05034+531	M1.0±0.83	M0.5	65.60±0.52	66.3	-	1	CAFE	BD+52 911
J05050+442	M5.0±0.45	M5.0	-32.23±0.68	0.0	-	3	HRS	2M J05050591+441403
J05062+046	M4.5±0.35	M4.0	20.28±0.68	0.0	-2.37±0.02	3	FEROS	RX J0506.2+043
J05078+179	M2.5±0.35	M3.0	23.31±0.11	20.1	-	2	FEROS	G 085-041
J05091+154	M2.5±0.75	M3.0	-25.10±0.76	-8.9	-2.90	1	FEROS	Ross 388
J05187+464	M4.5±0.29	M4.5	-40.11±1.85	0.0	-1.80	3	HRS	2M J05184455+462959
J05195+649	M3.5±1.07	M3.5	-44.20±0.69	0.0	-3.40	1	CAFE	1RXS J051929.3+64543
J05280+096	M3.0±0.55	M3.5	61.20±0.30	52.0	-	2	FEROS	Ross 41
J05298-034	M2.5±0.75	M2.5	21.90±0.75	19.7	-	1	FEROS	Wolf 1450

J05298+320	M2.0±0.59	M3.0	-9.66±0.35	-12.7	-	2	CAFE	Ross 406
J05322+098	M3.5±0.50	M3.5	-	17.2	-2.90	1	FEROS	V998 Ori
J05333+448	M3.5±0.32	M3.5	23.38±0.16	58.9	-3.68±0.02	5	CAFE	GJ 1081
J05337+019	M2.5±0.75	M2.5	65.20±0.80	19.6	-2.40	1	FEROS	V371 Ori
J05365+113	K7.5±0.75	M0.0	22.10±0.06	17.8	-	1	FEROS	V2689 Ori
J05366+112	M4.0±0.53	M4.0	21.80±0.15	0.0	-3.25±0.04	2	FEROS	2M J05363846+1117487
J05466+441	M4.0±0.43	M4.0	14.23±0.18	32.1	-	4	CAFE	Wolf 237
J05532+242	M2.0±0.59	M1.5	25.07±0.19	32.3	-	2	CAFE	Ross 59
J05566-103	M3.5±0.46	M3.5	22.68±0.24	0.0	-2.83±0.03	3	FEROS	1RXS J055641.0-10183
J06000+027	M3.5±0.42	M4.0	28.44±0.55	30.0	-3.30	2	FEROS	G 099-049
J06007+681	M3.5±0.43	M4.0	29.34±0.27	75.6	-	2	CAFE	LP 057-040
J06024+663	M4.5±0.27	M4.5	-55.03±0.34	0.0	-	6	HRS	G 249-032
J06102+225	M4.5±0.26	M4.0	-22.61±0.40	0.0	-2.27±0.13	6	HRS	2M J06101775+223419
J06103+821	M3.5±1.07	M2.0	9.00±0.63	-1.1	-	1	CAFE	GJ 226
J06171+751	M1.0±0.59	M2.0	-26.08±1.94	-28.3	-2.65±0.04	2	CAFE	TYC 4525-194-1
J06246+234	M4.0±0.59	M4.0	-10.13±0.38	-12.0	-	2	CAFE	Ross 64
J06277+093	M2.0±0.75	M2.0	41.60±0.43	0.0	-	1	FEROS	Ross 603
J06307+397	M2.5±0.48	M2.0	-56.47±0.23	0.0	-	5	HRS	2M J06304724+394737
J06325+641	M4.0±0.33	M4.0	0.04±0.26	0.0	-	6	HRS	LP 057-192
J06354-040	M5.5±0.80	M5.5	49.40±1.04	0.0	-2.60	1	FEROS	2M J06352986-040318
J06371+175	K7.5±0.35	M0.0	-60.36±0.79	-55.0	-	2	FEROS	HD 260655
J06396-210	M3.0±0.59	M4.0	-6.80±0.37	0.0	-4.10±0.21	2	CAFE	LP 780-032

J06400+285	M2.5±0.35	M2.0	-23.20±0.22	-46.0	-	2	CAFE	LP 307-008
J06421+035	M2.5±0.66	M3.5	81.99±0.29	82.0	-	2	FEROS	G 108-021
J06422+035	M3.5±0.54	M4.0	82.63±0.19	81.7	-	2	FEROS	G 108-022
J06524+182	M3.0±0.56	M4.0	11.96±0.07	13.7	-	3	FEROS	LP 421-007
J06565+440	M4.5±0.29	M4.5	-27.24±0.62	0.0	-	3	HRS	G 107-036
J06574+740	M4.0±0.44	M4.0	-11.18±0.42	0.0	-2.30	4	CAFE	2M J06572616+740526
J07033+346	M4.0±0.83	M4.0	2.90±0.24	8.7	-3.10	1	CAFE	LP 255-011
J07044+682	M2.5±1.07	M3.0	-48.70±0.41	-43.5	-	1	CAFE	GJ 258
J07119+773	M0.5±0.55	M1.5	4.35±0.24	0.0	-	4	CAFE	TYC 4530-1414-
J07181+392	M0.0±0.83	M0.0	9.70±0.66	11.2	-	1	CAFE	Ross 987
J07195+328	K7.5±0.50	M0.0	-69.70±0.16	-76.0	-	1	CAFE	BD+33 1505
J07274+052	M3.0±0.55	M3.5	18.16±0.11	15.0	-	2	FEROS	Luyten's Star
J07282-187	M4.5±0.23	M4.5	75.26±0.08	70.9	-	7	FEROS	LP 782-002
J07319+362N	M3.5±1.07	M3.5	0.40±0.49	0.7	-3.30	1	CAFE	BL Lyn
J07349+147	M2.5±0.75	M3.0	30.90±0.35	0.0	-3.40	1	FEROS	TYC 777-141-1
J07361-031	M0.5±0.75	M1.0	-16.00±0.50	-22.7	-4.50	1	FEROS	BD-02 2198
J07366+440	M3.5±0.56	M3.5	64.43±0.38	0.0	-	3	HRS	G 111-020
J07386-212	M3.0±0.75	M3.0	-28.50±0.47	-29.5	-	1	FEROS	LP 763-001
J07393+021	K7.5±0.29	M0.0	19.79±0.04	18.9	-	3	FEROS	BD+02 1729
J07418+050	M2.5±0.42	M2.5	-1.72±0.19	23.3	-	2	FEROS	G 050-001
J07446+035	M4.5±0.48	M4.5	26.93±0.65	30.0	-2.30	2	CAFE	YZ CMi
J07467+574	M4.5±0.21	M4.5	-33.97±0.70	0.0	-2.65±0.06	6	HRS	G 193-065

J07472+503	M4.0±0.35	M4.0	-14.40±0.22	0.0	-2.97±0.06	6	CAFE	2M J07471385+502038
J07545+085	M3.0±0.35	M2.5	-18.36±0.13	0.0	-	7	MULTI	LSPM J0754+083
J07558+833	M4.0±0.59	M4.5	8.67±0.53	6.7	-2.65±0.04	2	CAFE	GJ 1101
J07582+413	M3.0±0.66	M3.5	-20.37±0.35	-19.0	-	2	CAFE	GJ 1105
J07583+496	M4.5±1.01	M3.5	-25.50±0.38	-22.0	-	1	CAFE	LP 163-047
J08017+237	M1.5±0.43	M1.5	9.10±0.42	0.0	-	2	CAFE	TYC 1926-794-1
J08066+558	M2.0±0.83	M2.0	-36.20±0.28	-47.6	-	1	CAFE	LP 123-075
J08105-138	M2.0±0.78	M2.5	32.60±0.27	20.9	-	1	FEROS	GJ 297.2B
J08161+013	M2.0±0.97	M2.0	62.00±0.14	46.0	-	1	FEROS	GJ 2066
J08293+039	M1.5±0.90	M2.5	22.40±0.31	0.0	-	1	FEROS	2M J08292191+035509
J08313-060	M1.0±1.14	M1.5	73.80±0.46	65.5	-	1	FEROS	LP 665-021
J08314-060	M2.0±1.00	M3.0	74.90±0.63	75.1	-	1	FEROS	LP 665-022
J08344-011	M3.0±0.75	M3.5	60.30±0.23	81.1	-	1	FEROS	LP 605-037
J08371+151	M2.5±0.75	M2.5	83.00±0.50	80.8	-	1	FEROS	NLTT 19893
J08375+035	M3.5±0.36	M4.0	-41.94±0.45	0.0	-	3	HRS	LSPM J0837+0333
J08428+095	M2.5±0.75	M2.5	21.50±0.78	2.7	-	1	FEROS	BD+10 1857 C
J08468+760	M1.0±0.59	M1.5	-27.86±0.22	-26.2	-	2	CAFE	BD+76 3952
J08551+015	K7.5±0.35	M0.0	-3.90±0.16	-7.0	-	2	FEROS	BD+02 2098
J09005+465	M4.0±0.59	M4.5	4.23±0.25	0.8	-3.90±0.07	2	CAFE	GJ 1119
J09008+052E	M3.0±0.69	M3.5	-37.07±0.49	-27.2	-	2	FEROS	Ross 687
J09008+052W	M3.0±0.97	M3.0	-37.50±0.25	-35.4	-	1	FEROS	Ross 686
J09011+019	M3.0±0.69	M3.0	57.47±0.43	49.0	-	2	FEROS	Ross 625

J09023+084	M2.0±0.78	M2.5	39.80±0.70	42.2	-	1	FEROS	NLTT 20817
J09028+680	M2.5±1.07	M4.0	-44.00±0.25	-25.2	-	1	CAFE	LP 060-179
J09120+279	M3.5±1.07	M3.0	-11.10±0.22	36.4	-	1	CAFE	G 047-028
J09133+688	M2.0±0.48	M2.5	13.77±0.13	0.0	-	3	CAFE	G 234-057
J09140+196	M2.0±0.55	M3.0	12.43±0.35	0.0	-	2	FEROS	LP 427-016
J09143+526	K7.5±0.47	M0.0	11.67±0.19	5.7	-	2	CAFE	HD 79210
J09161+018	M3.5±0.38	M4.0	-12.69±0.59	0.0	-2.65±0.03	4	FEROS	RX J0916.1+015
J09163-186	M1.0±0.40	M1.5	14.24±0.11	15.5	-	4	FEROS	LP 787-52
J09177+462	M2.0±0.59	M2.5	0.21±0.63	0.0	-2.70	2	CAFE	RX J0917.7+4612
J09218-023	M2.0±0.78	M2.5	-57.30±0.23	-59.0	-	1	FEROS	RAVE J092148.1-02194
J09231+223	K5.5±0.50	M0.0	0.50±0.23	0.0	-	1	CAFE	BD+22 2086B
J09256+634	M4.0±0.43	M4.5	0.08±0.35	0.0	-2.90	3	HRS	G 235-025
J09288-073	M2.5±0.75	M2.5	8.50±0.31	9.9	-	1	FEROS	Ross 439
J09307+003	M3.0±0.78	M3.5	46.50±0.16	44.1	-	1	FEROS	GJ 1125
J09423+559	M3.5±0.76	M3.5	17.36±0.26	11.0	-	2	CAFE	GJ 363
J09425-192	M2.0±0.78	M2.5	44.70±0.69	41.0	-	1	FEROS	LP 788-024
J09439+269	M2.5±1.07	M3.5	36.20±0.33	32.9	-	1	CAFE	Ross 93
J09449-123	M5.5±0.48	M5.0	-	0.0	-1.57±0.1	3	CAFE	G 161-071
J09475+129	M3.0±0.48	M4.0	49.79±0.39	70.9	-	3	FEROS	LP 488-037
J09506-138	M3.5±0.27	M4.0	25.03±0.21	0.0	-	6	CAFE	LP 728-070
J09511-123	M0.0±0.39	M0.5	61.64±0.15	60.8	-	4	FEROS	BD-11 2741
J09531-036	M2.0±0.97	M2.0	61.10±0.54	24.0	-	1	FEROS	GJ 372

J09561+627	M0.0±0.46	M0.0	15.41±0.11	16.9	-	4	CAFE	BD+63 869
J10087+027	M3.0±0.69	M3.0	29.99±0.05	0.0	-	2	FEROS	LP 549-023
J10094+512	M3.5±0.30	M4.0	48.32±0.36	43.9	-	5	CAFE	LP 127-132
J10143+210	M0.0±0.83	M0.0	27.60±0.22	20.8	-	1	CAFE	BD+36 1970
J10158+174	M3.5±0.35	M3.5	26.05±0.33	0.0	-	2	CAFE	LSPM J1015+172
J10167-119	M2.5±0.90	M3.0	-10.70±0.11	-9.9	-	1	FEROS	GJ 386
J10185-117	M2.5±0.31	M4.0	1.63±0.19	0.0	-	4	CAFE	LP 729-054
J10243+119	M2.0±0.53	M2.0	-4.80±0.14	8.1	-	2	FEROS	StKM 1-852
J10251-102	M1.0±0.78	M1.0	20.90±0.28	22.7	-	1	FEROS	BD-09 3070
J10289+008	M2.0±0.97	M2.0	8.40±0.25	9.0	-	1	FEROS	BD+01 2447
J10350-094	M2.0±0.34	M3.0	14.12±0.24	0.0	-	3	CAFE	LP 670-017
J10360+051	M3.5±0.41	M3.5	20.50±0.18	17.0	-2.45±0.02	4	FEROS	RY Sex
J10379+127	M2.5±0.35	M3.0	16.65±0.61	0.0	-	2	CAFE	LP 490-042
J10396-069	M2.0±0.78	M2.5	3.80±0.21	3.7	-	1	FEROS	GJ 399
J10504+331	M3.5±0.76	M4.0	-58.64±0.25	-55.1	-	2	CAFE	G 119-037
J10508+068	M4.5±0.34	M4.0	0.27±0.07	-2.5	-	5	MULTI	EE Leo
J10520+139	M3.0±0.55	M3.5	22.55±0.09	18.0	-	2	FEROS	GJ 403
J10546-073	M4.5±0.31	M4.0	28.90±0.15	0.0	-	6	CAFE	LP 671-008
J10564+070	M6.5±0.22	M6.0	19.07±0.25	23.0	-2.53±0.01	7	MULTI	CN Leo
J11026+219	M0.0±0.48	M2.0	-13.57±0.18	-14.2	-	3	CAFE	DS Leo
J11033+359	M2.0±0.83	M1.5	-83.00±0.37	-85.9	-	1	CAFE	HD 95735
J11036+136	M3.5±0.53	M4.0	-20.60±0.55	0.0	-3.00±0.07	2	FEROS	LP 491-051

J11054+435	M0.0±0.83	M1.0	70.10±0.20	69.6	-	1	CAFE	BD+44 2051A
J11057+102	M2.5±0.35	M2.5	-56.80±0.12	-61.7	-4.00	2	FEROS	LP 491-060
J11075+437	M2.5±0.45	M3.0	-17.65±0.59	0.0	-3.80	2	HRS	HAT 141-00828
J11081-052	M2.5±0.38	M3.0	22.95±0.10	32.7	-	4	FEROS	GJ 1142 A
J11110+304	M2.0±0.59	M2.0	-15.10±0.19	-12.6	-	2	CAFE	BD+31 2240B
J11152+194	M3.0±0.54	M3.5	23.49±0.48	38.2	-	2	FEROS	G 056-026
J11289+101	M3.5±0.75	M3.5	36.80±0.27	32.0	-	1	FEROS	Wolf 398
J11417+427	M3.5±1.07	M4.0	-8.70±0.32	-9.8	-	1	CAFE	Ross 1003
J11421+267	M3.0±0.83	M2.5	10.60±0.22	12.0	-	1	CAFE	Ross 905
J11476+002	M4.0±0.57	M4.0	7.63±0.44	6.0	-2.75±0.04	2	FEROS	LP 613-049 A
J11476+786	M3.0±1.16	M3.5	-109.90±0.69	-112.0	-	1	CAFE	GJ 445
J11477+008	M4.0±0.78	M4.0	-31.10±0.54	-31.3	-	1	FEROS	FI Vir
J11509+483	M4.0±0.83	M4.5	-34.70±0.69	-26.0	-	1	CAFE	GJ 1151
J11521+039	M3.0±0.55	M4.0	28.51±0.39	0.0	-	2	FEROS	StM 162
J11532-073	M2.0±0.47	M2.5	26.35±0.23	25.6	-	3	FEROS	GJ 452
J11541+098	M3.5±0.53	M3.5	1.00±0.28	3.5	-4.20	2	FEROS	Ross 119
J11549-021	M3.0±0.43	M3.0	-11.62±0.31	0.0	-	3	HRS	2M J11545693-020609
J12006-138	M3.0±0.78	M3.5	-16.70±0.48	-6.3	-	1	FEROS	LP 734-011 A
J12016-122	M2.5±0.90	M3.0	-39.20±0.32	-36.2	-	1	FEROS	LTT 4484
J12054+695	M3.5±0.79	M4.0	-45.96±0.27	-3.0	-	2	CAFE	Ross 689
J12100-150	M4.0±0.40	M3.5	82.93±0.20	79.5	-	4	CAFE	LP 734-032
J12112-199	M3.0±0.39	M3.5	-9.01±0.09	-3.7	-	4	FEROS	LP 794-031

J12156+526	M4.0±0.42	M4.0	-8.57±0.11	0.0	-2.17±0.07	4	CAFE	StKM 2-809
J12191+318	M3.0±0.42	M4.0	8.24±0.30	0.0	-	4	CAFE	LP 320-626
J12230+640	M2.0±1.16	M3.0	9.30±0.25	21.5	-	1	CAFE	Ross 690
J12277-032	M3.0±0.59	M3.5	3.70±0.25	0.0	-	2	CAFE	LP 615-149
J12290+417	M4.0±0.45	M3.5	-0.12±0.22	-3.8	-3.38±0.01	4	CAFE	G 123-035
J12299-054W	M3.5±0.70	M3.5	-6.60±0.87	-12.4	-	1	FEROS	LP 675-076
J12312+086	K7.5±0.50	M0.5	19.40±0.26	15.2	-	1	FEROS	BD+09 2636
J12350+098	M2.0±0.69	M2.5	33.00±0.25	31.6	-	2	FEROS	GJ 476
J12373-208	M4.0±0.38	M4.0	9.31±0.21	0.0	-	5	CAFE	LP 795-038
J12388+116	M3.0±0.97	M3.0	-4.40±0.25	-2.3	-	1	FEROS	Wolf 433
J12428+418	M4.0±0.35	M4.0	-3.17±0.16	0.0	-2.95±0.09	4	CAFE	G 123-055
J12471-035	M3.0±0.75	M3.0	-18.50±0.36	-61.6	-	1	FEROS	LP 616-013
J12479+097	M3.0±0.55	M3.5	19.30±0.14	11.0	-	2	FEROS	Wolf 437
J12485+495	M3.5±0.38	M3.5	-7.97±0.40	0.0	-2.37±0.1	3	CAFE	RX J1248.5+493
J13143+133	M6.5±0.29	M6.0	-38.44±0.67	-9.0	-2.40±0.04	3	HRS	NLTT 33370 AB
J13180+022	M3.5±0.43	M3.5	5.93±0.48	4.8	-	2	CAFE	G 062-028
J13195+351E	M2.5±0.25	M3.0	-7.24±0.15	-11.0	-	6	CAFE	BD+35 2436B
J13195+351W	M0.0±0.59	M0.5	-15.31±0.20	12.1	-	2	CAFE	BD+35 2436Aab
J13229+244	M4.5±0.45	M4.0	-19.99±0.41	-19.0	-	2	CAFE	Ross 1020
J13283-023E	M3.0±0.49	M3.0	-39.06±0.22	-41.8	-	3	MULTI	Ross 486A
J13283-023W	M3.5±0.76	M4.0	-39.89±0.44	-21.6	-	2	CAFE	Ross 4862B
J13293+114	M2.5±0.64	M3.5	28.24±0.26	28.0	-	2	FEROS	GJ 513

J13386+258	M3.0±0.59	M3.0	-31.19±0.24	-22.4	-	2	CAFE	Ross 1022
J13417+582	M3.0±0.59	M3.5	-10.99±0.24	0.0	-3.30±0.07	2	CAFE	StM 187
J13536+776	M3.5±0.48	M4.0	-6.09±0.29	0.0	-2.33±0.27	3	CAFE	RX J1353.6+773
J13582+125	M3.0±0.45	M3.0	-9.62±0.14	-10.8	-	3	MULTI	Ross 837
J14010-026	M1.0±0.97	M1.0	-25.50±0.47	-25.3	-	1	FEROS	HD 122303
J14062+693	M2.5±0.43	M3.0	-23.88±0.17	0.0	-	2	CAFE	NLTT 36313
J14082+805	M1.0±0.59	M1.0	8.70±0.22	16.2	-	2	CAFE	BD+81 465
J14152+450	M2.5±0.76	M3.0	15.00±0.18	40.9	-	2	CAFE	Ross 992
J14171+088	M4.5±0.43	M4.5	-34.74±0.84	0.0	-	3	HRS	2M J14170731+085136
J14173+454	M4.0±0.35	M5.0	5.65±0.30	0.0	-2.66±0.06	5	CAFE	RX J1417.3+452
J14174+454	K7.5±0.50	M0.0	3.10±0.45	3.9	-	1	CAFE	BD+46 1951
J14251+518	M2.5±0.50	M2.5	-9.80±0.31	8.6	-	1	CAFE	tet Boo B
J14257+236E	M0.0±0.57	M0.5	8.46±0.16	8.6	-	2	MULTI	BD+24 2733B
J14257+236W	M0.0±0.59	M0.0	10.07±0.18	8.7	-	2	CAFE	BD+24 2733A
J14294+155	M1.5±0.90	M2.0	7.20±0.01	6.0	-	1	FEROS	Ross 130
J14310-122	M3.0±0.55	M3.5	-1.45±0.10	0.5	-	2	FEROS	Wolf 1478
J14320+738	M2.0±0.51	M2.0	-11.26±0.12	0.0	-	3	CAFE	G 255-055
J14331+610	M2.0±0.48	M2.5	-21.14±0.26	0.0	-	4	CAFE	G 224-013
J14342-125	M4.5±0.70	M4.0	-1.20±0.17	-1.9	-	1	FEROS	HN Lib
J14368+583	M3.0±0.83	M2.5	-66.40±0.43	-26.6	-3.80	1	CAFE	LP 098-132
J14472+570	M3.5±0.52	M4.0	-14.65±0.54	0.0	-1.83±0.03	3	HRS	RX J1447.2+570
J14524+123	M2.0±0.97	M2.0	4.90±0.23	5.7	-	1	FEROS	G 066-037

J14544+355	M2.5±0.79	M3.5	-39.60±0.25	-40.4	-	2	CAFE	Ross 1041
J15011+071	M3.0±0.48	M3.5	-18.22±0.41	-17.3	-	4	FEROS	Ross 1030
J15013+055	M3.0±0.53	M3.0	-5.72±0.20	-6.6	-	2	FEROS	G 015-002
J15073+249	K7.5±0.50	M0.0	-68.50±0.24	-53.1	-	1	CAFE	BD+25 2874
J15095+031	M2.5±0.75	M3.0	-32.50±0.44	-32.3	-	1	FEROS	Ross 1047
J15194-077	M2.5±0.43	M3.0	-9.83±0.40	-10.3	-	2	MULTI	HO Lib
J15218+209	M1.5±0.75	M1.5	7.30±0.77	7.4	-3.30	1	FEROS	OT Ser
J15357+221	M3.0±0.59	M3.5	-59.60±0.28	-59.9	-	2	CAFE	LP 384-018
J15412+759	M2.5±1.07	M3.0	-41.40±0.17	-42.2	-	1	CAFE	UU Umi
J15474-108	M2.0±0.78	M2.0	4.60±0.94	1.0	-	1	FEROS	LP 743-031
J15496+348	M4.0±0.59	M4.0	-69.28±0.14	-55.1	-4.20±0.21	2	CAFE	LP 274-008
J15583+354	M3.0±0.37	M3.5	10.37±0.18	21.0	-	5	CAFE	G 180-018
J15598-082	M1.5±0.97	M1.0	-16.90±0.55	-17.0	-	1	FEROS	BD-07 4156
J16017+301	M3.0±0.59	M3.0	8.69±0.23	43.2	-	2	CAFE	G 168-024
J16028+205	M4.5±0.42	M4.0	7.25±0.30	3.0	-	4	MULTI	GJ 609
J16092+093	M2.5±0.75	M3.0	-44.60±0.20	0.0	-	1	FEROS	G 137-084
J16120+033	M1.5±0.33	M3.5	8.85±0.06	0.0	-	3	CAFE	TYC 371-1053-
J16167+672N	M3.0±0.83	M3.0	-17.60±0.34	-19.1	-	1	CAFE	EW Dr
J16167+672S	K7.5±0.35	M0.0	-18.75±0.18	-28.3	-	2	CAFE	HD 147379
J16254+543	M1.0±1.38	M1.5	-12.80±0.14	-12.0	-	1	CAFE	GJ 625
J16255+260	M2.5±0.38	M3.0	-42.74±0.21	-44.3	-	3	CAFE	TT 14889
J16303-126	M3.0±0.97	M3.5	-21.00±0.20	-21.3	-	1	FEROS	V2306 Oph

J16313+408	M5.5±0.56	M5.0	-40.97±0.90	-21.0	-2.33±0.07	3	HRS	G 180-60
J16327+126	M2.5±0.50	M3.0	-32.79±0.18	-6.5	-	4	MULTI	GJ 1203
J16462+164	M2.5±0.75	M2.5	18.30±0.17	19.5	-	1	FEROS	LP 446-006
J16487+106	M2.0±0.83	M2.5	-23.20±0.13	0.0	-	1	CAFE	LSPM J1648+1038
J16509+224	M4.5±0.55	M4.5	-41.89±0.68	-46.0	-3.15±0.04	2	CAFE	G 169-029
J16591+209	M3.5±0.53	M3.5	7.32±0.25	0.0	-2.90	2	FEROS	RX J1659.1+205
J17033+514	M4.5±0.29	M4.5	25.39±0.50	42.0	-	3	HRS	G 203-042
J17071+215	M2.5±0.50	M3.0	-50.30±0.20	-50.3	-	1	CAFE	Ross 863
J17136-084	M3.0±0.69	M3.5	-0.94±0.41	-1.6	-	2	FEROS	V2367 Oph
J17158+190	M0.0±0.83	M0.5	-20.60±0.22	-16.1	-	1	CAFE	BD+19 3268
J17198+265	M5.0±0.26	M4.5	-35.28±0.18	-38.0	-2.22±0.11	4	MULTI	V639 Her
J17199+265	M3.0±0.83	M3.5	-35.40±0.47	-38.0	-3.50	1	CAFE	V647 Her
J17303+055	M0.0±0.59	M0.0	-12.29±0.13	-12.9	-	2	CAFE	BD+05 3409
J17355+616	M0.0±0.59	M0.5	-15.58±0.21	-14.0	-	2	CAFE	BD+61 1678C
J17395+277N	M3.0±0.53	M3.0	18.57±0.10	65.6	-	3	MULTI	LTT 15242
J17542+073	M4.5±0.35	M4.0	-28.85±0.19	-29.0	-	2	FEROS	GJ 1222
J17578+046	M4.0±0.78	M3.5	-110.20±0.26	-111.0	-	1	FEROS	Barnard's Star
J18022+642	M4.5±0.29	M5.0	-2.23±0.22	0.0	-2.63±0.06	3	HRS	LP 071-082
J18180+387E	M3.0±0.59	M3.0	1.01±0.25	1.0	-	2	CAFE	G 204-058
J18180+387W	M4.0±0.58	M4.0	-1.70±0.35	1.0	-	3	CAFE	G 204-057
J18319+406	M3.0±0.59	M3.5	-18.81±0.34	-18.2	-	2	CAFE	G 205-028
J18427+139	M4.0±0.53	M4.0	-33.98±0.15	-33.0	-2.90	2	FEROS	V816 Her

J18580+059	M0.5±0.75	M0.5	10.50±0.52	11.2	-	1	FEROS	BD+05 3993
J19146+193N	M3.0±0.83	M3.5	-28.60±0.34	-42.3	-	1	CAFE	Ross 733
J19463+320	M0.5±1.07	M0.5	-4.70±0.59	-7.0	-	1	CAFE	BD+31 3767A
J19464+320	M2.0±0.59	M2.0	-4.50±0.09	-5.7	-	2	CAFE	BD+31 3767B
J20187+158	M2.0±0.55	M2.5	-12.99±0.10	-45.5	-	2	FEROS	LTT 15944
J20198+229	M2.5±0.66	M3.0	-21.17±0.57	0.0	-2.70	2	FEROS	LP 395-008
J20301+798	M2.5±0.50	M3.0	-53.00±1.21	0.0	-2.80	1	CAFE	GSC 04593-01344
J20405+154	M4.5±0.29	M4.5	-82.08±0.49	-59.0	-	3	HRS	GJ 1256
J20407+199	M2.5±0.53	M2.5	-34.92±0.12	-46.8	-	2	FEROS	GJ 797B
J20445+089N	M3.0±0.69	M3.5	-39.54±0.33	-28.3	-	2	FEROS	LP 576-039
J20567-104	M2.0±0.61	M2.5	35.40±0.51	33.5	-	2	FEROS	Wolf 896
J20568-048	M3.5±0.64	M4.0	-42.69±0.35	-42.1	-3.20	2	FEROS	FR Aqr
J21012+332	M3.0±0.83	M3.0	-38.10±0.25	-37.0	-3.80	1	CAFE	LP 340-547
J21019-063	M2.0±0.55	M2.5	-14.99±0.10	-15.1	-	2	FEROS	Wolf 906
J21055+061	M3.0±0.61	M3.0	-12.14±0.24	0.0	-	2	FEROS	2M J21053205+060915
J21057+502	M3.0±0.58	M3.5	-15.50±0.48	0.0	-	3	HRS	2M J21054537+501543
J21127-073	M4.0±0.48	M3.5	-1.23±0.31	0.0	-	3	HRS	2M J21124559-071955
J21152+257	M2.5±0.53	M3.0	-15.55±0.15	-38.1	-	3	MULTI	LP 397-041
J21164+025	M2.5±0.46	M3.0	-21.63±0.06	0.0	-	3	FEROS	LSPM J2116+023
J21221+229	M0.5±0.90	M1.0	6.00±0.36	0.0	-	1	FEROS	GSC 02187-0051
J21323+245	M3.5±0.53	M3.5	2.26±0.17	6.0	-2.95±0.04	2	FEROS	LP 397-034
J21348+515	M3.0±0.83	M3.0	-13.20±0.49	-14.1	-	1	CAFE	Wolf 926

J21376+016	M4.5±0.29	M4.5	-51.12±0.92	0.0	-1.70	3	HRS	GSC 00543-00620
J21442+066	M2.5±0.54	M3.0	24.38±0.54	26.9	-4.30	2	FEROS	G 093-033
J21463+382	M4.0±0.83	M4.0	-81.10±0.40	-81.0	-	1	CAFE	LSPM J2146+3813
J21466+668	M4.0±0.48	M4.0	-13.45±0.54	0.0	-	3	HRS	G 264-012
J21472-047	M4.5±0.29	M4.5	-11.23±0.61	0.0	-4.47±0.1	3	HRS	2M J21471744-044440
J21574+081	M1.0±0.78	M1.5	-26.00±0.28	-27.0	-	1	FEROS	Wolf 953
J22012+283	M4.0±0.52	M4.0	-7.92±1.96	-7.0	-2.55±0.04	2	FEROS	V374 Peg
J22020-194	M3.0±0.55	M3.5	-22.60±0.12	-23.2	-	2	FEROS	LP 819-017
J22088+117	M5.0±0.43	M4.5	-18.13±0.57	0.0	-2.33±0.03	3	HRS	2M J22085034+1144131
J22114+409	M6.0±0.45	M5.5	-22.31±0.96	0.0	-3.17±0.03	3	HRS	1RXS J221124.3+41000
J22125+085	M2.5±0.38	M3.0	8.78±0.07	9.1	-	4	FEROS	Wolf 1014
J22137-176	M4.5±0.42	M4.5	-23.16±0.21	-24.8	-	3	FEROS	LP 819-052
J22231-176	M4.5±0.50	M4.5	-0.90±0.46	-2.1	-2.40±0.1	2	FEROS	LP 820-012
J22298+414	M4.5±0.49	M4.0	2.75±0.32	7.0	-	2	CAFE	G 215-050
J22426+176	M2.0±0.61	M2.5	-12.77±0.12	-24.7	-	2	FEROS	GJ 1271
J22468+443	M4.0±0.83	M3.5	1.30±0.67	0.4	-2.80	1	CAFE	EV Lac
J22509+499	M5.0±0.43	M4.0	-40.58±1.88	0.0	-2.37±0.03	3	HRS	2M J22505505+495913
J22559+178	M0.5±0.60	M1.0	-31.72±0.18	-33.2	-	2	FEROS	StKM 1-2065
J23096-019	M3.0±0.46	M3.5	-3.87±0.25	-11.7	-	4	FEROS	G 028-044
J23113+075	M3.0±0.43	M3.5	-10.27±0.15	-10.0	-	4	FEROS	NLTT 56083
J23174+382	M2.0±0.83	M2.5	-6.40±1.01	14.9	-	1	CAFE	G 190-017
J23175+063	M2.5±0.42	M3.0	25.98±0.38	-3.5	-	2	FEROS	G 029-019

J23194+790	M3.5±1.07	M3.5	-11.80±0.58	0.0	-2.10	1	CAFE	HD 220140B
J23216+172	M4.5±0.41	M4.0	-5.70±0.70	-7.6	-	2	FEROS	LP 462-027
J23234+155	M1.5±0.54	M2.0	-43.86±0.15	0.0	-	2	FEROS	LP 522-065
J23293+414N	M3.5±0.50	M3.5	-12.10±0.67	-12.5	-2.40	1	CAFE	G 190-028
J23340+001	M2.0±0.62	M2.5	-4.31±0.46	-5.0	-	2	FEROS	GJ 899
J23381-162	M2.0±0.46	M2.0	21.12±0.14	19.7	-	3	FEROS	G 273-093
J23438+325	M3.0±0.83	M3.0	-16.30±0.81	-14.0	-	1	CAFE	G 130-006
J23492+024	M1.0±0.31	M1.0	-71.10±0.14	-72.0	-	9	FEROS	BR Psc
J23505-095	M4.5±0.35	M4.0	-20.77±0.24	-42.8	-	3	FEROS	LP 763-012
J23548+385	M3.5±0.43	M4.0	6.70±0.58	0.0	-2.45±0.04	2	CAFE	RX J2354.8+3831
J23556-061	M2.0±0.69	M2.5	18.25±0.06	17.1	-	2	FEROS	GJ 912
J23573-129E	M3.5±0.42	M3.0	49.60±0.46	17.4	-2.45±0.04	2	FEROS	LP 704-015 A
J23577+233	M3.0±0.39	M3.5	-34.99±0.28	-32.4	-	4	FEROS	GJ 1292
J23585+076	M3.0±0.48	M3.0	-7.74±0.07	-4.0	-	4	FEROS	Wolf 1051

Table A.2.: Average results of the spectroscopic analysis of all given stars after the rejection of unusable spectra. All activity indicators with values lower than -4.5 are removed because H_α is not an emission line in this case. Karmn gives the identification number of each star in the CARMENCITA database. SpT the spectral type. v_r the radial velocity. A the activity indicator of H_α. N the number of averaged spectra. Spectro the spectrograph and Name the Simbad name of each star.

Bibliography

Agol, E., Cowan, N. B., Knutson, H. A., Deming, D., Steffen, J. H., Henry, G. W. & Charbonneau, D. (2010) The climate of HD 189733b from fourteen transits and eclipses measured by Spitzer. *The Astrophysical Journal*, **721**(2), 1861.

Bochanski, J. J., Hawley, S. L., Reid, I. N., Covey, K. R., West, A. A., Tinney, C. & Gizis, J. E. (2005) Spectroscopic survey of M dwarfs within 100 parsecs of the Sun. *The Astronomical Journal*, **130**(4), 1871.

Borucki, W. J., Agol, E., Fressin, F., Kaltenegger, L., Rowe, J., Isaacson, H., Fischer, D., Batalha, N. et al. (2013) Kepler-62: A five-planet system with planets of 1.4 and 1.6 Earth radii in the habitable zone. *Science*, **340**(6132), 587–590.

Christen, F., Kuijken, K., Baade, D., Cavadore, C., Deiries, S. & Iwert, O. (2006) CCD Charge Transfer Efficiency (CTE) Derived from Signal Variance in Flat Field Images. In *Scientific detectors for astronomy 2005*, Springer, pp. 543–548.

Clubb, K. I. (2013) The Radial Velocity Equation. URL `http://astro.berkeley.edu/~kclubb/pdf/RV_Derivation.pdf`.

Covey, K., Ivezic, Z., Schlegel, D. et al. (2001) Stellar SEDs from 0.3 to 2.5 μm: Tracing the stellar Locus and the searching for color outliers in the SDSS and 2MASS. *The Astronomical Journal*, **134**.

Cutri, R., Skrutskie, M., Van Dyk, S., Beichman, C., Carpenter, J., Chester, T., Cambresy, L., Evans, T. et al. (2003) 2MASS All Sky Catalog of point sources.

Giampapa, M. (2000) Red Dwarfs/Flare Stars. *Encyclopedia of Astronomy and Astrophysics*, **1**, 1866.

Gray, R. O., Corbally, C. J., Burgasser, A. J., Hanson, M. M., Kirkpatrick, D. J. & Walborn, N. R. (2009) *Stellar spectral classification*, vol. 592. Princeton University Press Princeton.

Hauschildt (1992) *JQSRT*, **47**, 433.

Hawley, S. L., Gizis, J. E. & Reid, I. N. (1996) The Palomar/MSU nearby star spectroscopic survey. II. The southern M dwarfs and investigation of magnetic activity. *The Astronomical Journal*, **112**, 2799.

Irwin, J., Berta, Z. K., Burke, C. J., Charbonneau, D., Nutzman, P., West, A. A. & Falco, E. E. (2011) On the angular momentum evolution of fully convective stars: Rotation periods for field M-dwarfs from the MEarth transit survey. *The Astrophysical Journal*, **727**(1), 56.

Kane, S. R. & Gelino, D. M. (2012) The habitable zone gallery. *Publications of the Astronomical Society of the Pacific*, **124**(914), 323–328.

Kaufer, A., Stahl, O., Tubbesing, S., Nørregaard, P., Avila, G., Francois, P., Pasquini, L. & Pizzella, A. (1999) Commissioning FEROS, the new high-resolution spectrograph at La-Silla. *The Messenger*, **95**, 8–12.

Kniazev, A. Y., Pustilnik, S., Masegosa, J., Márquez, I., Ugryumov, A., Martin, J.-M., Izotov, Y., Engels, D. et al. (2000) HS 0822+ 3542-a new nearby extremely metal-poor galaxy. *arXiv preprint astro-ph/0003320*.

Knutson, H. A., Charbonneau, D., Allen, L. E., Fortney, J. J., Agol, E., Cowan, N. B., Showman, A. P., Cooper, C. S. et al. (2007) A map of the day–night contrast of the extrasolar planet HD 189733b. *Nature*, **447**(7141), 183–186.

LeDrew, G. (2001) The Real Starry Sky. *Journal of the Royal Astronomical Society of Canada*, **95**(1).

Lépine, S. & Gaidos, E. (2011) An all-sky catalog of bright M dwarfs. *The Astronomical Journal*, **142**(4), 138.

Lepine, S., Hilton, E. J., Mann, A. W., Wilde, M., Rojas-Ayala, B., Cruz, K. L. & Gaidos, E. (2013) A Spectroscopic Catalog of the Brightest (J $<$ 9) M Dwarfs in the Northern Sky. *The Astronomical Journal*, **145**(4), 102, URL `http://stacks.iop.org/1538-3881/145/i=4/a=102`.

Lovis, C., Dumusque, X., Santos, N., Bouchy, F., Mayor, M., Pepe, F., Queloz, D., Ségransan, D. et al. (2011) The HARPS search for southern extra-solar planets. XXXI. Magnetic activity cycles in solar-type stars: statistics and impact on precise radial velocities. *arXiv preprint arXiv:1107.5325*.

Mayor, M. & Queloz, D. (1995) A Jupiter-mass companion to a solar-type star. Nature, **378**, 355–359.

Mayor, M. & Queloz, D. (1995) A Jupiter-mass companion to a solar-type star. *Nature*, **378**(6555), 355–359.

Montes, D., CRESPO-CHACÓN, I., GÁLVEZ, M. C., JOSÉ, M., FERNÁNDEZ-FIGUEROA, J. L.-S., DE CASTRO, E., CORNIDE, M. & HERNÁN-OBISPO, M. (2004) Cool Stars: Chromospheric Activity, Rotation, Kinematic and Age. *Lecture Notes and Essays in Astrophysics*, **1**, 119–132.

Mrotzek, N. (2013) *Spektral Klassifizierung von M-Sternen aus HET-Daten*. Bachelor thesis, Göttingen University.

Perryman, M. (2011) *The exoplanet handbook*. Cambridge University Press.

Pfeiffer, M., Frank, C., Baumüller, D., Fuhrmann, K. & Gehren, T. (1997) FOCES-a fibre optics Cassegrain échelle spectrograph? *ASTROPHYSICS*.

Piskunov, N. & Valenti, J. (2002) New algorithms for reducing cross-dispersed echelle spectra. *ASTRONOMY AND ASTROPHYSICS-BERLIN-*, **385**(3), 1095–1106.

Quintana, E. V., Barclay, T., Raymond, S. N., Rowe, J. F., Bolmont, E., Caldwell, D. A., Howell, S. B., Kane, S. R. et al. (2014) An Earth-sized planet in the habitable zone of a cool star. *Science*, **344**(6181), 277–280.

Quirrenbach, A., Amado, P. J., Seifert, W., Carrasco, M. A. S., Mandel, H., Caballero, J. A., Mundt, R., Ribas, I. et al. (2012) CARMENES. I: instrument and survey overview. In *SPIE Astronomical Telescopes+ Instrumentation*, International Society for Optics and Photonics.

Rajpurohit, A., Reylé, C., Allard, F., Homeier, D., Schultheis, M., Bessell, M. & Robin, A. (2013) The effective temperature scale of M dwarfs. *arXiv preprint arXiv:1304.4072*.

Reid, I. N., Hawley, S. L. & Gizis, J. E. (1995) The Palomar/MSU Nearby-Star Spectroscopic Survey. I. The Northern M Dwarfs-Bandstrengths and Kinematics. *The Astronomical Journal*, **110**, 1838.

Reid, N., Reid, I. N., Reid, N. & Hawley, S. (2000) *New light on dark stars*. Springer.

Reiners, A. & Basri, G. (2008) Chromospheric activity, rotation, and rotational braking in M and L dwarfs. *The Astrophysical Journal*, **684**(2), 1390.

Reiners, A. & Jeffers, S. (2013) *Lectures of spectroscopy at Göttingen University*.

Saar, S. H. & Donahue, R. A. (1997) Activity-related radial velocity variation in cool stars. *The Astrophysical Journal*, **485**(1), 319.

Sánchez, S., Aceituno, J., Thiele, U., Grupp, F., Dreizler, S., Bean, J., Benitez, D. & München, U.-S. (2009) CAFE: Calar Alto Fiber-fed Echelle spectrograph.

Schneider, J., Dedieu, C., Sidaner, P. L., Savalle, R. & Zolotukhin, I. (2011) Defining and cataloging exoplanets: the exoplanet. eu database. *arXiv preprint arXiv:1106.0586*.

Schöfer, P. (2013) *Spektroskopie massearmer Sterne*. Bachelor thesis, Göttingen University.

Stumpff, P. (1980) Two self-consistent Fortran subroutines for the computation of the Earth's motion. *Astronomy and Astrophysics Supplement Series*, **41**, 1.

Tipler, P. A., Mosca, G. & Pelte, D. (2004) *Physik für Wissenschaftler und Ingenieure*. Elsevier, Spektrum, Akad. Verlag.

Tull, R. G. (1998) High-resolution fiber-coupled spectrograph of the Hobby-Eberly Telescope. *Optical Astronomical Instrumentation*, **387**.

Tuomi, M., Jones, H. R. A., Barnes, J. R., Anglada-Escudé, G. & Jenkins, J. S. (2014) Bayesian search for low-mass planets around nearby M dwarfs - estimates for occurrence rate based on global detectability statistics. MNRAS, **441**, 1545–1569.

Voigt, H.-H. (2012) *Abriss der Astronomie*. WILEY-VCH.

Weigert, A., Vendker, H. & Wisotzki, L. (2009) *Astronomie und Astrophysik: Ein Grundkurs*. Viley-VCH.

West, A. A., Hawley, S. L., Walkowicz, L. M., Covey, K. R., Silvestri, N. M., Raymond, S. N., Harris, H. C., Munn, J. A. et al. (2004) Spectroscopic properties of cool stars in the Sloan Digital Sky Survey: an analysis of magnetic activity and a search for subdwarfs. *The Astronomical Journal*, **128**(1), 426.

West, A. A., Morgan, D. P., Bochanski, J. J., Andersen, J. M., Bell, K. J., Kowalski, A. F., Davenport, J. R., Hawley, S. L. et al. (2011) The Sloan Digital Sky Survey Data Release 7 Spectroscopic M Dwarf Catalog. I. Data. *The Astronomical Journal*, **141**(3), 97.

Zechmeister, M., Anglada-Escude, G. & Reiners, A. (2013) Flat-relative optimal extraction. A quick and efficient algorithm for stabilised spectrographs. *Astronomy & Astrophysics*.

Danksagung

Ohne die tatkräftige Unterstützung vieler Menschen wäre die Erstellung dieser Arbeit und der Abschluss meines Studiums nicht möglich gewesen.
Mein Dank gilt deswegen besonders Prof. Dr. Ansgar Reiners und Dr. Sandra Jeffers für die Betreuung, Begutachtung und die vielen Hilfestellungen zu dieser Arbeit. Ihre allzeit offene Tür und ihre unermüdliche Unterstützung bei jeder Frage und jedem Problem waren ein Grundstein dieser Arbeit.
Außerdem möchte ich Dr. Mathias Zechmeister und Florian Bauer für ihre Unterstützung in die Einarbeitung der verwendeten Programme und für ihr immer offenes Ohr danken.
Da ohne die Hilfe von Korrekturlesern die Erstellung einer solchen Arbeit kaum machbar wäre, gilt mein Dank natürlich auch Tim Lichtenberg, Alexander Schmelev, Florian Rusteberg und Hendrik Lamert für ihr wachsames Auge und für die Zeit die sie aufgebracht haben.

Besonders meinen Eltern, Jan und Diana Lamert, und meinen Großeltern, die mich in den fünf Jahren meines Studiums in allen denkbaren Belangen unterstützt haben und immer den Glauben an mich bewahrten, möchte ich ein großes Dankeschön aussprechen.

Zum Abschluss möchte ich all meinen Freunden und Kommilitonen für die wunderbare Zeit danken, die ich bisher mit ihnen in Göttingen erleben durfte. Viele Höhepunkte meines Studiums wären ohne sie nicht möglich gewesen, aber auch bei der Überwindung so mancher Tiefs war ihre Unterstützung eine große Hilfe.

Acknowledgments

Without the help of many people the writing of this thesis and the completing of my studies would not have been possible.
I would like to thank Prof. Dr. Ansgar Reiners and Dr. Sandra Jeffers for their supervision, refereeing and support of this thesis. They had always an open door for me and their infinite patience while answering every of my questions is a foundation of this work.
I also want to thank Dr. Mathias Zechmeister and Florian Bauer for their support to help me learning the used programs and to have a sympathetic ear at every time. Without any proofreaders this thesis would not exist. So I want also to thank Tim Lichtenberg, Alexander Schmelev, Florian Rusteberg and Hendrik Lamert for checking this thesis and their time they invested.

A special thank is due to my parents, Jan and Diana Lamert, and to my grand parents for their support of my studies in all possible situations over the last five years and for their never-ending trust in me.

At the end I would also like to thank all my friends and fellow students for the wonderful time I had in Göttingen with them. Many highlights of my studies would not had happened without them, but they were also a great help to overcome some crises.

Erklärung nach §18(8) der Prüfungsordnung für den Bachelor-Studiengang Physik und den Master-Studiengang Physik an der Universität Göttingen:

Hiermit erkläre ich, dass ich diese Abschlussarbeit selbständig verfasst habe, keine anderen als die angegebenen Quellen und Hilfsmittel benutzt habe und alle Stellen, die wörtlich oder sinngemäß aus veröffentlichten Schriften entnommen wurden, als solche kenntlich gemacht habe.
Darüberhinaus erkläre ich, dass diese Abschlussarbeit nicht, auch nicht auszugsweise, im Rahmen einer nichtbestandenen Prüfung an dieser oder einer anderen Hochschule eingereicht wurde.

Göttingen, den 10. September 2014

(Andre Lamert)